Shielding and activation studies for the ELI-beamlines project

Alberto Fasso[1], Anna Ferrari[1,2], Georg Korn[1], Roberto Versaci[1]
[1]ELI-Beamlines, Czech Republic
[2]Helmoltz-Zentrum Dresden-Rossendorf, Germany

Abstract

ELI-beamlines is one of the four pillars of the Extreme Light Infrastructure, a European ESFRI Project, for the next generation of high-energy and high-intensity lasers. It aims at the development of high-brightness sources of X-rays and the acceleration of proton, electron, and ion beams, to be used both for pure research and practical applications. Aiming at a proper radiation protection assessment, for both shielding and activation, extensive FLUKA simulations have been performed, taking into account the laser high repetition rates. The present work, which is the continuation of the calculations presented at SATIF-10, is the first one based on the design of the facility being constructed and on the updated experimental set-up.

Introduction to the ELI Project

The Extreme Light Infrastructure ELI project [1] is part of a European plan, by the European Strategy Forum for Research Infrastructures, ESFRI, to build a new generation of large research laser facilities. The main goal is to achieve ultra-short laser pulses of a few femtoseconds and power of 10 PW. ELI will be operated as a European Research Infrastructure Consortium, ERIC, and will have four facilities: the one whose construction status is the most advanced is ELI-Beamlines in the Czech Republic, the other facilities are ELI-Attosecond in Hungary and ELI-NuclearPhysics in Romania, plus a fourth facility whose location still has to be decided.

Due to the high intensities and short pulses, ELI-Beamlines will provide laser-driven particle beams of both protons having energy up to 3 GeV, and electrons having energy up to 50 GeV. This will allow investigation on a wide range of topics, including accelerator science, plasma physics, material science, etc.

Such energetic beams, which can have repetition rates up to 10 Hz, require a careful and precise assessment of possible radiation protection issues, including prompt dose radiation level in the experimental halls and activation of experimental devices.

We have assessed these issues evaluating the significant quantities by means of FLUKA simulations [2,3]. Also using simulations, we have started working on the modelling of some of the devices that will be installed on the beamlines. Here, we present the preliminary work on the beam dump for the E2 beamline and on the activation of various materials whose use is being envisaged.

Beamlines parameters and FLUKA model

The evaluation of the prompt dose level for each of the ELI's beamlines and for each operation mode would be a massive and very long task, therefore we have focused ourselves on those lines that would be of more concern from the radiation protection

It has been seen that a single target, at the end of an irradiation cycle, causes a dose rate higher than 300 uSv/h at the distance of 6 metres. When the storage is completely filled with targets, the dose rate at 6 metres distance drops to less than 50 uSv/h, due to the fact that the targets shield each other.

Considering the full configuration as source term to design the shielding wall would cause an underestimation of the dose rate in the first operation cycle and this could lead to an overexposure of personnel passing through the corridor nearby. In order to keep both the wall thickness reduced and the dose rate as low as 0.5 uSv/h in controlled areas, it has been decided to shield the first irradiated target deposited in the storage with some empty lead boxes, taking advantage of the lead as shielding. In this scenario a concrete wall 50 cm thick will be sufficient to meet the radiation protection constraints in the corridor.

Acknowledgements

This work has been prepared together with the SPES Target Group, which we would like to acknowledge. They designed the storage rack and shared with us the details of the target handling system.

References

[1] G. Prete, A. Covello (2008) “SPES Technical Design Report”, INFN-LNL-223.

[2] G. Battistoni et al. (2007), “The FLUKA code: Description and benchmarking” *Proceedings of the Hadronic Shower Simulation Workshop 2006, Fermilab 6-8 September 2006, AIP Conference Proceeding* 896, 31-49.

[3] A. Ferrari et al. (2005), “FLUKA: a multi-particle transport code” CERN-2005-10, INFN/TC_05/11, SLAC-R-773.

[4] ICRP 15 (1969), “Protection against Ionizing Radiation from External Sources”, ICRP 21 (1971), “Data for Protection against Ionizing Radiation from External Sources”.

Figure 6. Gamma dose rate (uSv/h) due to 44 stored irradiated targets (side view)

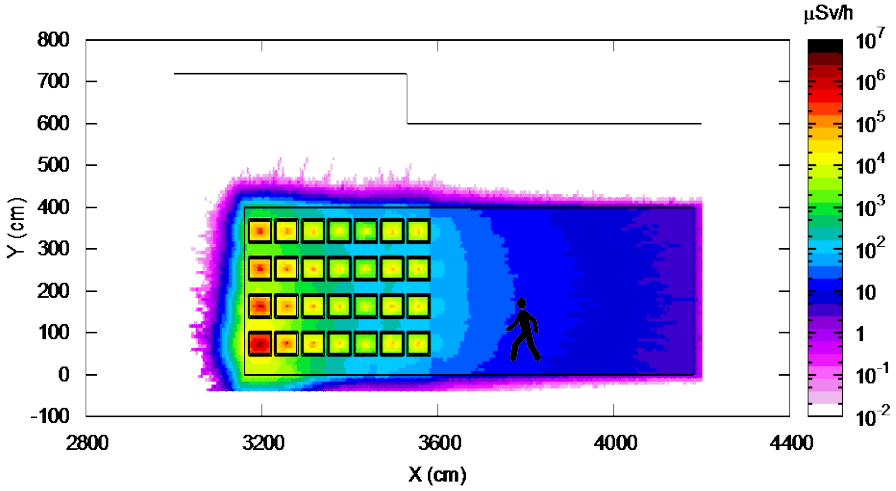

Figure 7. Gamma dose rate (uSv/h) at the end of an irradiation cycle

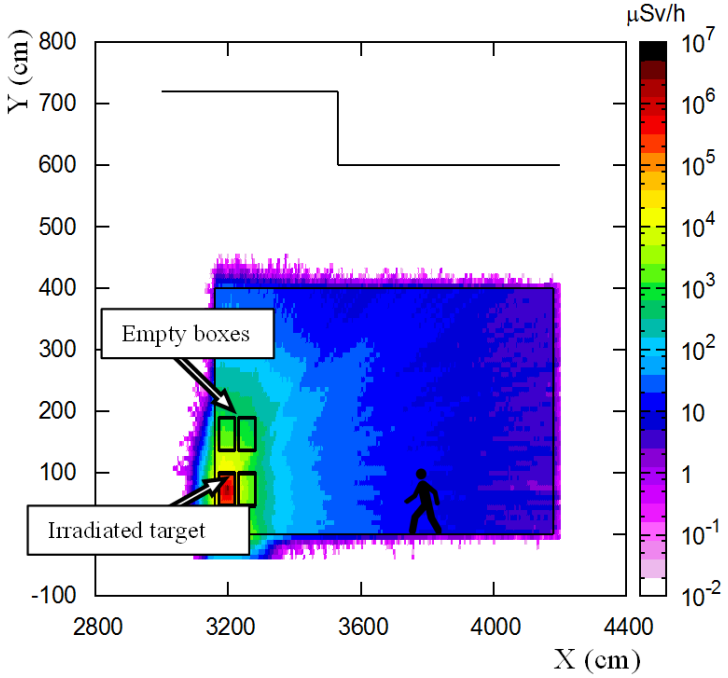

The irradiated target is shielded by some empty lead boxes (side view).

Conclusions

The schedule of the SPES project foresees the irradiation of an uranium carbide target for 12 days and a cooling time of two weeks before the start of a new irradiation cycle. The irradiated target is then placed in a lead box 2.5 cm thick and temporarily stored in a dedicated area close to the bunker, where a rack hosting up to 44 targets is installed.

Due to space restrictions, an accurate evaluation of the dose rate at a certain distance from the targets was needed in order to design an adequate shielding wall. The temporary storage, in fact, borders on a passageway with controlled access of personnel.

The results of this study are shown in Figures 5 and 6. All the available positions have been filled with targets, and the most active is in the furthest position. The dose rate in the passageway in this configuration is below 50 uSv/h, and a reduction of a factor 100 must be achieved. A standard concrete wall 50 cm thick will be sufficient to prevent a dose rate of 0.5 uSv/h where personnel can access.

After the first one or two irradiation cycles, shielding the exhausted targets with some empty lead boxes might be considered (they do not need to be prepared specially as they will be used for future targets). As shown in Figure 7, the dose rate at the desired position is about 50 uSv/h, similar to the "full rack" configuration and the shielding wall can be kept as thin as 50 cm.

Figure 4. Gamma dose rate (uSv/h) at the end of an irradiation cycle

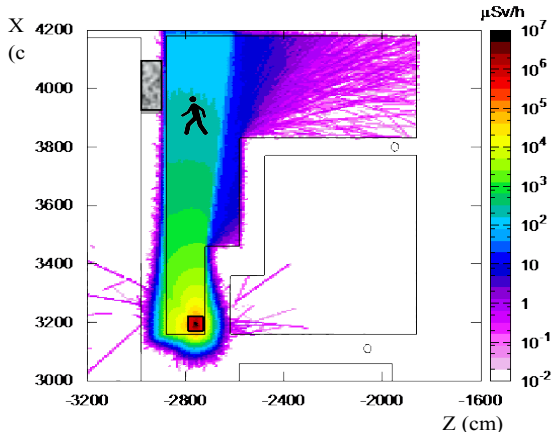

Figure 5. Gamma dose rate (uSv/h) due to 44 stored irradiated targets (aerial view)

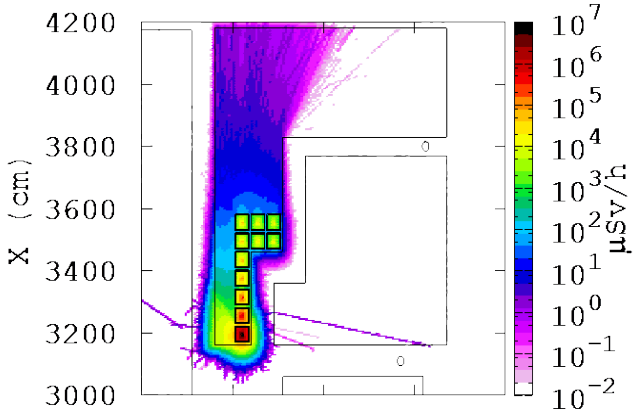

Figure 2. Distribution of the target activation products as a function of the half-life

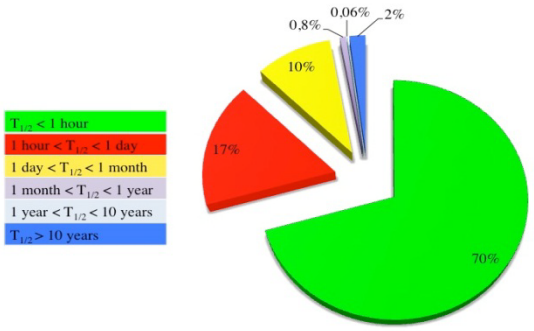

Figure 3. Layout of the SPES Facility (re-acceleration line not included)

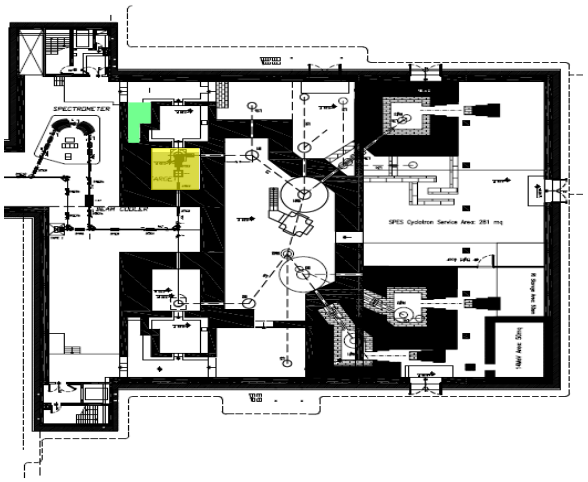

The irradiation bunker is highlighted in yellow and the storage area in green.

Results

The gamma dose rate in correspondence with the passageway is about 300 uSv/h (as indicated by the position of the man in Figure 4), and the photons contributing to this dose rate have an energy in the range of 0.3-3 MeV. In order to fulfill the radiation protection constraints for controlled areas (0.5 uSv/h), a standard concrete wall 70 cm thick must be provided. This allows a dose rate reduction of a factor 10^3 [4].

Furthermore, the configuration of the whole storage filled with targets was studied. To do this, 44 separate simulations were run, one for each target stored. Some preliminary considerations have to be clarified: before being placed in the storage, the irradiated target remains in its position for 14 days.

The targets will be automatically moved from the irradiation cave to the storage area. Once there, a lift will be able to place each target in a dedicated location in a rack.

After a few targets have been stored, their positions will be exchanged so that the furthest position from the passageway will always be free for the most active target in order to take advantage of the shielding effect by the other target boxes.

the target in a low-pressure environment, the heat due to electromagnetic and nuclear interaction will be dissipated by radiative thermal transfer, directly proportional to the body surface. The disks have 40 mm diameter and 1 mm thickness.

Figure 1 shows the multifoil target as implemented in the Monte Carlo geometry in order to simulate the proton-induced fission process, including the graphite container and the dumping disks.

Figure 1. The SPES production target as implemented in the Monte Carlo geometry

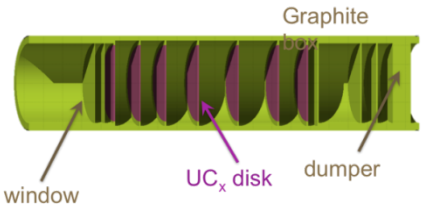

The irradiation of the target lasts 12 days with a total of 10^{21} protons on target per shift and 10^{19} fissions induced. At the end of the irradiation cycle, the radioactivity in the target amounts to around 1 kCi, whose distribution according to the half-life of the products can be seen in Figure 2.

Less than 3% of the total activity is due to species with half-life longer than 1 month and 2% longer than 10 years.

Simulation set-up

In order to simulate the storage of a target after an irradiation cycle, and to evaluate the gamma ambient equivalent dose rate only due to radioactive decay, the capability of FLUKA has been exploited to assign a material to a certain region during irradiation and to change material during decay.

In the present case the target has been placed in the lead box, as it will be performed after an irradiation for storing it, and located in the dedicated area of the storage (the green area in Figure 3, not the yellow one where the irradiation should take place). The volume between the target and the lead box is set to “blackhole” and the irradiation of the target with the proton beam is started. In this simulation phase, all the nuclear and electromagnetic interactions take place but secondary particles do not escape the system because as soon as they leave the target they meet the blackhole.

In this situation the target is activated but the surrounding materials are not, the irradiation is over and the volume between the target and the lead box is switched to air, so that the particles released during the decay can be transported outside and the dose rate in the area of interest can be evaluated.

A temporary storage for activated UCx targets at SPES

Lucia Sarchiapone, Demetre Zafiropoulos
Laboratori Nazionali di Legnaro, INFN, Italy

Abstract

SPES (Selective Production of Exotic Species) is a project of the INFN (Istituto Nazionale di Fisica Nucleare) for the production of radioactive ion beams, through direct irradiation of a fissile target with high-intensity proton beams. The irradiation of the uranium carbide target with protons at 40 MeV energy and 200 μA current during an irradiation cycle of two weeks causes an activity of approximately 10^{14} Bq. Less than 5% of the total activity is due to species of half-lives longer than one month. The replacement of the target takes place at each irradiation shift, ideally once per month, taking into account two weeks of irradiation and two weeks for the facility set-up. For the first years of operation, a temporary storage will host the exhausted targets. This work presents the evaluation of the residual dose rate due to the presence of several irradiated targets in order to design the needed shielding for the storage area and to allow the access nearby. The simulations have been performed with the FLUKA Monte Carlo code.

Introduction

SPES (Selective Production of Exotic Species) is an INFN project to develop a Radioactive Ion Beam (RIB) facility as an intermediate step towards EURISOL (European Isotope Separation On Line). The capability to obtain a RIB of interest for nuclear physics is supported by the presence at LNL (Laboratori Nazionali di Legnaro) of a superconducting linac, able to re-accelerate exotic ions at 8-13 MeV/u.

The RIB is a neutron-rich beam of fission fragments with a fission rate in the target of 10^{13} fissions per second, achieved through the interaction of a proton beam of 40 MeV energy and 0.2 mA current with a target of uranium carbide (production target) [1]. A 70 MeV-0.75 mA cyclotron, actually under construction by Best Cyclotron Systems, Inc. delivers the proton beam.

The production target is irradiated for 12 days and then replaced by a new one. A small area close to the irradiation bunker is being equipped to host up to 44 irradiated targets, conveniently located in lead boxes. Once this temporary storage is full, targets will be moved to their final destination as waste. The temporary storage area is not directly accessible but borders on a passageway classified as a controlled zone. This work presents the evaluation of the shielding thickness required in order to keep the ambient equivalent dose rate below 0.5 μSv/h in the accessible corridor. The evaluation has been performed with Monte Carlo simulations, using the FLUKA code [2,3].

Production target

The production target consists of multiple thin disks housed in a cylindrical graphite box. This geometry increases the body surface in order to optimise the target cooling. In fact,

[14] D.K. Trubey (1988), "New Gamma-Ray Buildup Factor Data for Point Kernel Calculations: ANS-6.4.3 Standard Reference Data", ORNL-RSIC 49.

[15] ANSI/ANS, American National (1991), "Standard for Gamma-Ray Attenuation Coefficients and Buildup Factors for Engineering Materials", ANSI/ANS-6.4.3-1991.

[16] Nucleonica GmbH, Dosimetry and Shielding (2011), "Nucleonica Nuclear Science Portal (www.nucleonica.com)", Version 3.0.06, Karlsruhe, Germany.

provided. The utilised initial nuclide inventories, including radioisotope production terms, can either originate directly from ActiWiz, from Monte Carlo codes like FLUKA, PHITS, MARS and MCNP or from gamma spectroscopy measurements. In this paper, details on the mathematical derivation of the implemented algorithms to calculate the time evolution of nuclide inventories are given, including also some numerical considerations.

Often activated material also needs to be transported. The appropriate shielding requirements, including photon dose build-up, can be calculated with ActiWiz within a few seconds even for large nuclide sets with many thousands of gamma lines. An overview of the implemented deterministic calculation method is provided and successful benchmark comparisons to another deterministic code (Nucleonica) as well as the FLUKA Monte Carlo code have been performed.

Acknowledgements

The authors would like to thank Stefan Roesler and Eduard Feldbaumer for stimulating discussions and the review of the Technical Notes which led to this paper. We would also like to express our gratitude to Joseph Magill from Nucleonica GmbH for fruitful discussions on the topic of shielding and Matthias Karacson for the meticulous review of this manuscript.

References

[1] H. Vincke, C. Theis (2013), "ActiWiz – optimizing your nuclide inventory at proton accelerators with a computer code", *Proceedings of the ICRS12 conference, 2012, Nara, Japan, Progress in Nuclear Science and Technology*.

[2] A. Fassò, A. Ferrari, J. Ranft, P. Sala (2005), "FLUKA: a multi-particle transport code", *CERN Yellow Report*, INFN/TC_05/11, SLAC-R-773.

[3] G. Battistoni et al. (2007), "The FLUKA code: Description and benchmarking", *Proceedings of the Hadronic Shower Simulation Workshop 2006, Fermilab 6--8 September 2006, M. Albrow, R. Raja eds.*, AIP Conf. Proc., 896, pp. 31-49.

[4] H. Vincke, C. Theis (2011), "ActiWiz: A computer code to model and assess radiological hazards of activated material", *CERN Technical Note CERN-DGS-2011-067-RP-TN*, CERN.

[5] suvaPro (2009), "Schweizer Strahlenschutzgesetz vom 22.3.1993 (StSG), Strahlenschutzverordnung vom 22.6.1994 (StSV), Stand 1.

[6] H. Bateman (1910), "Solution of a system of differential equations occurring in the theory of radioactive transformations", *Proc. Cambridge Philos. Soc. 15,* pp. 423-427.

[7] A. Koning et al. (2009), "The JEFF-3.1.1. nuclear data library", *JEFF Report 22*.

[8] K. Skrable et al. (1974), "A general equation for the kinetics of linear first order phenomena and suggested applications", *Health Physics, 27,* pp. 155-157.

[9] J. Cetnar (2006), "General solution of Bateman equations for nuclear transmutations", *Ann. Nucl. Energy* 33, pp. 640 – 645.

[10] R. Dreher (2013), "Modified Bateman solution for identical eigenvalues", *Annals of Nuclear Energy* 53, pp. 427 – 438.

[11] W. Kahan (1965), "Further remarks on reducing truncation errors", *Communications of the ACM 8 (1)*: 40, http://doi:10.1145/363707.363723, (1965).

[12] C. Theis, H. Vincke (2014), "Floating point considerations for ActiWiz 3", *CERN Technical Note,* CERN-RP-2014-016-REPORTS-TN, EDMS 1363729.

[13] C. Theis, H. Vincke (2014), "Addendum to the build-up and decay engine in ActiWiz", *CERN Technical Note,* CERN-RP-2014-017-REPORTS-TN, EDMS 1363771.

Figure 4. Set-up of the shielding calculation conducted with FLUKA

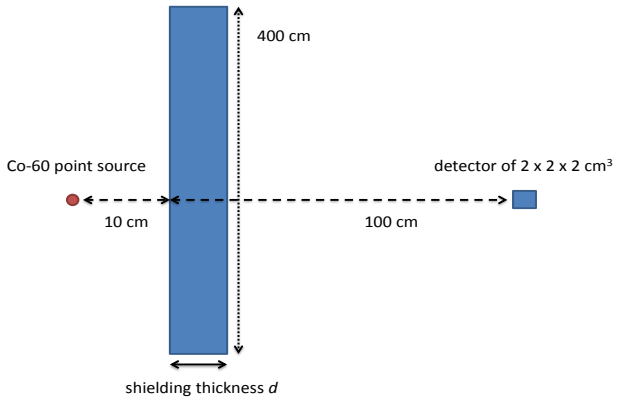

Table 1. Tenth-value dimension calculated by ActiWiz, Nucleonica and FLUKA for different materials

Material	ActiWiz/cm	Nucleonica/cm	FLUKA/cm	ActiWiz – FLUKA Δ/cm
Iron (ρ = 7.8 g/cm^3)	9.9	9.9	8.2 +/- 2%	1.7
Concrete (ρ = 2.4 g/cm^3)	30.5	30.5	26.0 +/- 2%	4.5
Lead (ρ = 11.3 g/cm^3)	5.0	5.0	4.6 +/- 3%	0.4

The uncertainty from the Monte Carlo simulation reflects solely the statistical fluctuations and does not consider any differences which could originate due to different nuclear data sets.

As shown in Table 1, the deterministic calculations of ActiWiz and Nucleonica would predict a slightly thicker shielding required for achieving an attenuation level of 1/10. The actual differences range from 0.4 cm of lead over 1.7 cm of iron to 4.5 cm of concrete, which is equivalent to 10-20% in terms of the respective total thickness. These deviations can be understood keeping in mind that the build-up factor in the deterministic calculations is approximated by a "one-size-fits-all" function, which conservatively tries to cover different geometric set-ups. As a consequence, the results might be slightly overestimated for some cases in contrast to a Monte Carlo simulation which can mimic the actual scenario by tracking particle trajectories through a full geometry. However, this flexibility and accuracy comes at the cost of speed and requires significantly more calculation time that can differ by several orders of magnitude. In general, the comparison between the deterministic solutions of ActiWiz and Nucleonica and the stochastic solution of FLUKA for a defined geometry yields reasonable agreement. In conclusion, the validation of the deterministic algorithms can be considered successful.

Summary and conclusions

The ActiWiz code has originally been developed at CERN for easy and quick assessment and comparison of the radiological hazard of materials used in the environment of high-energy accelerators. Due to its foundations on nuclide production terms, extensions have recently been developed which allow for expanding the scope of its application also to the field of operational radiation protection. An isotope build-up and decay engine has been developed to calculate nuclide inventories for arbitrary irradiation- and cooling period patterns. Automatic analysis of the dominating contributors to various quantities like radiotoxicity, clearance levels, photon dose-rate, gamma emission spectra etc. is

comparison involving the "Fukushima" nuclide set without daughter products. Yet, perfect agreement is found also in this case for iron or concrete shielding. This suggests that there could be small differences in the data sets that are used to describe the respective decay chains or small deviations in the assumed material density as ActiWiz generally suggests lower values for uranium. However, the differences vary only between 3-6%, which can be considered as good agreement.

Figure 3. Ratio of the shielding thickness calculated by ActiWiz versus the results obtained from Nucleonica to reach 1/10 of the original dose for various materials and radiation sources

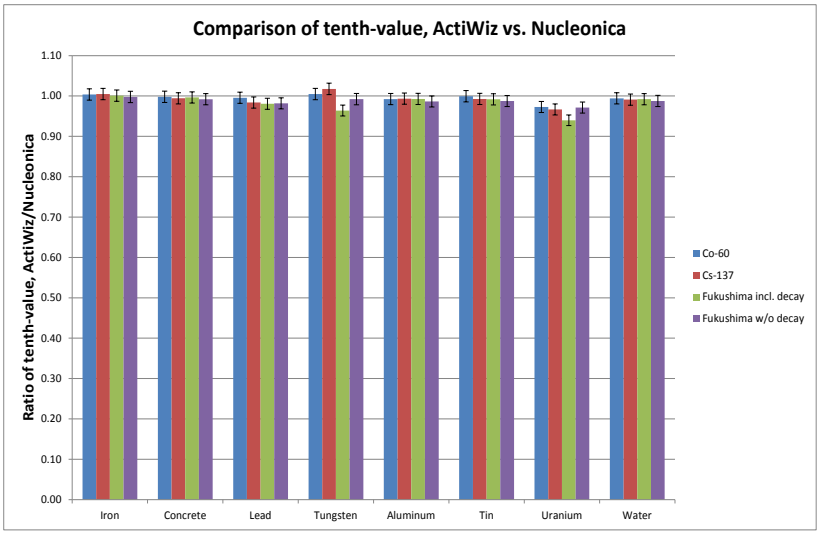

Comparison of ActiWiz, Nucleonica and FLUKA

In contrast to Monte Carlo simulations deterministic calculations of shielding, dimensions must account for the so-called radiation build-up effect in an approximated way. This correction should include indirect contributions due to in-scattering effects that usually can occur in scenarios involving massive shielding. These effects would increase the actual dose rate encountered at a detector in addition to line-of-sight contributions originating directly from the radiation source. It is important to keep in mind that the actual build-up depends on parameters like shielding thickness and extension, distance between shielding and source, distance between shielding and detector and the actual detector size. As the correction function utilised in deterministic assessments cannot fully account for all varieties of these details one can expect to have deviations from Monte Carlo simulations which are conducted for a specific geometric set-up. The actual situation that has been considered in the FLUKA Monte Carlo simulation is illustrated in Figure 4.

For typical shielding materials like iron, lead and concrete the tenth-value shielding thickness d, being pre-calculated with ActiWiz, has been used to calculate the dose attenuation for the given set-up with FLUKA. This result has then been extrapolated back to obtain an estimation for a FLUKA calculated tenth-value shielding thickness. The comparison to the tenth-values calculated by ActiWiz and Nucleonica is given in Table 1.

Figure 2. Exemplary attenuation curve of an iron shielding enclosing the activated electronic circuit board for which the photon emission spectrum illustrated in Figure 1 has been determined

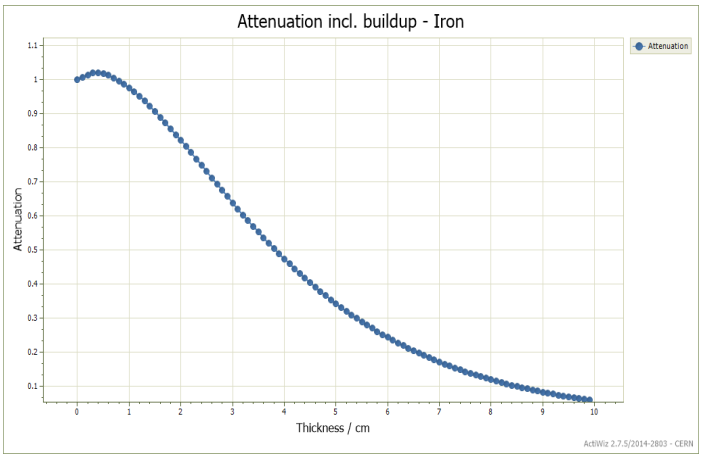

Benchmark of the shielding calculations

The actual performance of the calculations should not be judged only in terms of runtime but also in terms of accuracy and therefore, validation of the results is of highest importance. Comparisons of the estimates obtained by ActiWiz have been conducted with respect to Nucleonica [16] as well as the Monte Carlo code FLUKA. Nucleonica is a well-established toolkit used in the nuclear industry, which is based on internationally validated nuclear data. Within its wide selection of tools it contains a dosimetry and shielding calculator ("Dosimetry and Shielding++") which also uses a deterministic method to assess shielding dimensions. Therefore, the results can be directly compared to ActiWiz and the benchmark is eventually complemented by a comparison to a Monte Carlo based assessment conducted with FLUKA. In order to compare the different codes it has been decided to determine the shielding thickness required for an attenuation to 1/10 of the original dose rate.

Comparison of ActiWiz and Nucleonica

The selection comprised ^{137}Cs (dominant gamma line at 662 keV) as well as ^{60}Co (dominant gamma lines at 1.17 MeV and 1.32 MeV) as well as a complex nuclide mixture called "Fukushima" which is provided by Nucleonica on their web portal [16]. In order to increase the level of complexity in the comparison the nuclide mixture "Fukushima" has been used in two different scenarios. On one hand, the original nuclide set has been considered to be shielded and on the other hand, Nucleonica as well as ActiWiz independently calculated the time evolution of this mixture for a period of 1 month to also include daughter products originating from decay chains in the shielding assessment. The results of all comparisons are illustrated in Figure 3.

As can be seen in Figure 3, the results of both codes are in very good agreement. One has to keep in mind that most probably there are differences in the numerical algorithms that have been used in the two codes as well as in the nuclear data set of the gamma lines. Nucleonica uses the JEFF-3.1.1 library, whereas the gamma library used in ActiWiz was custom-built. It is primarily based on ENDF/B-VII.1, which has been found to be the most complete collection, containing information of over 70.000 gamma lines, and complemented, with information on missing radionuclides obtained from JEFF-3.1.1, JEF-2.2 and JENDL-FPDD2000. In total 101539 single gamma lines are contained in this merged data set. The most notable differences have been found in the comparison considering the "Fukushima" nuclide mixture including daughter products after one month of exemplary decay. One can see that these deviations are larger than the

Figure 1. Exemplary photon emission spectrum of an activated electronic circuit board comprising 60176 different gamma lines originating from 1308 isotopes

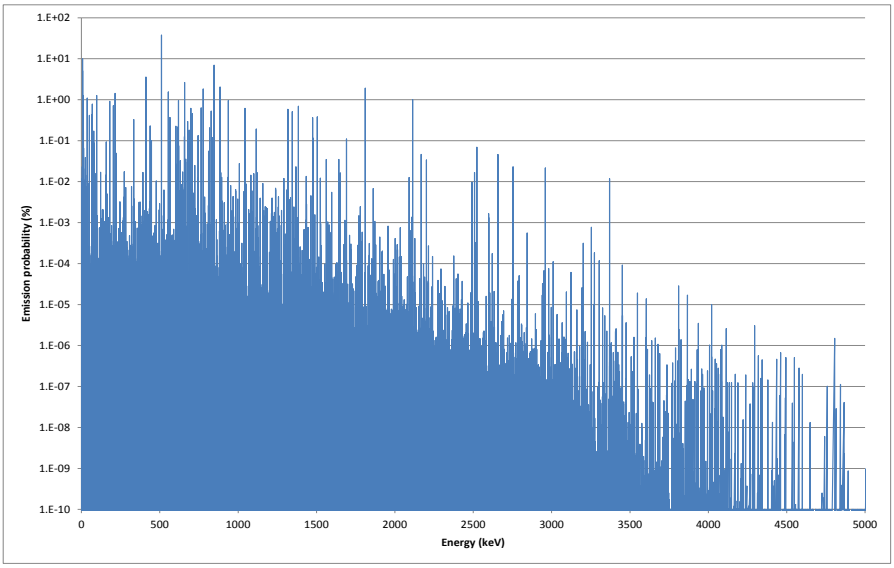

It is obvious that for such cases accurate assessment by deterministic methods requires the use of computational methods. One possible solution would be to first express the build-up factor B with an analytical approximation following the so-called "geometric progression form" as suggested in [14]. This expression is computationally rather complex and involves time consuming functions like the evaluation of the hyperbolic tangent. In order to save computation time for typical shielding materials like iron, concrete or lead the expression has been pre-calculated and tabulated [15] as a function of the energy as well as the so-called relaxation length R, which is equivalent to the mean-free path.

The solution implemented in ActiWiz generates specific build-up factor tables, which match the whole ensemble of photon energies emitted by the activated material. This is done on-the-fly by calculating two subsequent interpolations of tabulated build-up factors taken from [15]. The first interpolation is conducted with respect to the photon energy. It is followed by a second interpolation with respect to the relaxation length of a given photon in the shielding material. These tables are then used to express the build-up factors in Equation (7) as functions of the shielding thickness r only. The resulting expression is numerically solved for r by iterative evaluation and bisection based root-finding methods. The shielding materials available within ActiWiz currently comprise aluminum, concrete, iron, lead, water and tungsten. In addition to determining shielding dimensions for a desirable attenuation factor the user can also directly obtain graphs of attenuation curves as a function of the shielding thickness for the respective radionuclide mixture. Figure 1 shows an exemplary photon emission spectrum of an activated electronic circuit board which exhibits more than 60.000 discrete photon energies. In order to shield this equipment, an exemplary iron shielding (ρ = 7.8 g/cm^3) has been envisaged and the corresponding attenuation curve calculated by ActiWiz is shown in Figure 2. The curve contains 100 different data points and the calculation took about 1 second on a medium-level desktop PC (Intel i7-2600, 3.4 GHz), which can be considered as sufficiently fast for this rather complex example.

French exemption and clearance limits) or various activity to dose conversion factors (ambient dose equivalent, effective dose e(50) for inhalation and ingestion following ICRP 72) is provided. The code automatically identifies predominantly contributing isotopes and generates plots for gamma emission spectra (without correction of self-absorption) and the respective photon dose contribution. For the scenarios directly comprised by ActiWiz, a detailed analysis is carried out to identify the chemical element from which the respective nuclides are produced. The contribution is quantified which eventually allows for a sensitivity study of materials with respect to trace elements and impurities.

Shielding of activated material

At one point activated material typically needs to be separated from its surroundings and in addition may require transportation. In order to assess the required shielding thickness for these operations, one has to define the desirable attenuation that should be achieved and the shielding material to be used. The determination of the shielding dimensions can be done either by applying deterministic formulas or Monte Carlo simulations. Each of these approaches has its advantages as well as trade-offs. Monte Carlo simulations generally yield high precision as they take all secondary radiation effects into account, but they are very time consuming to set up and often entail considerable computation time. Deterministic assessment requires taking material and energy dependent attenuation and build-up factors into account. This can be done easily for simple cases (e.g. ^{137}Cs calibration source) where there is only one predominating energy-component and when the build-up is neglected for reasons of simplicity. However, in the environment of a particle accelerator one is usually confronted with activated material showing a broad energy spectrum of emitted radiation (mainly gamma radiation) that needs to be shielded (see Figure 1).

In general, the dose D caused by a point source at a certain distance d within a medium of thickness r can be expressed as:

$$D(d,r) = D(d = 1m, r = 0m)\, B(E,r) \frac{e^{-\mu(E)r}}{d^2} \tag{6}$$

with $\mu(E)$ describing the energy dependent attenuation coefficient and B being the dose build-up factor that in turn depends on the photon's energy as well as the shielding thickness. For shielding assessments the problem is usually formalised in view of a relative dose reduction (e.g. 1/10 of the original dose) for a given distance when placing a shielding material in between the radioactive object and the location of potential radiation exposure. Using the relative attenuation, the dependence on the distance between the source and the point of interest is implicitly considered. Therefore, Equation (6) can be re-written by introducing a relative dose-reduction factor A and a quantity C, denoting the relative contributions of the different photon energies to the total dose:

$$A = \sum_{i=1}^{n} C_i\, B_i(E_i, r) e^{-\mu_i(E_i)r} \tag{7}$$

In order to calculate the required shielding thickness to achieve the dose reduction factor A one would need to solve this equation for the variable r. The difficulty lies on one hand in the fact that the sum on the right might span over thousands of terms and that at the same time the build-up factor depends on the variable r as well. Using the logarithm to solve for r does not work as there is no simple mathematical expression for the logarithm of sums in contrast to the logarithm of products.

with standard double precision floating point accuracy would still fail, an example being the decay process of 1 kg of ^{238}U over 100 years. Therefore, ActiWiz implements multi-precision arithmetics with a custom developed plugin data-type based on the MPRF library. As this wide topic is beyond the scope of this paper the interested reader is kindly referred to [12] for details.

Specific treatment of stable nuclides

As mentioned before, Equation (2) provides an analytic closed-form solution to the Bateman equations. Yet, some attention has to be paid during the implementation because the sub-expression describing the build-up of new nuclides:

$$\frac{P_i^k(1-e^{-\lambda_j t_{k,irr}})e^{-\lambda_j t_{k,cool}}}{\lambda_j \prod_{\substack{p=i \\ p\neq j}}^{n}(\lambda_p-\lambda_j)} \tag{3}$$

can become indeterminate $\left(\frac{0}{0}\right)$ if $\lambda_j = 0$, which is the case for stable nuclides. Commonly text-books on radiation physics address Bateman's equations in a simplified way and exclude the production term illustrated in Equation (3). Thus, they inherently avoid the need to address the problem of indeterminate terms. If the chain is not followed down to the last stable element or if only activity values (A = λN) instead of nuclide concentrations are of interest, this issue will most of the time go unnoticed as the activity of a stable isotope can directly be set to zero. Clearly, a numerical work-around can be found by artificially introducing an extremely small decay constant and thus approximating the calculation at the end of each decay chain. Yet, this somehow defies the idea of finding an accurate and generic solution that can be analytically calculated. Thus, we attempted to find a fully analytic solution which specifically treats the indeterminate case. The actual problem to be solved is given by:

$$\lim_{\lambda_j\to 0}\frac{P_i\left(1-e^{-\lambda_j t_{irr}}\right)e^{-\lambda_j t_{cool}}}{\lambda_j\prod_{\substack{p=i\\p\neq j}}^{n}(\lambda_p-\lambda_j)} = \lim_{\lambda_j\to 0}\frac{\frac{\partial}{\partial\lambda_j}\left(P_i\left(1-e^{-\lambda_j t_{irr}}\right)e^{-\lambda_j t_{cool}}\right)}{\frac{\partial}{\partial\lambda_j}\left(\lambda_j\prod_{\substack{p=i\\p\neq j}}^{n}(\lambda_p-\lambda_j)\right)} \tag{4}$$

A thorough mathematical treatise can be found in [13]. For reasons of conciseness only the final result will be shown. Consequently, for the full analytic solution which also circumvents indeterminate sub-terms for the calculation of stable nuclide concentrations one obtains:

$$N_n(t) = \sum_{k=1}^{m}\sum_{i=1}^{n}\left[\left(\prod_{j=i}^{n-1}\lambda_{j,j+1}\right)\sum_{j=i}^{n}\left(\frac{N_i^k e^{-\lambda_j(t_{k,irr}+t_{k,cool})}}{\prod_{\substack{p=i\\p\neq j}}^{n}(\lambda_p-\lambda_j)} + \begin{cases}\dfrac{P_i\left(1-e^{-\lambda_j t_{irr}}\right)e^{-\lambda_j t_{cool}}}{\lambda_j\prod_{\substack{p=i\\p\neq j}}^{n}(\lambda_p-\lambda_j)} & \lambda_j\neq 0\\ \dfrac{P_i\, t_{irr}}{\prod_{\substack{p=i\\p\neq j}}^{n}\lambda_p} & \lambda_j = 0\end{cases}\right)\right] \tag{5}$$

This analytic solution has been fully implemented in ActiWiz and can be used to calculate the time evolution of nuclide inventories for scenarios either directly included in ActiWiz, which are based on FLUKA calculations of generic cases, or external source terms originating from other Monte Carlo codes or measurements. Subsequent convolution with either legal limits (Swiss exemption limits, Swiss authorisation limits [5],

In our definition an irradiation sub-pattern always consists of an irradiation period t_{irr} followed by a cooling period t_{cool}. Taking this into account, we can conduct a simple change of variable ($t = t_{irr} + t_{cool}$). As a consequence, the solution of the Bateman equations can be trivially extended to allow for calculating the respective nuclide concentrations for a pair of time periods, t_{irr} and t_{cool}, in a single step:

$$N_n(t) = \sum_{k=1}^{m}\sum_{i=1}^{n}\left[\left(\prod_{j=i}^{n-1}\lambda_{j,j+1}\right)\sum_{j=i}^{n}\left(\frac{N_i^k e^{-\lambda_j(t_{k,irr}+t_{k,cool})}}{\prod_{\substack{p=i\\p\neq j}}^{n}(\lambda_p-\lambda_j)} + \frac{P_i^k(1-e^{-\lambda_j t_{k,irr}})e^{-\lambda_j t_{k,cool}}}{\lambda_j\prod_{\substack{p=i\\p\neq j}}^{n}(\lambda_p-\lambda_j)}\right)\right] \quad (2)$$

This expression yields the nuclide concentration of the n^{th} isotope species in a decay chain after m consecutive irradiation patterns (consisting always of pairs of irradiation and cooling periods $t_{k,irr}$ and $t_{k,cool}$ for $k = 1…m$). It should be noted that possible initial concentrations of isotopes (N_i^k) are also taken into account during the treatment of the respective irradiation/cooling period indexed with k.

Detailed numerical and mathematical considerations

Evaluation of Equation (2) requires that some attention is paid to subtle mathematical as well as numerical aspects. On one hand the denominator $\prod_{p=i,p\neq j}^{n}(\lambda_p-\lambda_j)$ might yield zero for identical decay constants found at different levels of the decay chain. This is for example possible for the transmutation and decay of:

$$^{235}U \xrightarrow{(n,\gamma)} {}^{236}U \xrightarrow{(n,\gamma)} {}^{237}U \xrightarrow{\beta-} {}^{237}Np \xrightarrow{(n,\gamma)} {}^{238}Np \xrightarrow{\beta-} {}^{238}Pu \xrightarrow{(n,\gamma)} {}^{239}Pu \xrightarrow{\alpha} {}^{235}U.$$

Even if such physically closed loops are excluded in the data structures right from the beginning, as they might be of low significance for accelerator applications, they could be encountered as numerically closed loops if two decay constants cancel out due to insufficient numerical precision of the computer's floating point unit. A thorough and proper mathematical treatment of these cases can be found in [9,10]. However, in ActiWiz, for reason of simplicity and performance, an extremely simplified approach is implemented which ensures that such numerical cancellation does not occur. This is done by artificially modifying one decay constant as $\lambda = \lambda * (1+\varepsilon)$ with $\varepsilon << 1$ if the difference of two decay constants in the chain would evaluate to zero within floating point precision.

Another aspect which numerically could cause problems is the evaluation of $1 - e^{-\lambda t_{irr}}$ if the argument of the exponential function tends towards zero. The trivial approach to solve this situation is to replace the exponential with its Taylor series expansion which would result in $e^{-\lambda t_{irr}} \sim 1 - \lambda t_{irr}$. This simple approximation could also reveal non-obvious numerical problems when being applied to the whole term of $1 - e^{-\lambda t_{irr}}$, rather than just the exponential function. Detailed mathematical treatments of the numerical pitfalls of this specific case can be found in literature on numerical analysis. However, modern C++ compilers as well as some scientific computation libraries provide a function called *expm1()* which specifically handles the issue of calculating $e^x - 1$ in a numerically sound way for very small values of x. This function is used in our implementation. It should be noted that the actual algorithm of this function is implementation specific and thus, results could slightly vary from platform to platform. To the authors' current knowledge in most cases the chosen approach is based on Taylor series expansion to machine precision or polynomial interpolation like high-order Remez polynomials. Another important numerical aspect is the summation of the different terms of Equation (2). Keeping in mind that a computer provides finite precision in terms of floating point representation this sum can result in an accumulation of errors. A remedy would be the introduction of compensated summation like Kahan's algorithm [11]. Yet, calculations

mixture of the activated equipment into consideration. As this calculation is based on a relative attenuation factor, the self-shielding due to the object's actual geometry is implicitly taken into account.

Calculation of nuclide inventories

Nuclide inventories are a function of the material's chemical composition, the energy and the location of exposure in the accelerator as well as a defined irradiation and cooling period. The original concept of ActiWiz neither foresaw direct determination of nuclide inventories nor made them available to the user. Thus, the results calculated by the risk assessment model were directly based on the original FLUKA simulations, which already provided the activity of the various radioisotopes for the aforementioned parameters. Consequently, the user was restricted to the irradiation and cooling patterns that were directly available in ActiWiz. While this should satisfy most needs with respect to typical applications in radiation protection, there might be questions that could arise during specific studies that would require the determination of nuclide inventories for deviating or more complex irradiation and cooling patterns. This has led to the decision to develop and implement a dedicated isotope build-up and decay engine for ActiWiz, which uses the nuclide production source-terms of FLUKA for the irradiation scenarios described in [4], while providing the user with the flexibility to specify arbitrarily complex sequences of irradiation and cooling periods. In addition, nuclide production source terms from external sources can be used, which describe simulation scenarios and radiation environments beyond those already included in ActiWiz.

The production and decay of radioisotopes is described by linear first order kinetics which can be expressed as a series of coupled differential equations discussed originally by H. Bateman [6]. The quantity of a specific isotope is determined by a linear chain of parent and daughter nuclides which undergo first order production and decay phenomena. It can be understood as illustrated in Equation (1):

$$\frac{dN_i(t)}{dt} = -\lambda_i N_i(t) + \lambda_{i-1,i} N_{i-1}(t) + P_i \quad (1)$$

N_i denotes the quantity of the i^{th} member of the production/decay chain and λ_i being its decay constant. As the chains might branch into multiple sub-branches each progression from one generation to the next is connected with a branching fraction $b_{i,i+1}$ describing the partial branching from the parent of order i to the respective daughter of order $i+1$ [7]. Thus, a partial decay constant for the i^{th} species, considering branching, is defined as $\lambda_{i,i+1} = \lambda_i * b_{i,i+1}$. For the general description one cannot only restrict oneself to pure decay of isotopes. It is also important to consider their continuous production via the production rate P_i. Via the Laplace transforms $L\{N_i(t)\}=n_i(s)$ and $L\{N'_i(t)\}= s * n_i(s) - N_i(0)$, this system of differential equations can be transformed into a simple algebraic relation that can be solved for $n_i(s)$ by rearranging the terms as discussed in [8].

Operation of a particle accelerator can be seen as a sequence of time intervals during which the beam can either be present or switched off. Periods during which the particle beam is present will directly contribute to the build-up of radioactivity and thus will be referred to as "irradiation periods". During time spans without beam only radioactive decay will be observed and consequently they will be termed "cooling periods". However, one must also take into account that for example nuclides that could have been present at the beginning of an irradiation period will also decay during this time span. For accelerator applications an irradiation pattern typically consists of various consecutive irradiation sub-patterns, each of which comprise an irradiation period t_{irr}, resulting in the build-up of nuclides, followed by a cooling period t_{cool} during which only the decay of nuclides occurs. The resulting nuclide concentrations of such sub-patterns can be calculated by iterative solution of Equation (1) to the respective time span t_{irr} and t_{cool}, with appropriate selection of the associated factors $N_i(t)$ and $P_i(t)$.

The use of ActiWiz in operational radiation protection

Christian Theis, Helmut Vincke
CERN European Organisation for Nuclear Research, Switzerland

Abstract

The ActiWiz code was originally developed at CERN for easy and quick assessment and comparison of the radiological hazard of materials used in the environment of high-energy accelerators. Due to its foundations on nuclide production terms, extensions have recently been developed which allow for expanding the scope of its application also to the field of operational radiation protection. An isotope build-up and decay engine has been developed to calculate nuclide inventories for arbitrary irradiation- and cooling period patterns. Automatic analysis of the dominating contributors to various quantities like radiotoxicity, clearance levels, photon dose-rate, gamma emission spectra etc. is provided. In addition, shielding of activated equipment, including the treatment of photon dose build-up factors, can be calculated within a few seconds even for nuclide sets with many thousands of gamma lines. The utilised initial nuclear inventories, including radioisotope production terms, can either originate directly from ActiWiz, from Monte Carlo codes like FLUKA, PHITS, MARS, MCNP or gamma spectroscopy measurements. In this paper an overview of these new features and a benchmark comparison to shielding calculations with FLUKA and the analytic Nucleonica code are given.

Introduction

The ActiWiz code [1] was originally developed to assess the radiological hazard of materials that are used in the environment of CERN's accelerators. It is based on a large number of FLUKA [2,3] calculations yielding nuclide inventories for the exposure of 69 basic constituents (chemical elements and a few radioisotopes) to various irradiation scenarios typically found at high-energy proton accelerators. These nuclide inventories constitute the foundation for ActiWiz' risk model that is applied to compare the radiological hazard of compounds that can be freely defined by the user. For a detailed description please refer to [4].

Further studies are required which focus on the classification of material as conventional or radioactive waste, handling constraints in radioactive workshops, transport, etc. For these purposes, the calculation of nuclide inventories is required. The original code has been extended in version 2, introducing the calculation of nuclide inventories of compounds with subsequent convolution with either legal limits (Swiss exemption limits [5]) or various activity-to-dose conversion factors. This allows for the determination of the dominating contributors either to a compound's radiotoxicity or to its dose emission. At the same time, for a specific irradiation scenario the theoretical photon emission spectrum of an activated compound is calculated, neglecting self-shielding as the geometry of the real object is unknown. Furthermore, dominating photon energies that need to be considered for the shielding of radioactive material are highlighted. In addition, for a desirable relative attenuation factor (e.g. 1/10) the thickness for various shielding materials can automatically be determined, taking the full isotopic

[9] A.J. Malensek, A.A. Wehmann, A.J. Elwyn, K.J. Moss and P.M. Kesich (1993), "Groundwater Migration of Radionuclides at Fermilab", FERMILAB-TM-1851.

[10] NTH Consultants, Ltd.; http://www.nthconsultants.com/.

[11] RWDI; http://www.rwdi.com/.

[12] J.D. Cossairt (2000), "Calculation of the Radioactivity Produced in the Cooling Loops of the CDF SVX II Detector", Fermilab-TM-2112.

[13] MicroShield6 code; http://www.radiationsoftware.com/.

Figure 11. Receptor locations evaluated

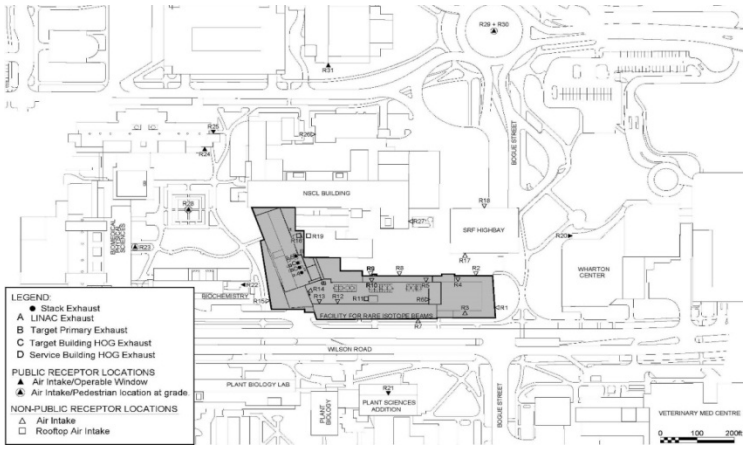

Conclusions

This paper provides an overview of the range of conservative radiation transport analyses performed in support of the FRIB design. The focus is on analyses that demonstrate compliance with NRC limits and MSU ALARA goals for postulated human and environmental exposure. Actual exposure will be based on measurements during commissioning and operation. These radiation calculations demonstrate anticipated acceptability and support the start of technical construction. Radiation transport will continue to support the designers, to ensure the completion of the final design, commissioning and operations.

Acknowledgements

This material is based on work supported by the US Department of Energy Office of Science under Cooperative Agreement DE-SC0000661.

References

[1] Standards for sump water, Nuclear Regulatory Commission, 10 CFR 20.

[2] MSU ALARA – NRC License Number 21-00021-29, MSU Type A Broad Scope License. MSU operates as a fully-licensed, non fuel cycle R&D Type A, NRC broad-scope licensee since 1977.

[3] Standards for drinking water, Entironmental Protection Agency, 40 CFR 141.

[4] N.V. Mokhov (1995), “The Mars Code System User's Guide”, Fermilab-FN-628.

[5] N.V. Mokhov, S.I. Striganov (2007), “MARS15 Overview”, Fermilab-Conf-07/008-AD; *Proc. of Hadronic Shower Simulation Workshop,* Fermilab, September 2006, AIP Conf. Proc. 896, pp. 50-60.

[6] http://www-ap.fnal.gov/MARS/.

[7] A. Wehmann, W. Smart, S. Menary, J. Hylen and S. Childress (1997), “Groundwater Protection for the NuMI Project”, FERMILAB-TM-2009.

[8] Bill Freeman (1996), "A NuMI Wide-Band Beam Shield Design That Meets the Concentration Model Groundwater Criteria", NuMI Note B-155.

consequent capture by the water condensate. The concentrations of the nuclides produced by the first mechanism were calculated using the same approach as used for water in the LCA and CHA systems. Similar model was also used for the production of ^{3}H, ^{7}Be, ^{11}C, ^{13}N and ^{15}O in the tunnel air via spallation reactions caused by the nucleons with the energy above 20 MeV. A yield of ^{41}Ar in air was estimated directly by taking into account a capture of thermal neutrons. All the nuclide concentrations were found to be quite low, and thus this low-activated water can be processed with the existing MSU systems.

Independently validated design basis air effluent

FRIB operation inherently activates air in the linac tunnel and the target building hot cell. Additionally gaseous releases associated with activated water in the facility result in normal operational effluent from the facility. This effluent is filtered with both activated charcoal and HEPA filters to remove a significant portion of the activated material from the gaseous effluent. This effluent is released to the environment through high velocity exhaust stacks on the top of the FRIB target building. The potential impact on the public from these releases must be conservatively evaluated to assure that regulatory release limits and ALARA goals (Table 1) can be met during operation. Actual exposure will be determined by monitoring and is anticipated to be significantly lower than these conservatively estimated releases.

Airborne consequence analysis was performed in two steps. First, the various sources of air activation and gaseous activated products were determined from radiation transport calculations. These included the tunnel air HVAC exhaust and hot cell air HVAC exhaust, as well as the gaseous releases from activated systems from the target facility hot off-gas system (HOG) and service building special mechanical off-gas system (SMOG). These sources were then evaluated for potential public consequence based on both decay and dispersion from the stack [11]. A key factor in this evaluation is the potential wind conditions at FRIB accounting for the normal annual variations in wind, the impact of surrounding buildings, and the potential location of public receptors. This evaluation was performed using scale model wind tunnel testing (Figure 10) and the local historical wind data for this area. An appropriate set of receptor locations were identified to provide a representative sample of receptor location (Figure 11). The results of the evaluation accounting for the conservative source term, radioactive decay in the time to reach the receptors, and dispersion as defined by the wind tunnel data show that the regulatory limits and MSU ALARA goals can be easily met.

Figure 10. Wind tunnel scale model

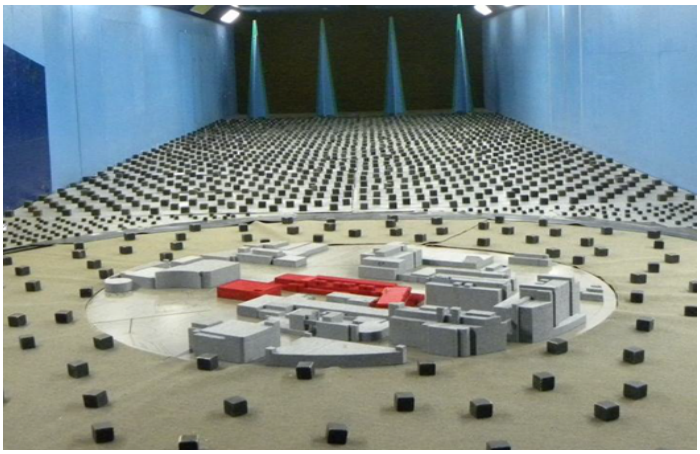

observed on the sides of the heat exchangers due to their significant size and small amount of shielding.

The contributions to the dose rates with no decay time allowed come mostly from short-lived nuclides ^{11}C, ^{13}N, and ^{15}O. Letting the radionuclide decay for 4 hours reduces the dose rates by more than two orders of magnitude, and ^{3}H and ^{7}Be become the dominant nuclides. However, as long as tritium remains contained by the plumbing, only ^{7}Be will be contributing to the dose rate outside the plumbing due to a low energy of electrons produced in the tritium decay.

Table 9. Dose equivalent rates (mrem/h) at a one foot distance from various components of the LCA system

– Tank/Device	– Side		– Top ("Face" for Heat Exchanger)	
	– 0 hours decay	– 4 hours decay	– 0 hours decay	– 4 hours decay
– Air Separator/GLS	– 4.801	– 2.373E-02	– 3.228	– 1.596E-02
– Heat Exchanger	– 2.307E+01	– 1.139E-01	– 2.918E-01	– 1.306E-03
– Expansion Tank	– 5.657	– 2.793E-02	– 4.320	– 2.135E-02
– DI	– 7.829	– 3.856E-02	– 7.605	– 3.756E-02
– Carbon Filter	– 7.829	– 3.856E-02	– 7.605	– 3.756E-02
– Pipe in Tunnel	– 2.190	– 1.086E-02	–	–

Table 10. Dose equivalent rates (mrem/h) at a one foot distance from various components of the CHA system

– Tank/Device	– Side		– Top ('Face' for Heat Exchanger)	
	– 0 hours decay	– 4 hours decay	– 0 hours decay	– 4 hours decay
– Air Separator/GLS	– 3.038E-01	– 1.506E-03	– 1.806E-01	– 8.898E-04
– Heat Exchanger	– 1.861	– 9.169E-03	– 3.121E-02	– 1.392E-04
– Expansion Tank	– 2.934E-01	– 1.449E-03	– 1.805E-01	– 8.894E-04
– DI	– 3.515E-01	– 1.735E-03	– 1.808E-01	– 8.904E-04
– Carbon Filter	– 3.515E-01	– 1.735E-03	– 1.808E-01	– 8.904E-04
– Pipe in Tunnel	– 7.780E-02	– 3.845E-04	–	–

Low-level liquid waste

There will be two more sets of tanks in the service building for Low Level Liquid Waste (LLLW). One set will store low-level activity water that is assumed to be condensed and collected on the HVAC cooling coils in the tunnel. The other set is for the condensed water from the tunnel walls and the magnets. Unlike the tanks in the two closed-loop systems, the LLLW tanks release activated vapour (humidity above the free surface) when additional water is added to the tanks and is released through the SMOG system to the environment. The activated water collected in LLLW will be removed as the tanks get filled, releasing the activated water vapour that has had a chance to decay in the LLLW tank. It was estimated that in the worst case mode as much as 9400 gallons of condensed water can be collected from the HVAC units in a full year operation. This mode of operation is unlikely, however, in the controlled climate of the facility.

Two sources of radionuclides in LLLW are possible: a direct production in water that has been already condensed, and production of the nuclides in the tunnel air with their

Table 8. Activities per unit volume and total activities of dominant radionuclides produced in water in the LCA and CHA systems for unlimited irradiation time (saturation) and no cooling time allowed

Radionuclide	LCA		CHA	
	Activity per unit volume [μCi/ml]	Total activity [μCi]	Activity per unit volume [μCi/ml]	Total activity [μCi]
^{3}H	1.53E-02	3.73E+05	1.59E-03	8.57E+03
^{7}Be	2.55E-03	6.21E+04	2.65E-04	1.43E+03
^{11}C	3.57E-04	8.70E+03	3.71E-05	2.00E+02
^{13}N	4.59E-03	1.12E+05	4.77E-04	2.57E+03
^{15}O	2.04E-02	4.97E+05	2.12E-03	1.14E+04

Dose rates at LCA and CHA systems

A further analysis allows calculations of the dose rates at the various components of the LCA and CHA systems using the estimated radionuclide concentrations. This was carried out with the code MicroShield6 [13]. Both the LCA and CHA systems have four types of cylindrically shaped tanks. These are air separators (Gas Liquid Separators, GLS), carbon filter tanks, ion exchangers (DI), and expansion tanks. There are two tanks of each type in each system. The tanks are located in a designated room in the service building. The tanks are not completely filled with activated water and have components inside which provide additional shielding against photons emitted from decaying radionuclides in water. In our calculations we assume that the tanks are filled with the water entirely. Thus, our calculations are conservative. There are also three heat exchangers in the LCA system and two in the CHA system, and regular pipes.

We assumed that a possible build-up of ^{7}Be anywhere in the LCA and CHA systems is insignificant and can be ignored. The build-up might occur due to ^{7}Be ions attaching to the plumbing if the water dynamics allows it. There are two factors, however, that suggest the low level of the build-up. First, the ions of ^{7}Be will be continuously removed from the systems by the ion exchange columns with efficiency of approximately 95% per cycle. Second, our collaborators from Spallation Neutron Source (SNS) reported that the build-up of ^{7}Be in their similar systems was insignificant. The dose rates were calculated, however, assuming that no ^{7}Be is removed from the LCA and CHA systems. Thus our calculations are conservative.

The dose equivalent rates at various components of the LCA and CHA systems are summarised in Tables 9 and 10. The dose rates were calculated at a distance of one foot from the components, assuming that the water in the system was irradiated for an infinite amount of time (saturation). The calculations were carried out for a moment immediately after the beam shut-down (0 hour delay), and 4 hours after the beam shut-down. We also assumed that no radionuclides are removed from water by any filters. The dose rates were calculated in two locations for each cylindrical tank assuming that these tanks are placed vertically: one foot from the cylindrical surface in the middle plane of the tank ("Side" in the tables); and one foot from the flat surface of the tanks ("Top" in the tables). Similarly, the dose rates were calculated in two locations for the heat exchangers: one foot from the middle point of the side surface ("Side" in the tables, the largest surface of the heat exchangers); and one foot from the middle point of the front or end surface ("Face" in the tables). Generally, the dose rates at the LCA components are more than an order of magnitude higher than those at the CHA components. The highest dose rate is

beam was 2.5×10^{15} 1/s, which corresponds to 400 kW of 1 GeV protons (beam power on the production target). It was found that the maximum dose rate reaches 1.8×10^{4} mrem/h. This dose rate is found at the front-end drop when the beam is lost in one of the locations in the second folding segment. The MSU ALARA stipulates that the dose rate stays below 2 mrem in any one hour for the workers. The limit of 2 mrem in any one hour is also a regulatory limit for the general public. Further assuming that the accelerator will be shut down after such an incident to investigate the reasons for the lost beam and therefore no more than one beam loss incident in any one hour is possible, we will need to detect such beam loss event and shut down the machine in 0.4 s. Note that the machine protection system is being designed to do so in just 35 μs. Therefore the beam loss incidents should not pose a risk to people from the standpoint of the prompt dose.

Activation of water services

There are several thousand gallons of water in two closed-loop systems at the FRIB linac. The LCA system (Low Conductivity Activated) will hold ≈6435 gallons to cool various beam line elements and magnets. Approximately, 1425 gallons in the CHA system (Chilled Activated) will be used for the HVAC units in the tunnel. Both systems will have an extensive plumbing and various purpose tanks in the linac tunnel and the service building above grade. Since this water is directly exposed to the radiation from the linac, we need to know both radionuclide concentrations and the total amount of radioactivity produced in these systems. These values are used in spill analyses of the activated water and in calculations of the doses to the workers from the activated water contained in the plumbing.

Radionuclide inventories in LCA and CHA systems

The dominant radionuclides produced in water in the accelerator environment are ^{3}H (tritium), ^{7}Be, ^{11}C, ^{13}N and ^{15}O [12]. These radionuclides are produced via spallation reactions induced by nucleons with the energy above 20 MeV. Fluxes of such nucleons were calculated in the LCA and CHA systems with MARS15 [4-6] for the normal beam losses (1 W/m) and the radiologically bounding proton beam. The fluxes were then converted into concentrations of the radionuclides of importance using a model described in [12]. The concentrations were calculated for broad ranges of the irradiation time (from 1 month to saturation) and the cooling time (from 0 to 1 year). The activities produced by ion beams at the same beam loss rate of 1 W/m are expected to be lower. The total activities were also calculated since the volumes of water directly exposed to the radiation in both systems are known. Both activities per unit volume and the total activities in the case of unlimited irradiation (saturation) and no cooling time allowed are summarised in Table 8. This case is the worst case scenario. The activities will decrease if a cooling time is assumed. For accident scenarios involving spills or leaks, the saturation case with no decay time should be used.

Figure 8. Dose equivalent rate distribution calculated above grade and expressed in units of mrem/h

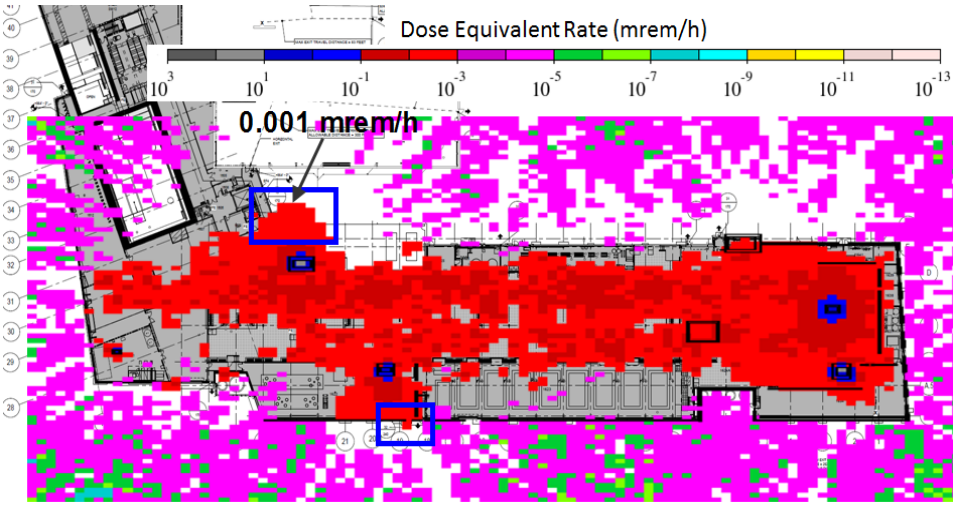

The blue boxes indicate publically accessible areas where the dose rate exceeds 0.001 mrem/h.

Figure 9. Plan view of the service building at the grade level

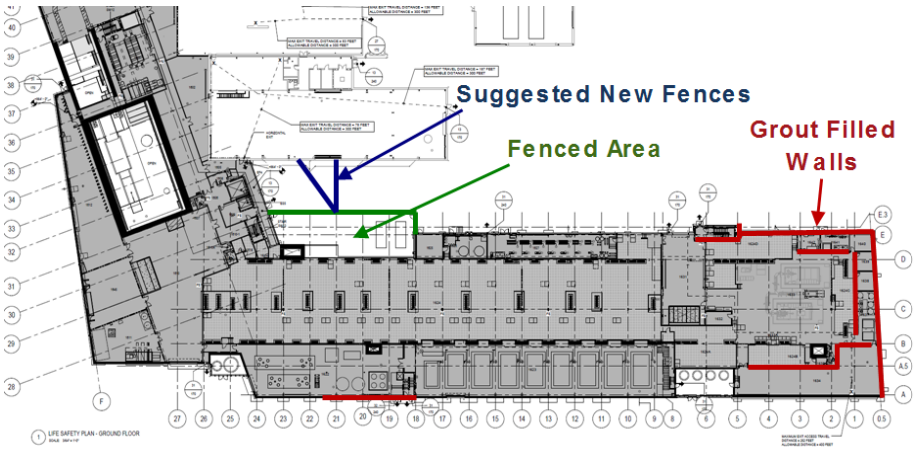

The red lines indicate building walls that are suggested to be filled in with grout. The green lines limit an area outside the service building that is planned to be fenced out. The blue lines show fence locations which will limit the public access to the area because the expected dose rate will exceed 0.001 mrem/h.

Prompt dose rates due to beam loss incidents

The dose equivalent rates in the service building above grade due to beam loss incidents were also evaluated. Radiologically bounding proton beams were used. We also assumed that the beam is completely stopped in a stopping target. This is rarely the case, however. Particle beams are not normally lost locally but rather on a stretch of accelerator because an actual beam has a size and particles in the beam have angular distribution. And, if the beam is lost due to a magnet failure, the field in the magnet changes slow enough to spread the beam losses over a section of the machine. Therefore, the assumption of the local beam losses will result in conservative estimates. The positions of the stopping target were selected to maximise to dose rates around the major penetrations, since the dose rate increase due to smaller conduits is not substantial. The intensity of the stopped

Prompt dose rates

As part of the design process, we need to ensure that the facility provides an adequate shielding so that the dose equivalent rates stay below the MSU ALARA goals for both the workers and the general public. In the case of prompt dose radiation at the FRIB linear accelerator, the limits apply to the areas above the surface (grade) only, because the machine was not designed to allow access into the beam enclosure during the operation. It is important to note that the facility is located on the MSU campus, and that the members of the general public can be present close to the facility walls. The dose rates must be evaluated for both the normal operation (1 W/m beam loss rate) and beam loss incident scenarios, and compared to both the personnel and general public dose limits. All the calculations for this purpose were performed with the MARS15 code [4-6] using a model that includes the linear accelerator, tunnel, all major penetrations and other conduits, and the walls of the service building above grade.

Prompt dose rates during normal operation

MSU ALARA stipulates that the annual doses should not exceed 500 mrem for the workers, and 10 mrem for members of the general public. These numbers translate into 0.25 mrem/h and 0.0018 mrem/h ALARA goals assuming that one working year during which the exposure of the workers to the radiation is possible is 2000 hours, and one operational year during which the general public can be exposed to is 5556 hours. We do not claim any credit for the general public to be around FRIB for only part of the year.

The dose equivalent rate above grade was calculated for the radiologically bounding beams: protons at 611 MeV in the second linac segment and the second folding segment, and protons at 1 GeV in the third linac segment. In addition, we added the beam losses for ^{18}O beam at 35 MeV/nucleon in the first linac segment and the first folding segment. These segments would not be used for protons. The resulting dose rate distribution is shown in Figure 8. The distribution is overlaid with a plan view of the facility. A number of recommendations were made based on this distribution for the purpose of protection of the general public: the walls of the service building constructed with CMU blocks should be filled with grout in several locations (see Figure 9); the fence on the north side of the building should be realigned to restrict access of the general public to that area; and the shielding above the surface for the cryogenic distribution shaft must be redesigned.

The dose map also confirmed that the dose rate is below 0.1 mrem/h everywhere in the service building with exception of the vicinity of the major penetrations. The dose rate of 0.1 mrem/h is in fact the MSU ALARA goal for the workers with additional safety margin of 2.5. A closer look at the dose rate around the major penetrations revealed that it is only a small numerical factor higher than 0.1 mrem/h and in relatively small areas with size in a scale of a meter. A number of mitigation strategies can be applied in these areas such as active monitoring, local shielding that would not impact the operation, stand-offs, and occupancy factors in locations where the workers are not expected to be during the entirety of their shift. Other penetrations such as conduits for radio-frequency wave guides appear to be small enough and well shielded to keep the dose rates in their vicinity below 0.1 mrem/h.

Figure 6. Plan view of model above the tunnel

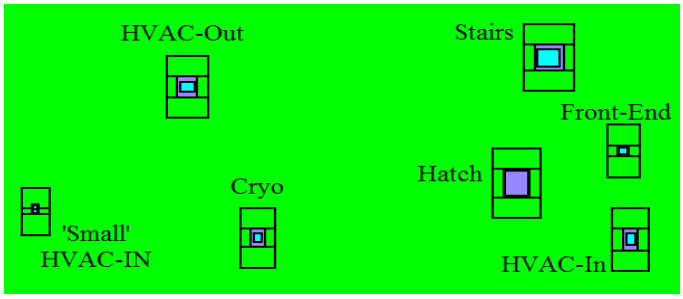

Volumes around the penetrations in which the star densities were calculated are shown.

Figure 7. Plan view of model above the tunnel

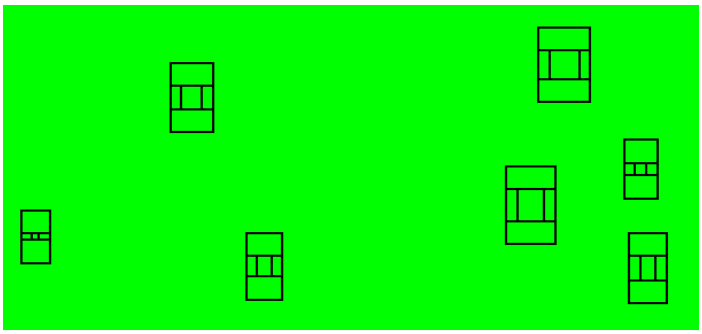

Volumes around the penetrations in which the star densities were calculated are shown. The model is similar to that shown in Figure 6, but the major penetrations were removed from it.

Table 7. Averaged star densities calculated in 3 m-thick volumes located around the major penetrations

Penetration	Averaged star density in model with major penetrations [1/cm^3/y]	Averaged star density in model with major penetrations removed [1/cm^3/y]	Star density increase due to penetration [%]
Front end	8.79E+07	8.15E+07	7.3
HVAC-In	4.52E+07	3.99E+07	11.7
East Hatch	1.89E+08	1.27E+08	32.5
Cryoline	6.68E+07	5.92E+07	11.3
Stairs	2.35E+06	1.87E+06	20.2
HVAC-Out	8.95E+07	7.76E+07	13.3
'Small' HVAC-In	5.83E+06	5.61E+06	3.8

Also shown are the averaged star densities calculated in the same volumes but in the model where the penetrations were removed.

Effect of major penetrations

The linac tunnel will be located approximately 6 m under the surface. This shielding of 6 metres (concrete and soil) is not solid, however. There is a number of small penetrations through the shielding like those for radio-frequency wave guides, cables and services, and several big penetrations. These major penetrations (see Figure 5) are the front-end drop; heating, ventilation and air conditioning inlet (HVAC-In); second (smaller) HVAC inlet ("Small" HVAC-In); HVAC outlet (HVAC-Out); hatch on the east side of the linac tunnel (East Hatch); stairwell on the north-east side of the linac tunnel; and cryogenic distribution shaft (Cryoline). Due to their substantial size, one expects an enhanced radiation streaming through them which, in turn, will increase the level of the soil and ground water activation. An effect of the major penetrations on the ground water activation was studied in two sets of calculations. The star densities were calculated in volumes surrounding these penetrations (see Figure 6). The volume size was chosen to be 3 m which approximately corresponds to the 99.9% volume as described in the previous sections. The star densities were compared to values obtained in the second set of calculations using the same model but with the major penetrations removed (Figure 7). The direct comparison between the two sets of star density values allows us to estimate the effect of the penetrations on the ground water activation. The calculations were performed for a constant beam loss of 1 W/m for radiologically bounding beams: protons at 611 MeV in the second linac segment and the second folding segment, and protons at 1 GeV in the third linac segment. The beam losses in the first linac segment and the first folding segment were ignored due to the fact that these segments would not be used for the proton beams, and that the energy of other ion beams in this segment will be as low as 20 MeV/nucleon or below. Table 7 provides the comparison between those two sets of star density values for each of the major penetrations. One can see that the values are less than 33% different. Thus the conclusions of our previous studies are not affected.

Figure 5. Three-dimensional rendering of the concrete structure of the linac tunnel and the service building

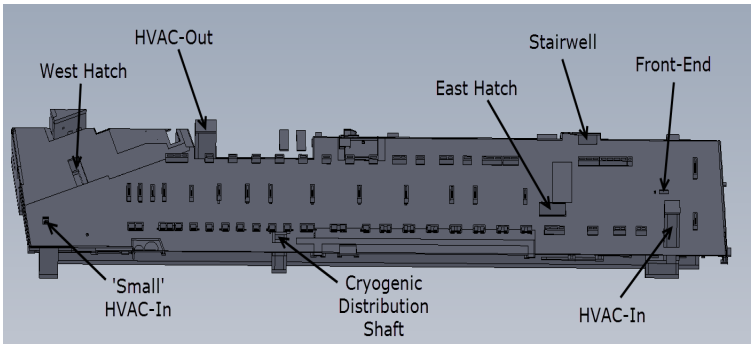

The area above the surface level is clearly seen. The major penetrations are indicated.

Figure 4 shows two star density distributions as a function of soil depth for both types of soil. Both distributions are similar which validates that the results previously obtained with the FNAL-type wet dirt are applicable to the FRIB site.

Table 6. Composition of averaged FRIB soil and FNAL-type wet dirt

Element	Z	A	Weight fraction (FNAL)	Weight fraction (FRIB)	Atomic fraction (FNAL)	Atomic fraction (FRIB)
H	1	1.00794	0.023	0.016	0.31	0.23
C	6	12.01100		0.028		0.035
O	8	15.99940	0.57	0.61	0.49	0.56
Mg	12	24.30500		0.020		0.012
Al	13	26.98154	0.071	0.034	0.036	0.018
Si	14	28.08550	0.33	0.21	0.16	0.11
K	19	39.09830		0.0094		0.0036
Ca	20	40.07800		0.060		0.022
Ti	22	47.88000		0.0022		0.00069
Fe	26	55.84500		0.014		0.0038

Figure 4. Star density distribution as a function of the soil depth

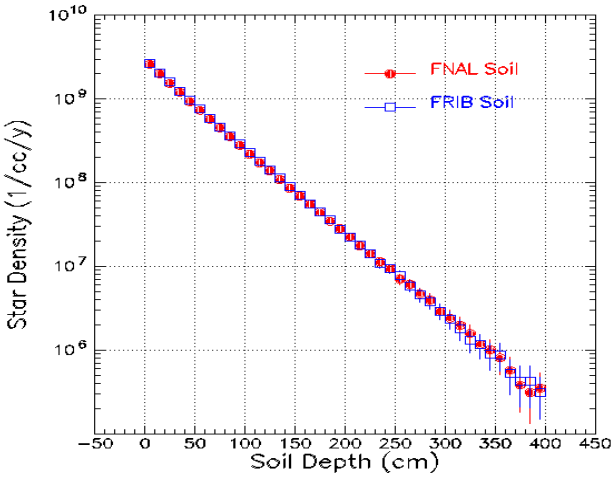

$\Sigma_i C_i/C_{i,max}$ must be less or equal to 1. The values of $C_{i,max}$ for drinking water are found in [3] and also summarised in Table 3. As the calculations for the considered model showed, the radionuclide concentrations calculated in the 99.9% volume are expected to stay below the regulatory limits for drinking water standards for all radionuclides of importance both separately and in sum. These calculations are conservative for a number of reasons. The thickness of the tunnel walls has been increased from 30 in to 36 in after these calculations where completed; ion beams will be used instead of radiologically bounding proton beams in the baseline configuration of the facility, and heavier beams are expected to produce even less activity in the ground water; and in addition to that, we do not expect that the saturation conditions will even be achieved due to the seasonal variations of the water table.

Table 3. Dominant radionuclide parameters and regulatory limits C_{max}

Nuclide	Half-life [y]	C_{max} [pCi/ml]	Atoms per Star (*K*-factor)
^{3}H	12.32	20	0.0250
^{22}Na	2.6027	0.4	0.00732

Table 4. Concentrations of radionuclides averaged over the volume containing 99% of activity

Irradiation 10 years			Irradiation 20 years			Saturation		
$C(^{3}H)$ [pCi/ml]	$C(^{22}Na)$ [pCi/ml]	$\Sigma_i C_i/C_{i,max}$	$C(^{3}H)$ [pCi/ml]	$C(^{22}Na)$ [pCi/ml]	$\Sigma_i C_i/C_{i,max}$	$C(^{3}H)$ [pCi/ml]	$C(^{22}Na)$ [pCi/ml]	$\Sigma_i C_i/C_{i,max}$
4.10	0.20	0.71	6.44	0.22	0.86	9.54	0.22	1.02

Table 5. Concentrations of radionuclides averaged over the volume containing 99.9% of activity

Irradiation 10 years			Irradiation 20 years			Saturation		
$C(^{3}H)$ [pCi/ml]	$C(^{22}Na)$ [pCi/ml]	$\Sigma_i C_i/C_{i,max}$	$C(^{3}H)$ [pCi/ml]	$C(^{22}Na)$ [pCi/ml]	$\Sigma_i C_i/C_{i,max}$	$C(^{3}H)$ [pCi/ml]	$C(^{22}Na)$ [pCi/ml]	$\Sigma_i C_i/C_{i,max}$
2.56	0.13	0.44	4.02	0.13	0.54	5.95	0.14	0.64

Comparison of FNAL and FRIB soil

Although the evaluation of the soil and ground water activation was performed using FNAL-type soil, a comparison between this type of soil and actual FRIB soil was also carried out. NTH Consultants, Ltd. [10] performed a geological survey taking a number of samples at various locations and depths (up to 75 ft) on the FRIB site. The moisture content and the element composition were determined. It was found that although the soil composition varies from sample to sample, the averaged composition and the density is somewhat similar to those of the FNAL-type soil. The soil compositions are compared in Table 6. The averaged density of the FRIB soil was found to be 2.257 g/cm^3 versus that of 2.24 g/cm^3 for the FNAL soil. To further validate the similarity, Monte Carlo calculations were conducted using a simple cylindrically symmetrical model with dimensions that resemble those found in the actual FRIB tunnel. Star density was calculated for both soil types. A beam of 1 GeV protons was used.

w_i is the weight of water divided by the weight of soil needed to leach 90% of the leachable radioactivity that is present (0.27 for ^{3}H and 0.52 for ^{22}Na);

λ_i is the inverse mean lifetime of the radionuclide of the type *i*, measured in units consistent with those of time *t* (e.g. years);

1.17×10^{6} is the numerical factor that converts disintegrations per second into *p*C*i* (0.037) and years into seconds (3.15×10^{7}).

The averaging of the activated water is taken into account by the geometry factor, *G*. A typical value of *G* found in the literature is 0.19 for beam lines and 0.019 for target stations not followed by long beam lines [8]. The factor was analytically calculated as a ratio of the star density averaged out to a radius where the star density has fallen to 1% of its peak value over the peak star density. The calculations were performed for a system with a certain cylindrical symmetry. Sometimes this approach is erroneously called a "99% volume" approach assuming that in these calculations 99% of all the activation is contained in the volume over which this procedure is performed. This is only approximately correct, especially for systems where there is no cylindrical symmetry. In the present calculations, however, we do not rely on the knowledge of the geometry factor. The previously calculated averaged star density is used as described above. This changes Equations (1) and (2) to:

$$C_i(t) = N_p \cdot S_{aver} \cdot K_i \cdot L_i \cdot (1.17\times10^{6} \cdot \rho \cdot w_i)^{-1} (1 - e^{\lambda i\, t}) \quad (3)$$

or in the limit of radionuclide saturation

$$C_i(t=\infty) = N_p \cdot S_{aver} \cdot K_i \cdot L_i \cdot (1.17\times10^{6} \cdot \rho \cdot w_i)^{-1} \quad (4)$$

In these equations, S_{aver} is the star density averaged over volumes containing either 99% or 99.9% of all the activity, and is $S_{max}\times G$. The rates of radionuclide production per star, K_i, are also calculated. We do not rely on the values originally presented in the radionuclide concentration model. The number of lost particles N_p is energy dependent and is calculated assuming a beam loss rate of 1 W/m.

As discussed in [7] and [9], only two radionuclides ^{22}Na and ^{3}H are of importance for FNAL soil types based upon the production rates, half-life time and the leachability by water. The leaching factor, L_i, is probably the most uncertain parameter of the model. It is a fraction of radionuclides that can be washed out by a representative amount of water. As discussed in [9], measurements were made of the number of radionuclides washed out of a sample of material exposed to a known amount of beam, by successive mixings of known amounts of water. For ^{22}Na, the amount washed out with each batch of water can be totalled and compared to the amount of activity initially present. This is not possible with the ^{3}H leaching measurements, due to the low energy of its beta decay and the analytical techniques employed. Only a product of the leachability and radionuclide production probability per star, K_i, can be measured for tritium.

The concentration model chooses to use the quantity of water that removes 90% of the leachable radionuclides, and uses this amount of the water as the basis for conversion from the soil density,ρ, to the density of water in the soil, ($\rho\ w_i$). The leachability for tritium in soil is 0.9, and has the meaning that the volume of water considered removes 90% of the amount of tritium that could be removed by continuing the washes to the necessary limit.

Table 3 summarises some parameters for the dominant radionuclides. *K*-factors were obtained from the simulations. Tables 4 and 5 show dominant radionuclide concentrations averaged over different volumes. The concentrations were calculated for three irradiation times: 10 years, 20 years and an infinite irradiation time ("saturation"). Beside the concentrations, the values $\Sigma_i C_i/C_{i,max}$ are also shown. The values are the sums of concentrations of all radionuclides of importance divided by maximum allowed concentrations in drinking water. The regulatory requirements stipulate that the value

Figure 3. Resulting star density distribution

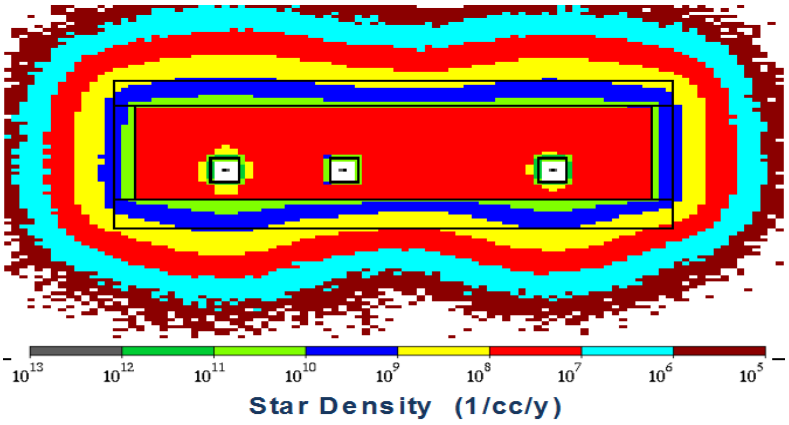

Table 2. Averaged star densities and limiting isocontour levels corresponding to 99% and 99.9% volumes

Volume	Averaged star density [1/cm^3/y]	Isocontour level [1/cm^3/y]
99%	2.99×10^8	1.13×10^7
99.9%	1.87×10^8	1.24×10^6

The isocontours levels can be used to determine "points of compliance" from Figure 3.

Nuclide concentrations

The averaged star densities are converted in radionuclide concentration using Radionuclide Concentration Model [7]. In the original model, the concentration C_i (in *pCi* per *ml*) for a radionuclide of the type *i* in water in proximity to the beam enclosure is expressed by:

$$C_i(t) = N_p \cdot S_{\max} \cdot G \cdot K_i \cdot L_i \cdot (1.17\times10^6 \cdot \rho \cdot w_i)^{-1} (1 - e^{\lambda_i t}) \quad (1)$$

or, in the limit of radionuclide saturation, by:

$$C_i(t=\infty) = N_p \cdot S_{\max} \cdot G \cdot K_i \cdot L_i \cdot (1.17\times10^6 \cdot \rho \cdot w_i)^{-1} \quad (2)$$

where:

N_p is the number of incident protons per year;

S_{max} is the maximum star density (in 1/cm^3) per incident proton in the soil or rock obtained from calculations carried out with radiation transport codes;

G is the geometry factor which takes into account mixing of the activated water in some volume;

K_i is the radionuclide production probability per star (0.075 atoms/star for ^{3}H, 0.02 atoms/star for ^{22}Na in the original model, calculated in simulations in our case and presented in Table 3);

L_i is the *leachability* factor for the radionuclide (0.9 for ^{3}H and 0.135 for ^{22}Na in soil);

ρ is the material density;

Activation of soil and ground water

Some activation of the soil and the ground water is expected at the FRIB linac due to normal beam losses. Whereas the actual beam losses will be determined during facility operation, the design requirement for the linac is to keep it below 1 W/m. The level of activation was evaluated for an assumed beam loss rate of 1 W/m and radiologically bounding beam of protons at 200 MeV in the first linac segment (see Figure 1), 611 MeV in the second segment, and 1 GeV in the third segment. The calculations were carried out in two steps. As the first step, the star density distribution was calculated around the linac tunnel using the radiation transport code MARS15 [4-6]. The concentrations of dominant radionuclides ^{3}H and ^{22}Na were estimated from the star density using Radionuclide Concentration Model [7] after that.

Star density distribution due to normal beam losses

Figure 2 shows a cross-section of the double-folded FRIB linac, the tunnel walls and the surrounding soil. The associated proton beam energies are also indicated in the figure. Fermilab-type wet dirt [6] with a density of 2.24 g/cm^3 was used as the soil (standard MARS15 material "SOIL"). The tunnel wall thickness used in the calculations was 30 in, and that of the tunnel roof is 42 in. The linac segments were represented with a stainless steel pipe surrounded with a box as cryogenic modules. The angle at which the beam particles entered the beam pipe material was set to 3 mrad with respect to the beam pipe surface, and the entry position is uniformly distributed both longitudinally and azimuthally. These assumptions are a simplification. In reality, a broader angular spectrum is possible, with the beam loss rate higher in focusing elements where the beam size is larger. The effect of the incident angle on the ground water activation was tested for angles 0.1 mrad, 3 mrad and 1 degree and no significant difference was found.

The resulting star density distribution with contribution from beam losses in all the segments is shown in Figure 3. The distribution is presented in units of 1/cm^3/y assuming that one operational year is 2×10^7 s (5556 h). It is recognised that a gradient in activity will be present from the edge of the facility. The soil and groundwater activation is assessed by assuming uniform mixing of the activated water over the assumed analysis volume. Activated soil and groundwater next to the tunnel wall poses no risk to the environment or the public. It must flow from this location to the "facility boundary" or "point of compliance" for the facility as described in the regulations. Therefore, the region can be assumed to effectively mix. The mixing of the water is taken into account by assessing the average star density over a volume that contains either 99% or 99.9% of the entire radioactivity generated in the soil. The 99% and 99.9% volumes were found to be restricted by isocontours located approximately 2 m and 3 m respectively from the concrete walls of the tunnel. These distances of 2 m and 3 m are measured against the segment 2 (611 MeV) and segment 3 (1 GeV) which are locations where the soil activity is maximum. In other places these isocontours are located even closer to the tunnel walls. The averaged star densities are summarised in Table 2.

Figure 2. Cross-section of linac model with surrounding soil and tunnel walls

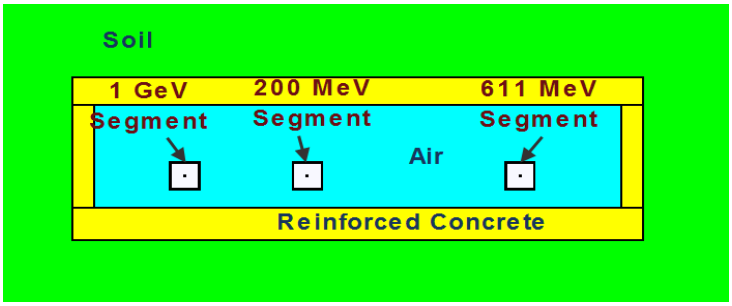

Figure 1. Schematics of the FRIB Facility and the experimental areas

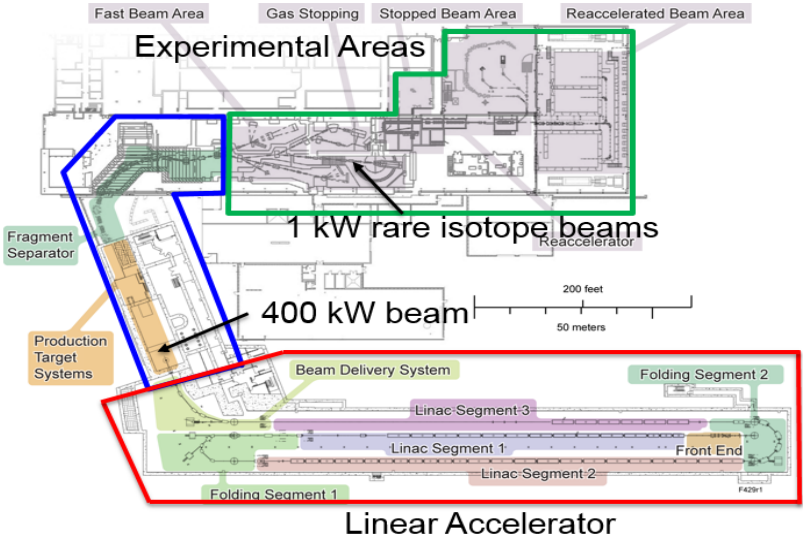

Regulatory protection criteria applied to FRIB

One of the goals of the radiation transport calculations is to provide input to the designers to verify that the facility meets the limits from various regulatory agencies and satisfy the MSU ALARA (As Low As Reasonably Achievable) goals both for the general public and the radiation workers. One key factor for this analysis is that FRIB is situated on the MSU campus where the general public is immediately outside the facility walls and not in a remote location. Although FRIB is largely funded by the US Department of Energy, the regulatory agencies include the US Nuclear Regulatory Commission (NRC), whose limits are the applicable regulations for this study. FRIB will be under an independent NRC license. Table 1 summarises various limits. The MSU ALARA goals are in general set to 10% of the limits imposed by the regulatory agencies. One distinctive difference is the self-imposed limits for the ground water activation. The limits for effluent water shown in Table 1 show the significant margin being applied to the design by using the drinking water limits. Groundwater near FRIB is not in contact with any source of drinking water nor public access. FRIB is relatively distant from the closest drinking water well and the aquifer is relatively deep under FRIB. Nonetheless, the design goal is to assure radiation protection for the ground water activation level by meeting the limits established for the drinking water.

Table 1. Regulatory radiation protection limits and MSU ALARA goals

Type of limit	Limits and goals	
Radiation dose – Worker	Standard [1]: 5,000 mrem/yr MSU ALARA Goal [2]: 500 mrem/yr	
Radiation dose – Public	Standard [1]: 100 mrem/yr and < 2 mrem/(any one hour) MSU ALARA Goal [2]: 10 mrem/yr and < 2 mrem/(any one hour)	
Air – maximum exposure to nearest receptor	Standard [1]: 10 mrem/y MSU ALARA Goal [2]: 1 mrem/yr	
Groundwater - effluent	^{3}H Standard [1]: 1,000 pCi/ml FRIB Design Goal: 20 pCi/ml (drinking water standard [3])	^{22}Na Standard [1]: 6 pCi/ml FRIB Design Goal: 0.4 pCi/ml (drinking water standard [3])

Evaluation of radiation environment at FRIB linac

Mikhail Kostin[1], Robert Lowrie[1,2], Reginald Ronningen[1]
[1]Facility for Rare Isotope Beams, US
[2]URS Corporation, US

Abstract

The Facility for Rare Isotope Beams (FRIB) at Michigan State University is a project jointly funded by the US Department of Energy and Michigan State University with the construction started in March 2014. This accelerator facility will use a broad range of primary ion beams from ^{16}O to ^{238}U with a beam power of up to 400 kW and energy of 200 MeV/nucleon for ^{238}U in its baseline configuration to produce rare isotopes. A possible facility upgrade will include increase of the beam energy up to 400 MeV/nucleon for ^{238}U and the addition of new light ion beams down to ^{3}He and protons for ISOL operations.

The work presented here is an overview of radiation transport calculations aimed to evaluate the radiological environment at the FRIB linac and adjacent areas. A number of calculations have addressed the impact on environment (activation of soil and ground water, evaluation of radionuclide releases); prompt radiation to the workers and general public due to normal beam losses and beam loss incidents; and activation of services.

This material is based on work supported by the US Department of Energy Office of Science under Cooperative Agreement DE-SC0000661.

Introduction

The Facility for Rare Isotope Beams (FRIB) is a new national user facility at Michigan State University (MSU). The facility is being built for the research in the fields of physics of nuclei, nuclear astrophysics, fundamental interactions, and applications for society. In its baseline configuration the facility will offer separation of isotopes in-flight for fast, stopped and reaccelerated secondary beams. A broad range of the primary ion beams will be utilised, from ^{16}O to ^{238}U with a beam power of up to 400 kW and energy of 200 MeV/nucleon for ^{238}U (higher for lighter primary beams) to produce rare isotopes. A possible facility upgrade will include an increase in the primary beam energy up to 400 MeV/nucleon for ^{238}U and the addition of new light ion beams down to ^{3}He and protons for Isotope-Online (ISOL) operations. A multi-user operation with simultaneous light and heavy primary beams is also considered.

FRIB will consist of two major systems: a double-folded linear accelerator which will deliver a primary ion beam to a rare isotope production facility, consisting of a high-power target connected to a fragment separator for providing secondary rare isotope beams for science experiments (see Figure 1). This paper provides an overview of the radiation transport calculations performed in support of the design of the FRIB linear accelerator and its radiation shielding with focus on human and environmental impact issues rather than on the design of specific beam line elements.

Conclusions

Several metallic and soil samples were irradiated at the H4IRRAD test facility. Gamma spectrometry and beta scintillation analysis (leached water only) were performed to determine the radioactivity induced in the samples. Conversion coefficients from unit lost beam power to induced specific activity at saturation were calculated for each radionuclide produced in metallic samples. FLUKA simulations were carried out to estimate the concentration of ^{3}H in the soil. Two leaching procedures were used and compared to quantify the amount of radioactivity leached out of the soil into the water. The mixing system was able to remove up to 39% of ^{3}H and 12% of ^{22}Na from the irradiated soil.

Acknowledgements

The authors would like to thank A. Dziewa, F. Malacrida and A. El Gares for performing the gamma spectrometry and the liquid scintillation measurements. The authors are grateful to M. Calviani, M. Brugger and the H4IRRAD team for allowing the irradiation of the samples and for providing the FLUKA geometry of the facility.

References

[1] R. Froeschl, F.P. La Torre and N. Walter (2012), "The ActiWiz material composition catalogue", CERN Technical Report, CERN-RP-2012-002-REPORTS-TN.

[2] R. Froeschl, FP. La Torre, S. Sgobba, C. Theis, H. Vinke, N. Walter (2012), "Radiological Hazard classification of material in CERN's accelerators", CERN Technical Report, CERN-DGS-2012-003-RP-IR.

[3] F.P. La Torre, M. Silari (2014), "Leaching of radionuclides from activated soil into groundwater", CERN Technical Report, CERN-RP-2014-012-REPORTS-TN.

[4] S. Sgobba (2006), "Material for high vacuum technology: an overview", CERN-TS/2006-004 (MME), EDMS 773904.

[5] S. Sgobba (2009), "Physics and measurements of magnetic materials", CERN Accelerator School CAS 2009: Specialised Course on Magnets, Bruges, 16-25 June 2009.

[6] J.M. Jimenez, B. Henrist (2004), "Vacuum Chambers for the Circulating Beams in the LHC Injection and Extraction Septa", Functional Specification, LHC-VCRS-ES-0001 rev. 1.0, EDMS 405734, (MUMETAL).

[7] S. Claudet et al. (2004), "Two 100 m Invar transfer Lines at CERN: design principles and operating experience for helium refrigeration", CERN-AT-2004-021-ACR.

[8] B. Biskup, M. Brugger, M. Calviani, I. Efthymiopoulos, R. Kwee, J. Mekki, F.P. La Torre, E. Lebbos, P. Mala, G. Manessi, A. Nordt, F. Pozzi, K. Roeed, C. Severino, M. Silari, A. Thornton (2011), "Commissioning and Operation of the H4IRRAD Mixed-Field Test Area", CERN Technical Note, CERN-ATS-Note-2011-121 PERF.

[9] A. Ferrari, P.R. Sala, A. Fasso, J. Ranft (2005), "FLUKA: A Multi-particle Transport Code", CERN-2005-10, INFN/TC_05/11, SLAC-R-773.

[10] G. Battistoni, S. Muraro, P.R. Sala, F. Cerutti, A. Ferrari, S. Roesler, A. Fasso, J. Ranft (2007), "The FLUKA code: description and benchmarking", *Proceedings of the Hadronic Shower Simulation Workshop 2006*, Fermilab 6-8 September 2006, M. Albrow, R. Raja Eds., AIP Conference Proceeding 896, 31-49.

Table 5. Specific activity of ^{3}H and ^{22}Na measured in leached water after correction for the decay and the concentration for the mixing system

Mixing time	Specific Activity (Bq/l)	
	^{3}H $(t_{1/2} = 12.32\ \mathrm{y})$	^{22}Na $(t_{1/2} = 2.6\ \mathrm{y})$
8 hours	518 ± 31	96.7 ± 5.8
1 month	541 ± 32	131 ± 8
2 months	542 ± 32	136 ± 8
4 months	542 ± 33	144 ± 9

Table 6. Specific activity of ^{3}H and ^{22}Na measured in the leached water including decay correction for the flowing system

Wash	Specific Activity (Bq/l)	
	^{3}H $(t_{1/2} = 12.32\ \mathrm{y})$	^{22}Na $(t_{1/2} = 2.6\ \mathrm{y})$
1	384 ± 23	126 ± 6
2	3.23 ± 0.93	12.7 ± 0.9
3	1.67 ± 0.90	3.15 ± 0.22
4	2.05 ± 1.09	4.71 ± 0.54

Fraction of radioactivity leached out

The activity concentration of the leached water for both systems was compared with the radioactivity measured in the activated soil in order to estimate the fraction leached out. Figure 2 shows the ratio between the total activity measured in the leached water and the total activity measured in the activated soil for ^{3}H and ^{22}Na, the two radionuclides of major interest in this study. Since the liquid scintillation analysis cannot be performed on the soil, the tritium activity measured in the leached water was compared with the tritium estimated in the soil by the FLUKA simulations. Most of the radioactivity leached into the water just after 8 hours of mixing time (mixing system) or after the first wash (flowing system). In the first case, the longer the soil is mixed with the water, the more radioactivity leaches out. After two months of stirring, 39% of the ^{3}H and 11% of the ^{22}Na are leached by water. For the flowing system, the leachable fraction after one wash is 27% for ^{3}H and 10% for ^{22}Na. As from the second wash, the leachable fraction falls down to a fraction of per cent for both radioisotopes.

Figure 2. Cumulative fraction of ^{3}H and ^{22}Na activities extracted by water from the activated soil for both systems

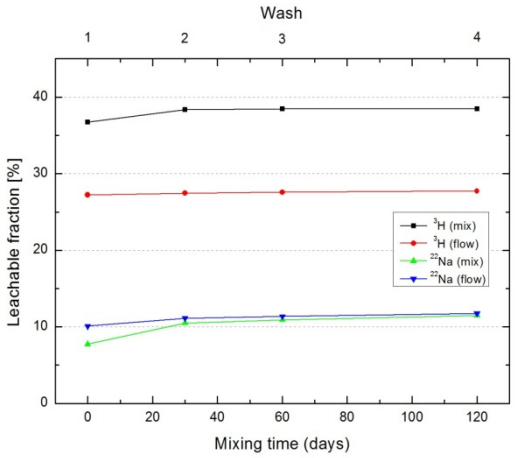

Table 4. Conversion coefficients from unit lost beam power to induced specific activity at saturation

Nuclide	$t_{1/2}$	Conversion coefficient $A_S(Bq/g/W)$				
		304L	316L	316LN	INVAR	MUMETAL
^{7}Be	53.1 d	5.43E+04	/	3.16E+04	1.56E+05	1.81E+05
^{22}Na	2.6 y	1.23E+04	8.47E+03	5.20E+03	1.17E+04	1.90E+04
^{46}Sc	83.8 d	2.59E+05	1.98E+05	1.23E+05	1.94E+05	1.21E+05
^{48}V	16 d	5.30E+05	4.75E+05	4.80E+05	5.01E+05	4.94E+05
^{51}Cr	27.7 d	2.40E+06	1.90E+06	1.18E+06	2.04E+06	1.38E+06
^{52}Mn	5.59 d	3.71E+05	3.98E+05	7.25E+05	8.86E+05	5.38E+05
^{54}Mn	312 d	2.43E+06	2.03E+06	1.17E+06	2.84E+06	1.27E+06
^{56}Co	77.3 d	1.78E+05	1.78E+05	1.41E+05	7.73E+05	1.48E+06
^{57}Co	272 d	5.67E+05	6.05E+05	4.75E+05	3.44E+06	5.53E+06
^{58}Co	70.9 d	6.03E+05	7.10E+05	5.71E+05	3.24E+06	5.89E+06
^{59}Fe	44.5 d	/	4.60E+03	2.98E+03	1.52E+04	2.38E+04
^{60}Co	5.27 y	7.41E+04	7.00E+04	3.57E+04	1.95E+05	3.50E+05
^{75}Se	120 d	/	/	1.43E+03	/	6.78E+03
^{83}Ru	86.2 d	/	/	5.49E+03	/	1.73E+04
^{88}Y	107 d	3.25E+03	2.27E+04	1.99E+04	/	7.19E+04
^{88}Zr	83.4 d	1.64E+03	1.26E+04	1.03E+04	/	3.89E+04
^{95}Nb	115 d	/	1.74E+04	1.41E+04	/	5.53E+04
^{133}Sn	115 d	2.07E+03	/	/	/	4.87E+04

Leaching techniques for activated soil

Two leaching possibilities were investigated: water stagnation with irradiated soil (mixing system) and water percolation through the irradiated soil (flowing system). To measure the amount of radioactivity passed from the irradiated soil to the water in both systems, leach water samples were systematically measured by gamma spectrometry and by scintillation analysis.

In the mixing system, 100 g of the irradiated soil was placed in a graduated flask together with 1 litre of distilled (tritium free) water. After vigorous shaking to disperse the soil in the water, the mixture was stirred for 8 hours. To measure the radioactivity leached out, a 100 ml sample of the hazy water was filtered through a Millipore filter (0.45 µm). The gamma activity in the water was measured with a Germanium detector as discussed above while β emitters were measured with a liquid scintillation spectrometer after distillation. Activated soil and water were in contact for 4 months and the analyses on the leached water were repeated after 1, 2 and 4 months. The results for the mixing system are shown in Table 5.

In the flowing system, a sample of 100 g of irradiated soil was placed in a funnel with a Millipore filter (0.45 µm) connected to a graduated container. A glass separatory funnel was placed over the funnel and filled with 1 litre of distilled (tritium free) water. The glass stopcock allowed controlling the rate of addition of the water to 125 ml/hr. The gamma activity in the water was measured with a Germanium detector while β emitters were measured with a liquid scintillation spectrometer after distillation. The whole procedure was repeated after 1, 2 and 4 months. The results for the flowing system are shown in Table 6.

Table 3. Specific activity of material samples irradiated at H4IRRAD, after 10 days of cooling time

Nuclide	$t_{1/2}$	Specific Activity (Bq/g)						
		304L	316L	316LN	INVAR	MUMETAL	Soil	Water
^{3}H	12.32 y	/	/	/	/	/	14.1 ± 0.3*	28.9 ± 2.6
^{7}Be	53.1 d	30.4 ± 10.7	/	17.7 ± 5.8	87.8 ± 27	102 ± 25	425 ± 32	523 ± 48
^{22}Na	2.6 y	0.49 ± 0.08	0.34 ± 0.07	0.21 ± 0.04	0.47 ± 0.11	0.76 ± 0.15	12.5 ± 0.8	/
^{46}Sc	83.8 d	101 ± 9	77. ± 7.7	48.2 ± 3.7	75.7 ± 7.6	47.1 ± 4.2	3.02 ± 0.19	/
^{48}V	16 d	554 ± 97	497 ± 99	501 ± 100	524 ± 152	516 ± 139	9.33 ± 0.50	/
^{51}Cr	27.7 d	2048 ± 307	1619 ± 259	1004 ± 161	1744 ± 366	1176 ± 282	25.0 ± 2.3	/
^{52}Mn	5.59 d	273 ± 87	294 ± 91	534 ± 144	653 ± 287	396 ± 174	6.01 ± 0.43	/
^{54}Mn	312 d	287 ± 29	239 ± 24	138 ± 14	336 ± 34	151 ± 15	6.02 ± 0.42	/
^{56}Co	77.3 d	74.4 ± 6.0	74.1 ± 6	58.7 ± 4.1	323 ± 23	620 ± 43	0.40 ± 0.04	/
^{57}Co	272 d	76.4 ± 9.2	81.5 ± 9.8	64.0 ± 7.7	464 ± 56	746 ± 82	/	/
^{58}Co	70.9 d	270 ± 27	318 ± 32	256 ± 26	1451 ± 145	2639 ± 237	0.22 ± 0.05	/
^{59}Fe	44.5 d	/	2.93 ± 1.1	1.90 ± 0.66	9.67 ± 2.9	15.1 ± 3.8	/	/
^{60}Co	5.27 y	1.48 ± 0.15	1.40 ± 0.14	0.71 ± 0.07	3.88 ± 0.39	6.97 ± 0.63	/	/
^{75}Se	120 d	/	/	0.41 ± 0.18	/	1.94 ± 0.73	/	/
^{83}Ru	86.2 d	/	/	2.10 ± 0.59	/	6.60 ± 1.98	/	/
^{88}Y	107 d	1.03 ± 0.19	7.20 ± 0.72	6.30 ± 0.63	/	22.8 ± 2.0	/	/
^{88}Zr	83.4 d	0.64 ± 0.34	4.93 ± 0.79	4.03 ± 0.60	/	15.3 ± 2.29	/	/
^{95}Nb	115 d	/	13.0 ± 2.4	10.5 ± 2.4	/	41.2 ± 9.1	/	/
^{133}Sn	115 d	0.62 ± 0.33	/	/	/	14.5 ± 2.3	/	/

*From FLUKA simulations.

Conversion coefficients for metallic samples

The conversion coefficients obtained in this work should be regarded as an upper limit of the induced radioactivity that can be expected in materials irradiated by the secondary radiation generated by high-energy protons (beam losses) stopped in target-like objects (e.g. collimators). Since the samples were exposed very close (~ 1 cm) to the target, which is thick enough to develop most of the hadronic cascade, these coefficients should be considered conservative. In cases where the material exposed to the secondaries is at a larger distance and/or the component where the beam loss occurs is not so thick, the specific activity induced in the material will be lower.

The induced radioactivity in the materials nearby the beam loss evolves with time according to the well-known expression:

$$A(t) = A_S[1 - exp(-t_{irr}/\tau)]exp(-t_{cool}/\tau) \quad (1)$$

where $A(t)$ is the activity at time $t = t_{irr} + t_{cool}$, A_S is the saturation activity, τ is the mean life of the radionuclide of interest, t_{irr} and t_{cool} are the irradiation time and the cooling time.

Let us assume a continuous loss of 1 W of beam power, on average, on a collimator. The value of 1 W is a fairly representative figure and the results can easily be scaled to a different power loss. Using Equation (1) one can calculate the specific activity at saturation A_S for the radionuclides of Table 3. Normalising A_S to 1 W of beam loss, we obtain the conversion coefficients from unit lost beam power to induced specific activity at saturation for the radionuclides produced in each material (Table 4).

as a function of the irradiation time as recorded during the experiment: for the long-lived radionuclides of interest in the present study, the irradiation can be considered constant over the entire period (about 18 days).

Figure 1. Irradiation profile of the samples

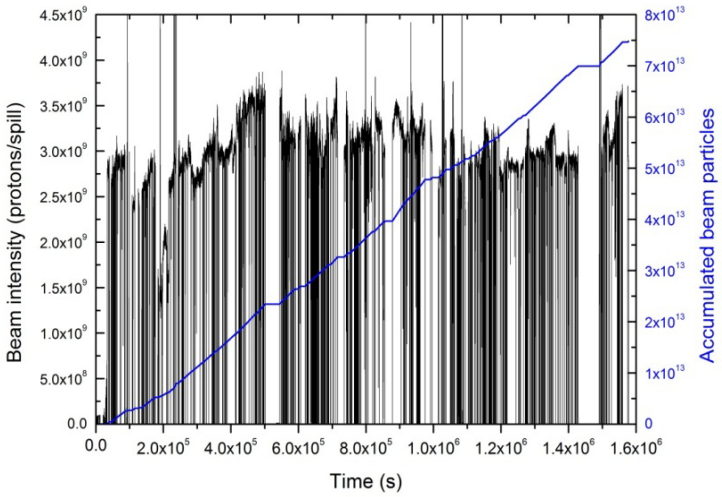

The number of protons in each spill (left scale) is shown together with the accumulated total number of protons (right scale).

Gamma spectrometry results

Immediately after irradiation with ~7.5×10^{13}accumulated protons, the dose rate of the samples was of the order of a few mSv/h. Most of this radioactivity was due to very short half-life radioisotopes. Since the radioisotopes of interest to this study have medium or long half-life, the samples were allowed to decay for at least 10 days before counting. The activated samples were measured with a high sensitivity, low-background, high-purity germanium (HPGe) detector by Canberra. The data acquisition and analysis was carried out using Canberra's Genie-2000 spectrometry software and the PROcount-2000 counting procedure software. This is a comprehensive software package for data acquisition, display and analysis, which includes a set of advanced spectrum analysis algorithms providing a complete analysis of gamma ray spectra. Several gamma spectrometry analyses were performed for each sample at various cooling times up to 2 years.

The soil samples could not be directly counted for ^{3}H due to the low beta-particle endpoint energy (18 keV), which is absorbed in the sample. For this reason, the tritium activity in the soil was estimated via Monte Carlo calculations with the FLUKA code [9,10]. The tritium activity in the water was determined using a liquid scintillation counter (Packard TRI-CARB 3180TR/SL), measuring a mixture of 8 ml of activated water and 12 ml of so-called liquid scintillation cocktail (Packard Ultima Gold LLF). In the case of high precision measurements, distillation is usually recommended requiring well controlled conditions where other radionuclides present in the sample (e.g. ^{22}Na) may significantly increase the result for tritium. This was not needed in the present case, as the potential interference of other radionuclides in the tritium pulse-height window was negligible.

The results of the gamma spectrometry for all samples and of the tritium measurement for the irradiated water after 10 days of cooling time are shown in Table 3. Quoted errors include statistical and systematic uncertainties of the gamma spectrometry analysis and liquid scintillation analysis.

properties, high magnetic permeability for low magnetic fields and small hysteresis effect. Vacuum chambers in the LHC injection and extraction septa were manufactured with MUMETAL [6]. The last sample is a Ni-Fe alloy called INVAR and used for the LHC helium transfer lines [7]. Table 1 shows the chemical composition of the metallic samples.

The soil samples were collected on the Prévessin site of CERN at a depth of 24 m. CERN is located in the Geneva basin, which is filled by sedimentary deposits called "molasse". The chemical analysis of the molasse rock was carried out by the EMPA laboratory in Dübendorf (Switzerland) via X-ray fluorescence spectrometry (WD-XRF). The results of the chemical analysis are shown in Table 2. The natural water content of the soil (moisture) was measured in CERN Environmental laboratory by drying a known amount of earth. The soil moisture content may be expressed by weight as the ratio of the mass of water present to the dry weight of the soil sample. To determine this ratio, the samples and container were weighed in the laboratory both before and after drying, the difference being the mass of water originally in the sample. The water content measured in the soil specimen was 5% by weight.

Table 1. Chemical composition in mass fraction (g/100 g) of metallic samples irradiated at H4IRRAD [2]

Element	Steel 304L	Steel 316L	Steel 316LN	INVAR	MuMetal
Density	8	7.99	8	8	8.75
C	0.03	0.03	0.03	/	0.011
Co	< 0.2	< 0.2	< 0.2	/	0.01
Cr	17 - 20	16 – 18.5	16 – 18.5	/	0.03
Cu	/	/	/	/	5.04
Fe	balance	balance	balance	64	13.8
Mg	/	/	/	/	0.015
Mn	2	2	2	/	0.57
Mo	/	2 – 2.5	2 - 3	/	4.02
N	/	0.05	0.14 – 0.2	/	/
Ni	10 – 12.5	11 - 14	12 - 14	36	76.4
P	< 0.045	< 0.03	< 0.045	/	0.002
S	< 0.03	< 0.01	< 0.015	/	/
Si	1	1	1	/	0.05

Table 2. Chemical composition of dried soil (density: ~1.4 g/cm^3)

Element	O	Si	Ca	Al	C	Fe	Mg	K	Na	Ti
(g/100 g)	38.8*	24	16	6.8	5*	4	2	1.9	0.7	0.42
Element	Mn	Ba	P	Sr	Zn	Cr	Zr	Eu	Ni	S
(g/100 g)	0.11	0.06	0.06	0.05	0.03	0.02	0.02	0.01	0.01	0.01

*Extrapolated value, not quantifiable by XRF analysis.

Irradiation facility and sample activation

The activation experiment was carried out at the H4IRRAD Facility which is installed in one of the secondary beam lines (H4) from the SPS in the CERN North Area [8]. The samples were installed under the copper target (8 cm in diameter and 100 cm in length) struck by the SPS primary proton beam with momentum of 400 GeV/c and average intensity of about 3×10^9 protons per pulse (over a supercycle of about 45 seconds and an extraction length of ~5 seconds). An argon ionisation chamber (XION) placed in the H4 beam line just upstream of the copper target monitored the intensity of the primary beam. Figure 3 shows the beam intensity profile and the accumulated number of protons

Induced radioactivity in accelerator materials and soil-shield samples

Francesco Paolo La Torre, Marco Silari
CERN European Organisation for Nuclear Research, Switzerland

Abstract

Several samples of materials used for accelerator components and shielding structures were irradiated in the high-energy stray radiation field of the H4IRRAD Facility, installed in one of the secondary beam lines (H4) from the SPS at CERN. After irradiation, the induced radioactivity of the samples was measured by gamma spectrometry at various cooling times up to 2 years, allowing identification of isotopes with a wide range of half-lives. The activation of soil-shield samples was also studied in detail. In particular, the mechanism and probability that the radioactivity produced in soil and ground water may transfer from the site of activation to the environment was investigated. Two techniques were used to quantify the amount of radioactivity leaching in the groundwater. Furthermore, the isotope production and their specific activities measured in the soil were simulated with the FLUKA Monte Carlo code.

Introduction

The operation of high-energy accelerators leads to nuclear activation of the surrounding material due to particle interactions in accelerator components, beam transfer line elements and shielding structures. A detailed estimation of the induced radioactivity is required in order to keep the impact on personnel and environment as low as reasonably achievable. A total of 30 material samples were collected from machine and shielding components manly used in the Large Hadron Collider (LHC) as well as in other CERN accelerator environments [1,2]. The samples were irradiated in a high-energy stray radiation field in a series of experiments recently performed at the H4IRRAD Facility at CERN.

The preliminary results on measured specific activities for seven samples are presented in this work. Conversion coefficients from unit lost beam power to induced specific activity at saturation for five metallic samples are shown. The activation of soil-shield samples was also studied in detail [3]. In particular, the mechanism and probability that the radioactivity produced in soil and ground water may transfer from the site of activation to the environment was investigated. Two techniques were used to quantify the amount of radioactivity leaching in the groundwater.

Material sample description

The AISI 304L steel is a general-purpose grade widely used for vacuum applications. At CERN it is mainly used in flanges and interconnections of the LHC vacuum vessel [4,5]. The AISI 316L steel is a molybdenum-containing grade. Due to its corrosion resistance, ductility and increased austenitic stability, this grade is used for specific application in the LHC interconnections. AISI 316LN is a nitrogen containing stainless steel. Both 316L and 316LN grades are widely used in the LHC main dipole cold masses (shell, insert, cover, plate, cold bore tubes, etc.) [4,5]. MUMETAL is a nickel-steel alloy with high magnetic

Session II: Induced Radioactivity

Chairs: Hiroshi Nakashima and Sayed Rokni

Summary

CENNS is extremely important for particle and nuclear physics and astrophysics. We are developing the Fermilab BNB at Fermilab as a low-energy neutrino facility for a first measurement of CENNS. We plan to operate a 1-tonne-scale, single-phase, LAr scintillation detector (possibly the MiniCLEAN detector) at a far-off-axis location. We performed fast neutron measurement in 2012 to survey the beam-induced neutron flux near the BNB target. Our calculations based upon these results suggest that a few metres of concrete are sufficient to attenuate these neutrons to acceptable levels for a first CENNS measurement. A second set of neutron measurements was scheduled for summer 2014 to more precisely assess the neutron energy spectrum, flux, and direction and to validate shielding design Monte Carlo simulations for the future experiment.

The CENNS experiment at the BNB represents a new class of accelerator-driven rare search physics experiments. A typical feature of all these experiments is the reduction of beam-induced backgrounds, namely neutrons. We have developed techniques to precisely measure high-energy neutron fluxes, energy spectra, and direction spectra. These techniques are valuable to the radiation shielding community. Our proposed technique to systematically configure shielding to modulate the detected neutron spectrum is unique.

References

[1] D. Z. Freedman (1974), *Phys. Rev. D*9, 1389.

[2] A. de Gouvea, K. Pitts, K. Scholberg, and G.P. Zeller (conveners), et al. (2013), "Neutrinos", Intensity Frontier Neutrino Working Group response to the Snowmass charge; arXiv:13010.4340v1.

[3] http://science.energy.gov/~/media/hep/hepap/pdf/May%202014/FINAL_DRAFT2_P5Report_ P5 Report (2004).

[4] S. Brice et al. (2014), CENNS Collaboration, *Phys. Rev. D*89, 072004; arXiv:1311.5958.

[5] Eljen Technology, Sweetwater, TX 79556, www.eljentechnology.com.

[6] R. Tayloe et al. (2006), *Nucl. Instrum. Meth. A*562, 198.

[7] R. Cooper et al. "SciBath: A Novel Tracking Particle Detector for Measuring Neutral Particles Underground", *Proceedings of the DPF-2011 Conference*, Providence, RI; arXiv:1110.4432.

[8] A. Hime (2011), "The MiniCLEAN Dark Matter Experiment", Proceedings of the DPF-2011 Conference, Providence, RI; arXiv:1110.1005.

[9] A.A. Aguilar-Arevalo, et al. (2012), "Low Mass WIMP Searches with a Neutrino Experiment: A Proposal for Further MiniBooNE Running"; submitted to the Fermilab PAC; arXiv:1211.2258.

[10] R. Dharmapalan, et al. (2013), "A Proposal to Search for Dark Matter with MiniBooNE", www.fnal.gov/directorate/program_planning/Jan2014PACPublic/MB_Request_2013_v2.pdf.

Figure 4. (a) Proposed site for a future CENNS experiment, (b) the 5-kg array of EJ-301 neutron detectors

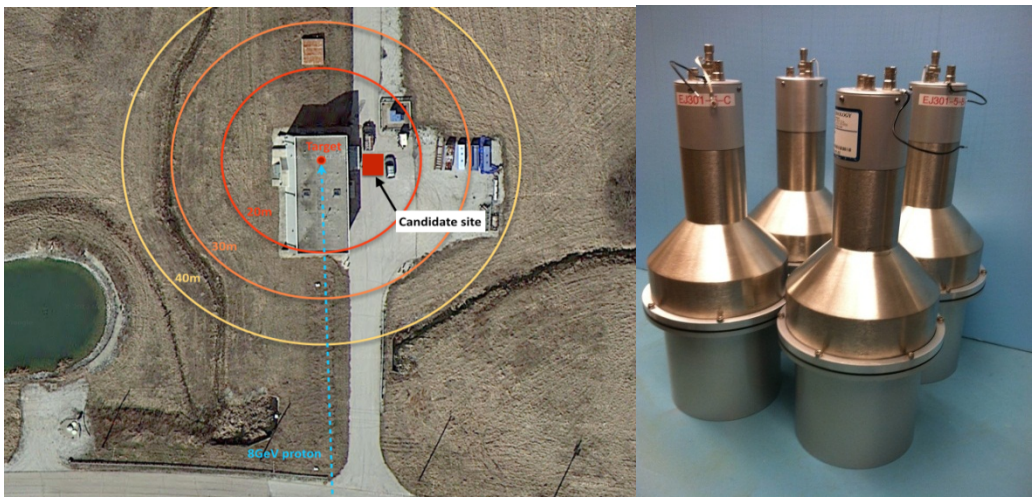

Improved SciBath detector

In the previous measurement, the limiting systematic error was our understanding of the detector gain and calibrations. Before delivering SciBath to the BNB in August 2014, we will improve our knowledge of this systematic. The light output of our current mineral oil-based scintillator will be measured with a series of off-line sample tests. We will also perform similar light yield tests by replacing our current scintillator with EJ-309 or linear alkylbenzene (LAB). Oxygenation is known to significantly reduce organic scintillator light yield. Therefore, nitrogen bubbling to remove any dissolved oxygen is an important systematic to control during these tests. Concurrently, a rigorous calibration programme to more precisely extract the energy-to-light yield conversion factor will be performed.

A custom, transport trailer is being designed to facilitate moving SciBath to other interesting locations. We will produce a map of the high-energy neutron flux and direction at multiple points around the BNB target building and will use a combination of pre-existing concrete blocks on the Fermilab campus to rapidly assemble a shielding structure to surround the SciBath trailer. We will also use large, commercially available tanks of water to modulate the incoming neutrons. With these shielding structures, we hope to validate the potentially complex neutron shielding simulations with neutron measurements.

CENNS-10 detector

The CENNS-10 detector is a 10-kg fiducial volume, single-phase LAr scintillation detector. The main goal of the CENNS-10 detector is to understand the detector response and necessary experimental configurations at the practical site of the experiment: detector energy thresholds, beam-induced background response, timing characteristics of the in-beam and out-of-beam events, shielding performance, etc. CENNS-10 consists of a 9-inch diameter inner chamber and a 12-inch diameter outer vacuum jacket. A cooling head equipped with a cryocooler and a heat exchanger module consistently circulate the argon through a hot-getter for argon purification. Two 8-inch PMTs (HAMAMATSU R5912-02MOD) view the active LAr detector volume for the scintillation light readout. The PMT siganal waveform will be used to discriminate between electron- and nuclear-recoil events. The cryogenic components of the detector are currently being commissioned. The full commissioning of the entire detector system and a calibration programme started in summer 2014. The detector operation at the BNB site is expected to begin in spring 2015.

The MiniCLEAN experiment has shown that a high level of PSD rejection is possible in large volumes of LAr [8].

For a 1-tonne detector with a 50% detection efficiency (mostly from PSD efficiency) and a low-energy threshold of 25 keV_{nr} (the quenching factor for nuclear recoils at these energies is approximately 25%), we expect about 300 CENNS events to be detected per year at the BNB (nominally 10^{21} POT). Our estimates indicate that the backgrounds should be controllable to a few per cent, and with adequate shielding, the beam-induced neutrons can be adequately attenuated. Our calculations from the previous neutron measurements show that about 7 m of concrete is sufficient to discover CENNS with negligible neutron contamination.

A first measurement of CENNS therefore requires a new LAr detector and a new neutron shielding system. Currently, the MiniCLEAN detector is operating underground searching for dark matter, but it may become available in a few years after its initial dark matter search concludes. This detector satisfies most of our operating requirements, though is only 500 kg. We are exploring options to bring it to Fermilab once a neutron shielding structure is designed. The neutron shielding design will require more input measurements of the neutron flux.

Future neutron measurements

In summer 2014, an effort started to improve neutron measurements at the BNB. The goal of these measurements is to deliver a comprehensive set of neutron measurements at viable locations for a future CENNS experiment (see Figure 4(a)). Because our previous measurements in 2012 were performed with no additional neutron shielding, our proposed measurements seek to modulate the measured neutron spectrum by systematically reconfiguring the surrounding concrete shielding structures. Therefore, we can precisely test our neutron shielding Monte Carlo simulations through a few metres of concrete. With these tests, we will deliver the neutron energy spectrum and flux, direction spectrum, and modulated shielding parameters.

Improved EJ-301 detector array

Three additional EJ-301 neutron detectors were procured from Eljen and have been combined into a single 5-kg detector array. The four-detector configuration is shown in Figure 4(b). These detectors and their data acquisition system are extremely portable, and we will measure the neutron fluxes at a variety of locations around the BNB target building. Until September 2014, the BNB is in an off-target configuration to support a low-mass dark matter search with the MiniBooNE detector [9-10]. This presents a unique opportunity to compare, contrast, and understand the specific processes that govern neutron transport through the BNB radiation shielding with the beam on- and off-target.

The neutron energy sensitivity of an EJ-301 neutron detector was found to be 0.3-1.6 MeV in the previous measurement. A series of precise calibrations were performed in spring 2014 at Indiana University to understand the full energy sensitivity range. We are extending the neutron reconstruction energy range through the full fission-energy-range (approximately 0.5-10 MeV). If the energy range of SciBath does not change, then in tandem, these detectors will be sensitive to 0.5-200 MeV neutrons. These represent the most dangerous neutron energies for a first CENNS experiment in LAr.

Results

Using a Monte Carlo simulation, the incident neutron flux was unfolded from the light output spectra in Figure 3(a). Because SciBath has no ability to discriminate gamma rays from neutrons below 5 MeV, a conservative threshold was placed on the light output to remove most gamma rays. This cut leads to a 10 MeV neutron threshold. At higher energies, the low statistics and finite size of SciBath effectively limit its neutron sensitivity to approximately 200 MeV. Above 10 MeV, 6.3±0.7 neutrons were measured per m^2 per BNB pulse (4.5×10^{12} POT per pulse). Figure 3(b) reports the reconstructed direction spectrum for the highest energy proton recoils. Additional track-like cuts are applied with our topology algorithms. The peak of the direction spectrum is in line with the beam direction but points upstream of the BNB beam target.

Figure 3. (a) The unfolded neutron energy spectrum, (b) the direction spectrum of high-energy recoiling protons

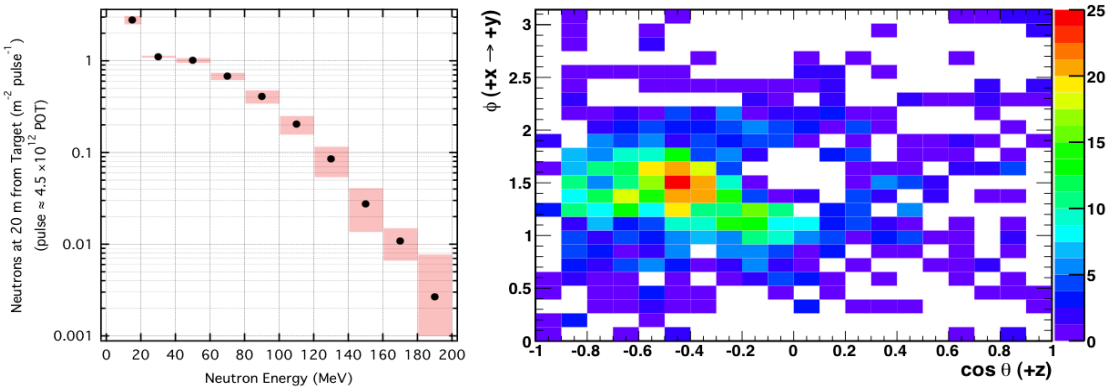

They tend to back-project upstream of the BNB target.

Proposed CENNS experiment at the BNB

Liquid argon (LAr) has several advantages as a detector medium. It has a high light yield, is transparent to its own scintillation light, can be purified, and is relatively inexpensive. This scintillation light has a wavelength of 128 nm, and it comes from the de-excitation of dimers in the form of trapped exciton states. These states can form in a singlet or triplet state and they have very different lifetimes in LAr, 6 ns and 1600 ns, respectively. LAr is also advantageous because the relative amount of the singlet and triplet states produced in an ionising radiation event will depend upon the recoiling particle. Electron recoils from gamma rays will have relatively more triplet state than nuclear recoils from CENNS neutrinos and neutron backgrounds. Therefore, electron recoils will tend to have slower pulses than nuclear recoils. Pulse-shape discrimination (PSD) is then able to separate electron recoils from the desired nuclear recoil signal from CENNS.

For a first CENNS measurement, we are proposing to use a 1-tonne fiducial volume, single-phase, LAr scintillation detector. The single-phase scintillation approach has the advantage of simplicity. The only signal-collecting element is an array of PMTs surrounding the LAr tank. Therefore, signal collection time is only limited by the time-scale of the triplet state. This is in marked contrast to dual-phase systems or time-projection chambers, which collect the ionised electrons over many milliseconds. Fast timing in the single phase allows us to take advantage of the 5×10^{-5} beam duty factor to reject cosmogenic backgrounds, radon progeny, and ^{39}Ar beta decays. ^{39}Ar is naturally occurring and leads to a natural radioactivity of about 1 Bq/kg of LAr. Because of LAr PSD rejection and the beam duty factor, this natural radioactivity should not be problematic.

SciBath detector

The Indiana University-built SciBath detector is a particle-tracking detector using 70 kg of mineral oil-based liquid scintillator (15% by volume pseudocumene and 1.5 g/L PPO). The liquid scintillator is contained in a roughly cubic volume (0.5 m × 0.5 m × 0.5 m) that is read out by 768 wavelength-shifting (WLS) fibers. Each of the three cubic axes is readout by a 16×16 square array of fibers with 2.54 cm spacing. The scintillator does not contain a secondary wavelength shifter (e.g. *bis*-MSB or POPOP) because the SciBath principle requires a wavelength shift to occur inside the WLS fiber. In this way, a fraction of the re-emitted, wavelength-shifted light is optically trapped in the fiber and transported to a PMT. Twelve 64-anode PMTs were used to read out each individual WLS fiber. A schematic drawing of SciBath is shown in Figure 1(b).

The SciBath detector electronics and single photoelectrons were calibrated with an LED pulser system. A stable, low-light LED was pulsed at the opposite end of the WLS fiber from the PMT readout during monthly calibration runs. The energy-to-light yield conversion factor was calibrated with minimum-ionising cosmic ray muons. These muons deposited approximately 65 MeV of energy and yielded about 400 total photoelectrons; the energy-to-light yield conversion factor is about 6 p.e./MeV. Cosmic ray muons were also an excellent calibration of the SciBath tracking capabilities, and we were able to reproduce the angular muon flux at the surface. More importantly, we developed topology algorithms that can separate track-like muons from point-like proton recoils with similar light yields. These were essential for reporting the high-energy neutron direction spectrum.

Figure 2(a) shows the background subtracted light output in 3 μs window around the beam. The discontinuity above 1000 p.e. is due to rebinning for added statistical power. It is clear that the beam duty factor significantly reduces the beam-uncorrelated background rates to negligible levels. Figure 2(b) shows the timing around the beam window for various light output groups. The group with the highest light output (blue) is consistent with fast neutrons in time with the beam interacting with the detector. The middle light output group (red) shows a similar beam turn-on, but there is a noticeable few-μs tail that is consistent with slower neutrons taking longer transit times and longer path lengths from scattering in the target building shielding. Finally, the lowest light output group (black) has a similar turn on and few-μs tail, but its post-beam rate is significantly higher than its pre-beam rate. Extending the time scale shows a characteristic lifetime of ~200 μs, which is consistent with neutrons thermalising in SciBath and our tagging on the 2.2 MeV gamma ray from the $n(p, d)\gamma$ neutron-capture reaction. Unfortunately, total event rates at the surface are too high to use this capture-gating technique to uniquely tag neutrons.

Figure 2. (a) The background-subtracted photoelectron spectrum collected in the beam time window, (b) the timing spectrum around the beam time spectrum for various groups of total photoelectrons

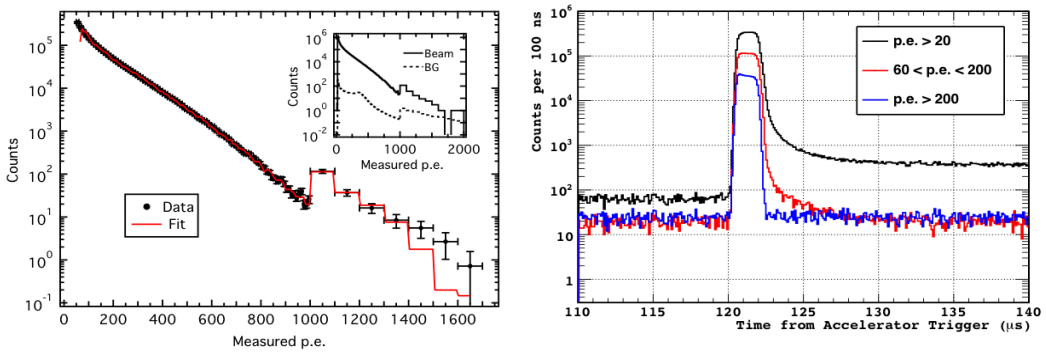

these detectors in the BNB target building. SciBath was located at position A and the EJ-301 was run for a significant amount of time after its survey at position B.

Figure 1. (a) BNB target building: SciBath operated in position A and the EJ-301 collected data at position B, (b) a schematic diagram of the SciBath detector

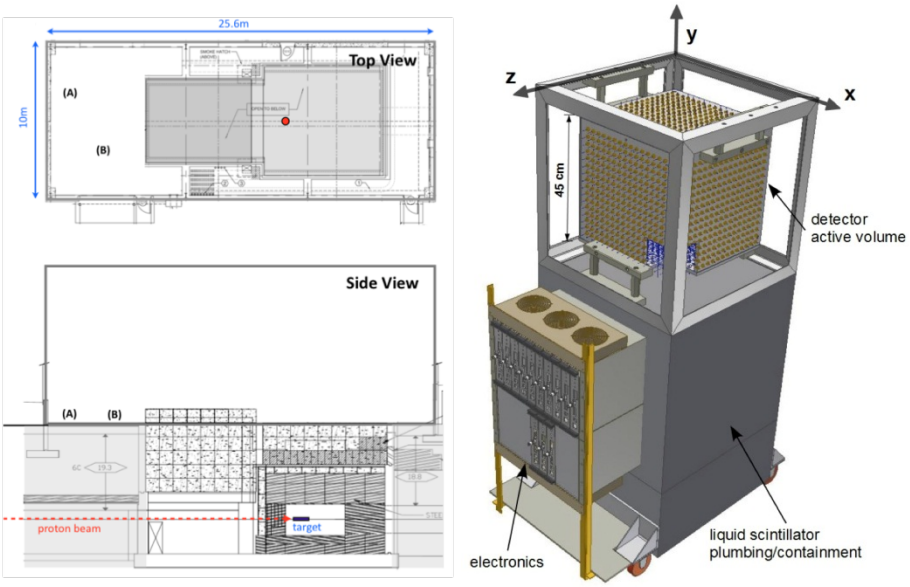

EJ-301 liquid scintillator detector

In order to obtain a rough estimate of the neutron fluxes at various locations in the BNB target building, a small, encapsulated, 1-kg neutron detector was deployed. This detector assembly uses 1-kg of Eljen EJ-301 liquid scintillator and is read out by a single, 5-inch PMT. PMT pulses collected around the BNB beam window were digitised and analysed off-line. The electron-recoil energy scale was calibrated with a variety of gamma ray sources. Manufacturer tabulations of the proton-recoil quenching factors for EJ-301 were used to understand the low-energy neutron scatters on hydrogen. For 1 MeV proton recoils, the quenching factor is ~0.16 compared to a 1 MeV electron recoil from a gamma ray.

EJ-301 can discriminate proton recoils from electron recoils using the pulse shape discrimination (PSD). We used the F90 PSD parameter to discriminate proton and electron recoils. The F90 PSD parameter is the fraction of the photons collected in the first 90 ns of a pulse to the total number of photons collected out to 1 μs. Using a ^{252}Cf source, we found that proton recoils have an F90 that is approximately 0.76-0.91, while electron recoils from gamma ray sources have “faster” pulses with an F90 that is above 0.91. Because of low light levels and digitizer saturation, the effective proton recoil energy range we used was 0.3-1.6 MeV.

The 1-kg detector was moved to various locations in the building in order to scope out an ideal location for the larger SciBath detector (see below). Once a site was located for SciBath, the EJ-301 detector was placed 19 m behind the beam target. Without a precise Monte Carlo simulation of the detector response to neutrons, we roughly estimate that the neutron flux above 0.3 MeV is about 2 neutrons per beam pulse. During our measurements, each BNB beam pulse delivers about 4.5×10^{12} protons on the beryllium target.

magnetic moment. An anomalously large magnetic moment (order 10-10 Bohr magnetons) would be measureable in future CENNS experiments by precisely measuring the nuclear recoil spectrum. CENNS is also sensitive to possible non-standard interactions, which could show up as different interaction strength with a particular neutrino flavour when all flavours should be equal. Low-energy neutrino interactions give supernova their positive pressure, and CENNS is a vital contribution. A programme to measure the CENNS interactions on a variety of nuclear targets can help to understand supernova dynamics. A CENNS detector, like dark matter detectors, can also be used as a sensitive supernova observatory. In fact, the sensitivity to CENNS interactions means that CENNS from solar and atmospheric neutrinos is an irreducible background for 10-tonne-scale dark matter detectors. CENNS can also be used probe nuclear form factors because the finite distribution of nucleons alters the coherence condition slightly. Finally, nuclear reactors are a copious source of low-energy neutrinos. A CENNS detector with very low thresholds could be used to monitor reactors at a distance for non-proliferation applications.

Low-energy neutrino source at the booster neutrino beamline at Fermilab

Fermilab currently operates a pair of GeV-scale neutrino beamlines for a suite of neutrino experiments. These GeV-energy beams are too high energy on-axis to satisfy the CENNS coherence condition. Beam Monte Carlo simulations for the less energetic Booster Neutrino Beamline (BNB) have shown that moving far off-axis (> 45°) leads to a nearly isotropic flux of < 50 MeV neutrinos from stopped pions [4].

The BNB delivers a 32 kW, 8 GeV proton beam to a beryllium target. This, in turn, produces positive pions that decay with a 26 ns lifetime to a positive muon and a muon neutrino. The muon neutrinos are prompt with respect to the 1.6 μs beam and are monoenergetic at 29.9 MeV. The resulting muons then decay with a 2.2 μs lifetime into a positron, muon antineutrino, and an electron neutrino. These neutrinos have a continuous, three-body energy spectrum from 0 MeV to half the muon mass (approximately 50 MeV). Because the beam is 8 GeV, a small fraction of neutrinos are from heavier kaon decays or from muon capture in the surrounding materials. Simulations have shown that the level of contamination from these high-energy neutrinos is tolerable in a CENNS measurement.

To satisfy Fermilab radiation safety regulations, the BNB beam target is surrounded by many tonnes of steel and concrete. The target itself is located about 7 m underground and there is 40 tonnes of steel above and below the target. Around the target are 1600 tonnes of iron blocks and 300 tonnes of concrete shielding above this iron structure. Approximately 30 forward-peaked neutrons are produced per proton on target (approximately 10^{21} POT per year), and simple neutron dosimetric attenuation factors predict that about 3.6×10^{8} neutrons per m^2 per 10^{21} POT emerge 20 m from the target. These estimates predict that 90% of these neutrons have energies below 50 MeV with a tail extending up to 8 GeV. Linearly scaling this attenuation suggests that an additional 8 m of concrete is sufficient neutron shielding for a future CENNS experiment. It is well known that neutron shielding simulation is notoriously difficult, and a programme was started to measure the neutron flux, energy spectrum and direction spectrum in the BNB target building.

Previous neutron measurements

In spring 2012, a pair of neutron detectors were deployed in the BNB target building to measure the fast neutron fluxes correlated with the beam [4]. A portable EJ-301 [5] liquid scintillator detector was first used to survey the fission-energy neutron fluxes in multiple areas around the building. This detector facilitated finding the best location of the larger, 70-kg neutron detector called SciBath [6-7]. Figure 1(a) shows the running location of

in the nucleus are all in-phase and add up coherently. The de Broglie relation can be used to estimate the neutrino energy required to satisfy the coherence condition. The coherence condition requires an incoming neutrino wavelength that is comparable to or larger than the size of a target nucleus. For a typical, medium-A nucleus (nuclear radius $R_N \approx$ few fm), the neutrino energy $\boldsymbol{E_\nu}$ that satisfies the coherence condition is:

$$\boldsymbol{E_\nu < hc/R_N \approx 50}\ \text{MeV} \qquad (1)$$

where h is Planck's constant and c is the speed of light. The experimental signature for a CENNS interaction is the elastic scattering of the target nucleus within the bulk of the target material. It is a simple kinematics problem to calculate the maximum energy imparted to the recoiling nucleus E_r^{max}, and it is:

$$\boldsymbol{E_r^{max} \approx 2E_\nu^2/M \approx 50}\ \text{keV} \qquad (2)$$

where M is the mass of the target nucleus. The direct detection of CENNS has been hampered largely by the development of large-scale, low-background detectors that are capable of low-threshold detection. However, recent progress in direct detection dark matter experiments has made it possible to attempt a first CENNS measurement.

In this paper, we will subsequently describe the physics motivation for measuring CENNS and the unique method we are developing in order to measure it at Fermilab. A CENNS measurement is tantamount to developing a low-energy neutrino source, a large low-energy neutrino detector, and a background rejection scheme. The most troublesome backgrounds are beam-correlated fast neutrons whose elastic scatters resemble the CENNS signal. We will describe the Fermilab Booster Neutrino Beam (BNB) as a viable, low-energy neutrino source. As previously noted, fast neutrons near the BNB are an indistinguishable background, and we will briefly describe our 2012 measurement of these fast neutrons in the BNB target building. This measurement featured an innovative fast neutron detector called SciBath, which is sensitive to up to 10-200 MeV neutrons. Finally, we will conclude with a description of additional measurements that are planned to further characterise the neutron fluxes around the BNB target building.

Physics motivation

The recent Snowmass process has identified CENNS as a fundamentally important interaction for particle physics, direct dark matter searches, astrophysics and supernovae, and as a novel technique for monitoring nuclear reactors [2]. Moreover, the recent P5 report strongly supports the "small neutrino experiment portfolio" in all budget scenarios [3]. Below, we outline some important physics motivations and refer the reader to [4] and the references therein for a more detailed examination of these physics motivations.

The neutral weak current via the Z boson mediates CENNS in the standard model. The standard model cross-section for CENNS interactions is:

$$\boldsymbol{\sigma_{\nu A} = {}^{4}/_{\pi}\, E_\nu^2 \left(Zw_p + Nw_n\right)^2 \approx {}^{G_F}/_{\pi}\, E_\nu^2 N^2} \qquad (3)$$

where wn, wp are the neutral current weak charges for the protons (Z) and the neutrons (N), and GF is the Fermi constant of weak interactions. We see that the cross-section is the coherent addition of all the nucleons, and that because wp ≈ 0, the CENNS interaction rate scales roughly as the number neutrons squared. Of course, bigger nuclei with more neutrons have a larger interaction rate, but its average recoil energy necessarily drops. For medium-A nuclei, the cross-section is approximately 10-39 cm^2, which dominates all other interactions at low energies for a given nucleus.

CENNS is also independent of the neutrino flavour. This is relevant for neutrino disappearance measurements to study short baseline neutrino oscillations and constrain possible sterile flavours of neutrinos. Because neutrinos have mass, they can possess a

Fast neutron measurements at the Booster Neutrino Beamline for a future Coherent Neutrino-Nucleus Scattering (CENNS) Experiment at Fermilab

S.J. Brice, R.L. Cooper[1], F. DeJongh[1], A. Empl[3], L.M. Garrison[2], A. Hime[4], E. Hungerford[3], T. Kobilarcik[1], B. Loer[1], G. Mariani[5], M. Mocko[4], G. Muhrer[4], R. Pattie[6], Z. Pavlovic[4], E. Ramberg[1], K. Scholberg[7], R. Tayloe[2], R.T. Thornton[2], J. Yoo[1], A. Young[6]

[1]Fermi National Accelerator Laboratory, Batavia, US
[2]Indiana University, Bloomington, IN, US
[3]University of Houston, Houston, US
[4]Los Alamos National Laboratory, Los Alamos, NM, US
[5]Virginia Tech, Blacksburg, VA, US
[6]North Carolina State University, NC, US
[7]Duke University, Durham, NC, US

Abstract

Low-energy neutrinos (E<50 MeV) have a standard model predicted, but unobserved, coherent elastic neutrino-nucleus scattering (CENNS) mode. Coherent neutrino scattering has important physics reach for understanding supernovae dynamics, direct supernova neutrino detection, standard model tests, nuclear form factors, direct dark matter search backgrounds, and reactor monitoring. The CENNS collaboration proposes to deploy a 1-tonne fiducial volume, single-phase, liquid argon scintillation detector at a far off-axis location at the Fermilab Booster Neutrino Beam (BNB) in order to produce a flux of low-energy neutrinos from decay-at-rest pions. The CENNS detector must be placed relatively close to the BNB target (approximately 20 m) in order to maximise the detected neutrino flux. Because the detector is relatively close to the BNB target, a major concern is the beam-correlated fast neutron fluxes that give the same signal as a coherently scattering neutrino. In order to understand these fluxes, the Indiana-built SciBath detector was deployed to measure fast neutron fluxes 20 m from the BNB target in the BNB target building. The SciBath detector is a novel 80-liter liquid scintillator, particle tracking detector that is read out by a three-dimensional grid of 768 wavelength-shifting fibers. The fiber readout allows SciBath to measure neutral particle fluxes by tracking the recoiling charged particles with uniform efficiency in all directions. This paper will describe the SciBath detector and summarise our previous measurement of the flux of 10 to 200 MeV neutrons at the BNB. This paper will also highlight a plan to improve these neutron measurements at the BNB with the SciBath detector and other neutron detectors. We will systematically change a concrete shielding structure around the detectors to modulate the neutron background fluxes. In this way, we will validate a shielding Monte Carlo simulation of the neutron flux.

Introduction

Coherent Elastic Neutrino-Nucleus Scattering (CENNS) has never been observed despite its standard model prediction by Freedman in 1974 [1]. In order to satisfy the coherence condition for CENNS, the neutrinos must have sufficiently low energy such that very little momentum is transferred in a collision. In this way, the scattered waves off each nucleon

[10] T. Guo et al. (2001), "Generation of hard x rays by ultrafast terawatt lasers", *Rev. Sc. Instr.*, 72, pp. 41-47.

[11] L.M. Chen et al. (2004), "Study of hard x-ray emission from intense femtosecond Ti:sapphire laser-solid target interactions", *Phys. Plasmas*, 11, pp. 4439-4445.

[12] R. Qiu et al. (2010), "Preliminary Radiation Hazard Analysis of X-ray Generated by High Intensity Laser Systems", SLAC RP Note RP-10-11.

[13] R. Qiu et al. (2011), "Analysis and mitigation of X-ray hazard generated from high intensity laser-target interaction", SLAC-PUB-14351.

[14] J. Bauer et al. (2011), "High intensity laser induced radiation measurements at LLNL", SLAC RP Note RP-11-11.

[15] M. Woods (2010), "Laser Beam Focusing and Propagation", SLAC LSO Memo 2010-10.

[16] J. Bauer et al. (2013), "Measurements of Ionizing Radiation Doses Induced by High Irradiance Laser on Targets in LCLS MEC Instrument", SLAC PUB-15889.

[17] D.D. Meyerhofer et al. (1993), "Resonance absorption in high-intensity contrast, picosecond laser-plasma interactions", *Phys. Fluids B*, 5, pp. 2584-2588.

[18] H. Chen et al. (2009), "Hot Electron Energy Distributions from Ultraintense Laser Solid Interactions", *Phys. Plasmas*, 16, 020705.

[19] P. Mulser, D. Bauer (2010), *High Power Laser-Matter Interaction*, Springer, Berlin Heidelberg, 416 p.

[20] F. Borne et al. (2002), "Radiation protection for an ultra-high intensity laser", *Radiat. Prot. Dosim.*, 102, pp. 61-70.

[21] K.W.D. Ledingham et al. (2000), "Photonuclear Physics when a Multiterawatt Laser Pulse Interacts with Solid Targets", *Phys. Rev. Lett.*, 84, pp. 899-902.

[22] M. D. Perry et al. (1997), "Laser Driven Radiography", Lawrence Livermore National Laboratory UCRL-ID-129314.

[23] Y. Hayashi et al. (2006), "Estimation of photon dose generated by a short pulse high power laser", *Radiat. Prot. Dosim.*, 121, pp. 99-107.

[24] M.H. Key et al. (1998), "Hot electron production and heating by hot electrons in fast ignitor research", *Phys. Plasmas*, 5, 1966-1972.

[25] Y. Ping et al. (2008), "Absorption of Short Laser Pulses on Solid Targets in the Ultrarelativistic Regime", *Phys. Rev. Lett.*, 100, 085004.

[26] G. Battistoni, S. Muraro, P.R. Sala, F. Cerutti, A. Ferrari, S. Roesler, A. Fassò, J. Ranft (2007), "The FLUKA code: Description and benchmarking", *Proceedings of the Hadronic Shower Simulation Workshop 2006*, Fermilab 6-8 September 2006, M. Albrow, R. Raja eds., AIP Conference Proceeding 896, 31-49.

[27] A. Ferrari, P.R. Sala, A. Fassò, and J. Ranft (2005), "FLUKA: a multi-particle transport code", CERN-2005-10, INFN/TC_05/11, SLAC-R-773.

[28] V. Vlachoudis (2009), "FLAIR: A Powerful But User Friendly Graphical Interface For FLUKA" *Proc. Int. Conf. on Mathematics, Computational Methods and Reactor Physics* (M&C 2009), Saratoga Springs, New York.

Active and passive instruments measured photon dose yields of about 10-4 mSv/J outside the MEC target chamber. As seen in Figure 11, these experimental results agree well with the 1-D ambient dose equivalent projection calculated in FLUKA simulations.

Summary

As part of an on-going study, recent experiments at SLAC MEC focused a high-intensity laser (1.8×10^{18} W/cm^2, T_h=183 keV, 0.2 J at 1 Hz) onto 100 µm thick copper targets. Active and passive detectors measured the ionising radiation generated inside and outside the target chamber. Preliminary results show photon and neutron dose yields of around 10^{-4} and 5×10^{-8} mSv/J, respectively, outside the MEC target chamber. Inside the chamber, passive dosimeters measured very high integrated doses, primarily due to low-energy electrons, up to 650 cGy after 540 laser shots. Analysis of the complex electron source term and mixed electron/photon dose results inside the chamber are on-going, and particle-in-cell plasma code studies are planned to better characterise the energy and angular distribution of the electron source term generated from the laser plasma.

Analytical models appear to provide a good estimate of the photon dose yield outside the target chamber generated from laser-matter interactions. Measurements of photon H*(10) outside the MEC target chamber also agree with results of FLUKA simulations. Future plans are underway at SLAC to further upgrade the MEC laser to a pulse energy of 8 J, and dedicated radiation measurements at higher laser intensities up to 2×10^{20} W/cm^2 (T_h=3.5 MeV) with different targets (including gas acceleration) will be performed.

Acknowledgements

This work was supported by Department of Energy contract DE-AC02-76-SFO0515. The authors wish to acknowledge support from William White (SLAC), Philip Heimann (SLAC), and Thomas Cowan (HZDR).

References

[1] J. Hastings et al. “Physics Requirements for MEC Instrument”, LCLS RPD SP-391-001-89 R0.

[2] W. P. Leemans et al. (2006), “GeV electron beams from a centimetre-scale accelerator”, *Nat. Phys.*, 2, pp. 696-699.

[3] T. Tajima, J. M. Dawson (1979), “Laser Electron Accelerator”, *Phys. Rev. Lett.*, 43, pp. 267-270.

[4] G. Malka, J.L. Miquel (1996), “Experimental Confirmation of Ponderomotive-Force Electrons Produced by an Ultrarelativistic Laser Pulse on a Solid target”, *Phys. Rev. Lett.*, pp. 75-78.

[5] F. Brunel (1987), “Not-So-Resonant, Resonant Absorption”, *Phys. Rev. Lett.*, 59, pp. 52-55.

[6] S.C. Wilks et al. (1992), “Absorption of Ultra-Intense Laser Pulses”, *Phys. Rev. Lett.*, 69, pp. 1383-1386.

[7] S.C. Wilks, W.L. Kruer (1997), “Absorption of Ultrashort, Ultra-Intense Laser Light by Solids and Overdense Plasmas”, *IEEE J. Quantum Electron.*, 33, pp. 1954-1968.

[8] F. Amiranoff et al. (1998), “Observation of Laser Wakefield Acceleration of Electrons”, *Phys. Rev. Lett.*, 81, pp. 995-998.

[9] M.I.K. Santala et al. (2000), “Effect of the Plasma Density Scale Length on the Direction of Fast Electrons in Relativicstic Laser-Solid Interactions”, *Phys. Rev. Lett.*, 84, pp. 1459-1462.

Whereas when bremsstrahlung is suppressed only in the target, the dose is seen all around the outside of the target chamber and agrees well with photon yield measured by the active instruments. This is especially noticeable in the backward (-x axis) direction outside the chamber where the dose is about 10^{-4} mSv/J.

Figure 11 shows the 1-D dose yield projection for electrons and photons when simulating either a mono-directional or isotropic electron beam scenario in FLUKA with energy thresholds of 1 keV for both electrons and photons. The 1-D slice is in the backward direction, extending radially from the laser-target interaction point at R=0 cm. As before, the target is a 100 μm thick copper foil. Also, the FLUKA calculation did not implement any local steel shielding inside the target chamber because measurement locations of interest were unshielded during the actual experiment.

Figure 11. Comparison of 1-D FLUKA H*(10) projection with measured photon dose ($I=1.8x10^{18}$ W/cm^2, T_h=183 keV)

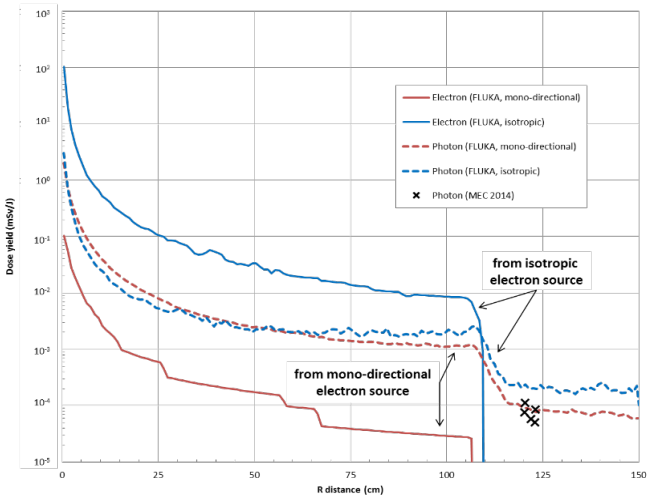

When observing a 1-D slice in the backward direction, the electron and photon dose yields differ between the isotropic or mono-directional electron beam scenarios. For an isotropic electron beam in FLUKA, the electron dose contribution dominates over the photon. However, this relation is reversed for a mono-directional source where the photon dose is greater. This behaviour is expected due to the fact that source electrons are emitted in all directions, including backwards, for the isotropic case, and only in the forward direction for the mono-directional case. Thus, the electron dose seen in Figure 11 for the mono-directional case is primarily due to back-scattered electrons from interactions with the copper target, whereas both source electrons and scattered electrons contribute to the electron dose in the backward direction for an isotropic electron beam scenario.

On the other hand, bremsstrahlung photons from electrons interacting with the copper target or aluminium chamber is the dominant mechanism that contributes to the photon dose yield for both electron beam direction scenarios, but a few interesting observations can be made from their slight differences in Figure 11. Inside the chamber at about R<50 cm, the photon yield from a mono-directional source is greater than the yield from an isotropic source because all the mono-directional source electrons in FLUKA can experience bremsstrahlung with the copper target. Near the Al chamber wall (R=100 cm), the photon yield is greater for the isotropic case due to source electrons now interacting with the Al chamber wall and producing bremsstrahlung photons. Photon build-up in the chamber wall can even be observed for the isotropic case at about R=105 cm. The photon dose outside the MEC chamber (R>110 cm) is also greater for the isotropic case.

Figure 9. 1-D ambient dose equivalent H*(10) projection

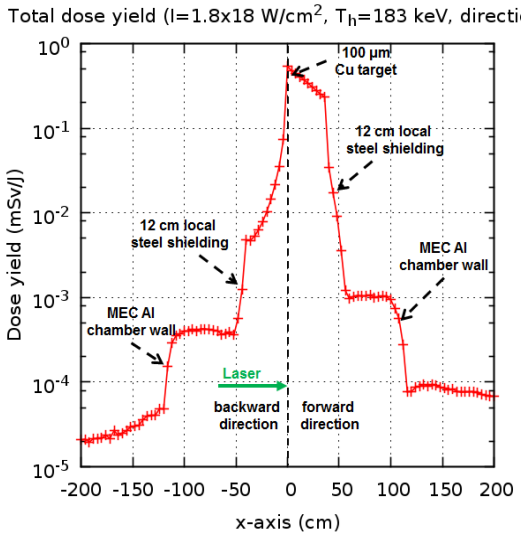

Source of dose outside target chamber

Simulations in FLUKA are used to gain additional insight on where the photon dose measured outside the MEC target chamber during the experiment originates from. Figure 10 presents results from two separate FLUKA simulations where bremsstrahlung photon production was suppressed in either the Al chamber wall or the Cu target using a high-energy (1 GeV) threshold for photon production. In Figure 10, the dose map on the left shows the total ambient dose equivalent for the target chamber when there is no bremsstrahlung photon production in the Al walls. The dose map on the right shows the ambient dose equivalent when there is no bremsstrahlung production in the Cu target. For both scenarios, the ambient dose equivalent inside the target chamber remains relatively unchanged because of dominance of electrons.

Figure 10. Suppression of bremsstrahlung photon production in FLUKA ($I=1.8\times10^{18}$ W/cm^2, T_h=183 keV, isotropic)

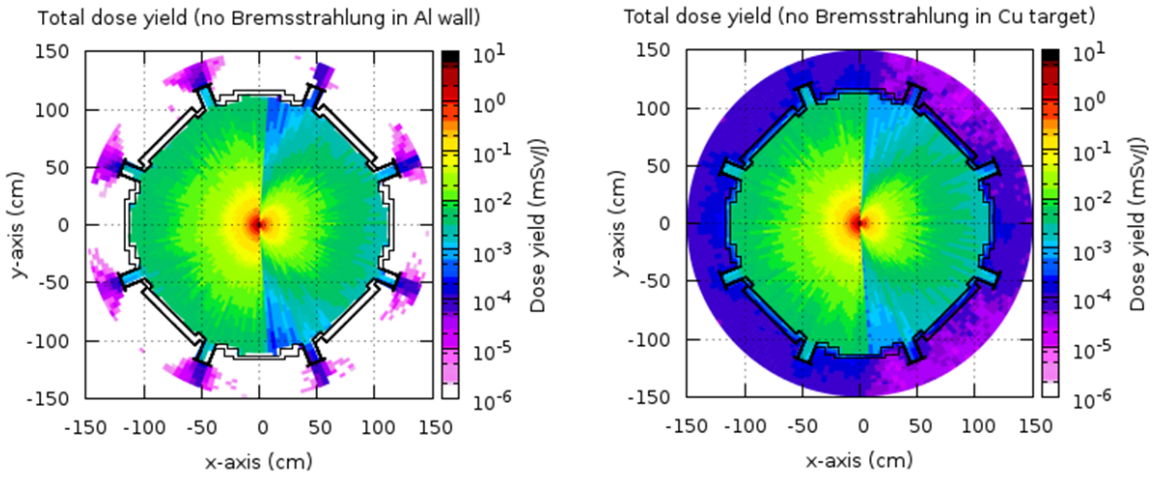

The comparison in Figure 10 appears to indicate that the dose outside the MEC target chamber is dominated by bremsstrahlung photons from electron interactions with the Al chamber wall for $I=1.8\times10^{18}$ W/cm^2. When photon production is suppressed in the Al walls, only a slight amount of dose escapes the chamber via the thin glass viewports.

Figure 8. Neutron dose results from BF_3 detectors

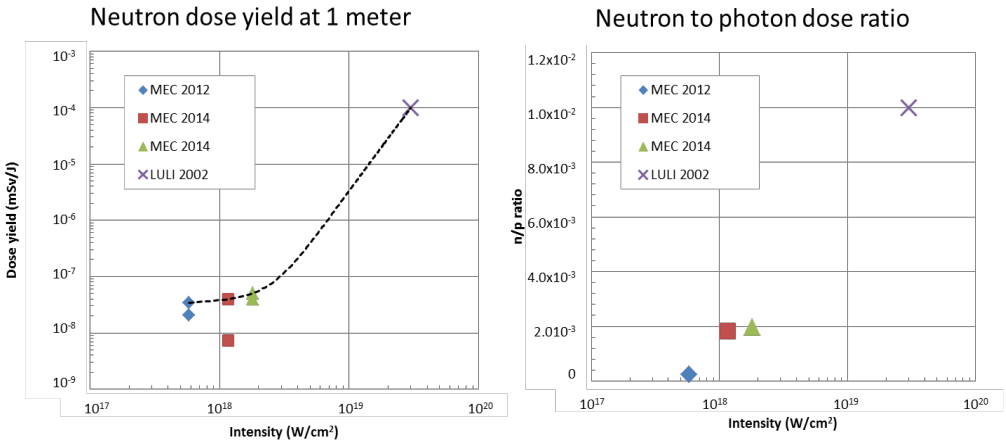

FLUKA simulations

Monte Carlo simulations with the radiation transport code FLUKA were used to calculate the bremsstrahlung photon yield outside the MEC target chamber from hot electron interactions inside the chamber and to compare with experimental measurement results. FLUKA2011 Version 2b.5 was used for all simulations [26-28]. The energy thresholds for electron and photon production and transport in FLUKA were both set at 1 keV.

Electron source term

The information on angular distribution of the electrons source term is limited. Thus, two opposite scenarios for the electron angular distribution were considered in the FLUKA simulations: mono-directional and isotropic.

For the mono-directional case, the electron source is modelled as a pencil beam and directed along the path of the laser. The electron beam (with energy sampled from a distribution characterised by Equation 4 and T_h from Equation 2) interacts with the laser target (100 µm thick copper foil). Figure 9 shows the FLUKA-calculated one-dimensional ambient dose equivalent $H^*(10)$ yield projected along the direction of the mono-directional electron beam (+x axis). The asymmetrical 1-D dose profile is a result of the simulated directional electron pencil beam interacting with the copper target at x=0 cm. The 12 cm local steel shields at x=±40 cm effectively reduce the ambient dose (mixed electron and photon field) by at least two orders of magnitude, and the Al walls of the chamber itself serve to further reduce the dose (dominated by photons) that may escape the target chamber.

For the isotropic beam case, the electrons are again sampled from an energy distribution characterised by Equation 4, but instead of being modelled as a pencil beam like the mono-directional case, the electrons are emitted isotropically as a point source from the surface of the copper target.

Figure 7. Photon dose yield (mSv/J) at 1 meter

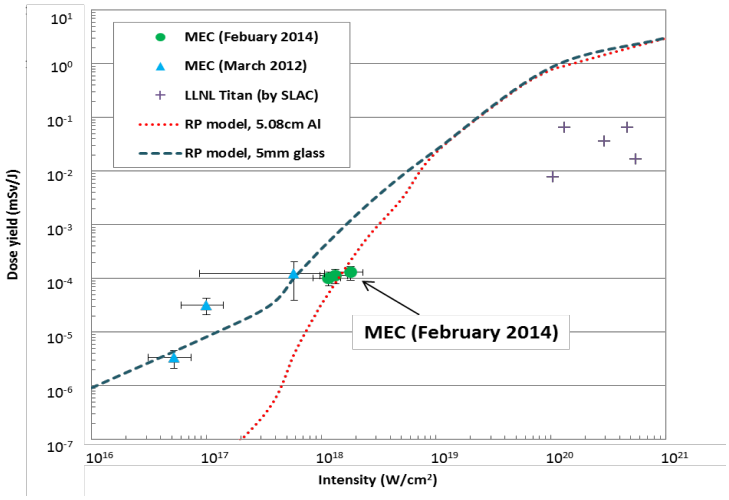

The three green circles are measurements from the February 2014 MEC experiment presented earlier and represent detector locations outside the target chamber wall (5.08 cm Al). The right point at 1.8×10^{18} W/cm^2 is the dose yield generated from the peak laser intensity before OAP mirror damage. The left point at about 1.1×10^{18} W/cm^2 is the final intensity inferred from the drop in dose rate observed in Figure 6. This laser intensity is calculated assuming the energy transmission fraction of the OAP mirror decreases proportionally with the observed decrease in dose rate. The middle point is associated with the integrated dose measurements by passive dosimeters and is a shot-weighted average of the two other laser intensities.

The two lines for the RP model represent the analytical calculation of photon dose as described earlier. The MEC target chamber is primarily Al wall with thin glass viewports. The dashed blue line estimates the photon dose yield through the thin 5 mm glass viewport of the MEC target chamber. Similarly, the dotted red line estimates the photon dose yield transmitted through a 5.08 cm thick Al chamber door. After converting the dose rates and integrated doses measured by active and passive instruments from earlier, the dose yields outside the MEC target chamber are about 10^{-4} mSv/J. This is in agreement with the RP model adjusted for attenuation of 5.08 cm of aluminium wall.

Neutron dose outside target chamber

As seen earlier in Figure 5, the results of the two neutron detectors agreed with each other, measuring a maximum neutron dose rate of 30 nSv/h. The neutron dose rate also translates to a dose yield of about 5×10^{-8} mSv/J at 1 m and a neutron-to-photon yield fraction of about 2×10^{-3} for I=1.8×10^{18} W/cm^2. Figure 8 compares the neutron results from the February 2014 MEC experiment to other experiments where neutrons were also measured [16] [20].

the MEC chamber is directionally dependent and dependent on the dose inside the chamber.

PTW-01 was located inside the Hutch 6 control room above the hutch roof. The control room is 3 m above the MEC target chamber and shielded by about 25 cm of concrete roof. This combination of distance and shielding caused PTW-01 to only measure a maximum dose rate of 0.01 µSv/h above background. PTW-02 was located outside the Hutch 6 steel roll up door about 6 meters from the target chamber and measured a maximum dose rate of 0.1 µSv/h above background.

Figure 6 shows a marked drop in photon dose rates over the course of 540 laser shots at 1 Hz. The same decreasing pattern was also observed by the BF_3 neutron detectors. The left bunch represents 140 shots, and right bunch represents 400 for a total of 540 laser shots on the copper target with a starting peak intensity of 1.8×10^{18} W/cm^2. The drop in dose rates is linked with the progressive damage of the Al-coated OAP focusing mirror. In addition, the sudden dips in the dose rate are due to the target rastering system shifting the copper foil to provide fresh material for laser shots.

Figure 6. Photon dose rates from Victoreen 451 #1

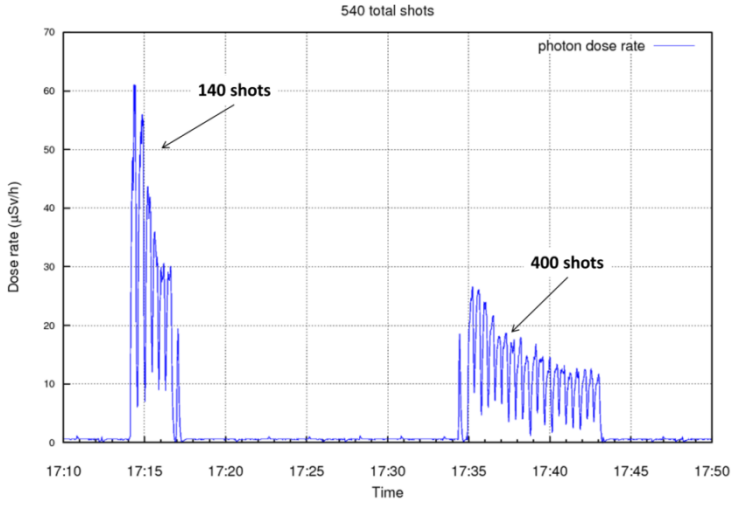

Most passive dosimeters such as the 2 mSv PIC, InLight, and Luxel+ that measure integrated dose were not sensitive enough and did not read above background. Measurements with more sensitive dosimeters (RADOS and 0.02 mSv PIC) did provide dose results that agreed well with each other. The maximum integrated doses measured on the passive dosimeters outside the target chamber were 4 µSv around the sides and 6 µSv above the chamber roof. The passive dosimeters on the roof measured higher doses because the chamber roof is thinner than the sides.

Photon dose yield

Figure 7 presents the maximum measured dose yield from this and two past experiments [14] [16], and error bars represent one standard deviation. Dose yield (ambient dose equivalent generated per laser shot energy) is in units of mSv/J at a distance of 1 meter. The blue triangles are from the 2012 MEC experiment [16], and the purple pluses are the 2011 measurements performed by SLAC RP at the LLNL Titan laser Facility [14]. The Titan results are shown with no error bars, since they were obtained parasitically from another experiment, and thus the laser-optic parameters were not well characterised and subject to large uncertainties.

The maximum measured dose is 650 cGy in the backward direction and 100 cGy in the forward. The angular distribution of dose suggests that the dose is peaked towards 0°, whereas the dose in the backward direction spreads over a wide angle. Two possible factors may contribute to the difference between the measured forward and backward dose: target thickness and laser intensity. Studies at other facilities have shown that the dose is dominantly in the forward direction [25]. However, these studies utilise filters to measure only electrons of 100 keV and greater, or they use a very high laser intensity between 10^{19}-10^{20} W/cm^2. On the other hand, the February 2014 MEC measurements presented here include dose from low-energy electrons along with high energy, and the laser intensity is also comparatively low at 1.8x10^{18} W/cm^2. In addition, the 100 µm thick copper target used in this experiment can be considered a thick target shielding to low-energy electrons in the forward direction. This shows the complexity of energy and angular distributions of hot electrons and their implications on photon doses outside the target chamber.

Radiation levels outside target chamber

Figure 5 shows the maximum photon and neutron dose rates (ambient dose equivalent) measured above background with the active instruments outside the MEC chamber, excluding PTW pressurised ion chambers. Each BF_3 station also included a Victoreen 451 to measure photon dose rate at that location. All active detectors performed well at the laser intensity of 1.8x10^{18} W/cm^2 at 1 Hz and were not affected by any electromagnetic pulse effects as experienced in experiments [14].

Figure 5. Maximum dose rates from active detectors at target chamber (I=1.8x1018 W/cm2 at 1 Hz)

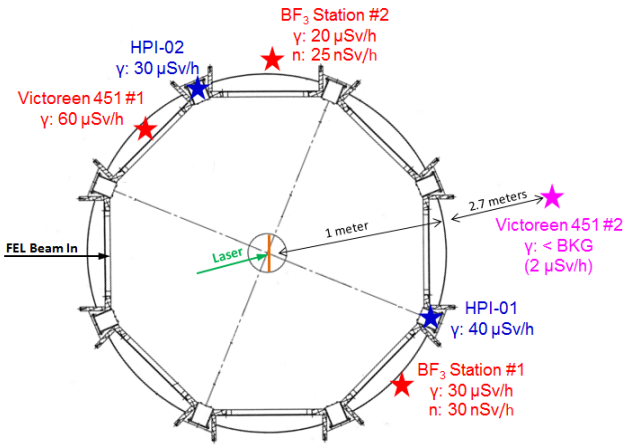

The maximum photon dose rate outside the target chamber of 60 µSv/h was measured by Victoreen #1 in the backward direction of the laser. This location outside the chamber corresponds with the mostly backward-directed nanoDot doses shown earlier in Figure 4. On the other hand, Victoreen #2 was shielded by 12 cm of steel shielding inside the chamber and did not measure greater than background during the experiment. This result demonstrates the effectiveness of localised shielding (designed for up to ~1x10^{20} W/cm^2 and 8 J) inside the target chamber for a laser intensity of 1.8x10^{18} W/cm^2.

As shown in Figure 5, the photon dose rates from active detectors outside the MEC chamber agree well. Differences between the photon dose rates may be due to self-shielding effects of the optics equipment and lenses inside the chamber as seen earlier in Figure 3. Comparing results from active detectors suggests the photon dose rate outside

deployed outside the target chamber to measure the photon doses that escape the target chamber.

The active instruments included RADOS electronic dosimeters, two HPI-6031 styrofoam-walled ion chambers, two PTW-7262 pressurised argon ion chambers, Victoreen-451 handheld ion chambers, and two polyethylene-moderated BF_3 neutron detectors (a quasi-remmeter design). The RADOS were added to the passive dosimeters outside the target chamber at their respective locations. The two HPI ion chambers, HPI-01 and HPI-02, were positioned directly outside the target chamber. One of the PTW ion chambers, PTW-01, was located in the Hutch 6 control room on the roof, the other, PTW-02, was at the Hutch 6 steel roll up door. The Victoreen-451 meters and BF_3 detectors were deployed at various angles and distances around the target chamber. The active instruments provided real-time dose monitoring information throughout the experiment. These detectors are described in detail in [16].

Measurement results

The amount of ionising radiation generated from laser-matter interaction depends heavily on the intensity and energy of laser and less on the solid target material and thickness. For a laser interacting with a solid high Z target, the radiation field inside the target chamber is composed of the accelerated hot electrons and bremsstrahlung photons originating from either the copper target itself or the walls of the Al chamber. The varying 2.54 to 5.08 cm thick Al wall of the target chamber is expected to attenuate the large majority of the low-energy electrons and photons. However, electrons and photons of sufficiently high energy can penetrate the wall, or the chamber's thin 5 mm glass view ports. The following sections provide preliminary measurements results from active and passive detectors used during the MEC experiment.

Dose inside target chamber

Passive nanoDot dosimeters inside the MEC chamber measured very high integrated doses from the experiment. The nanoDot results presented here are based on ^{85}Kr shallow dose calibration that accounts for the high fluence electron field inside the chamber. Figure 4 presents a polar plot of dose from nanoDots located 30 cm radially from the laser-target interaction point.

Figure 4. Dose (cGy) from nanoDots inside MEC chamber at 30 cm (I=1.8x10^{18} W/cm^2 for 540 shots)

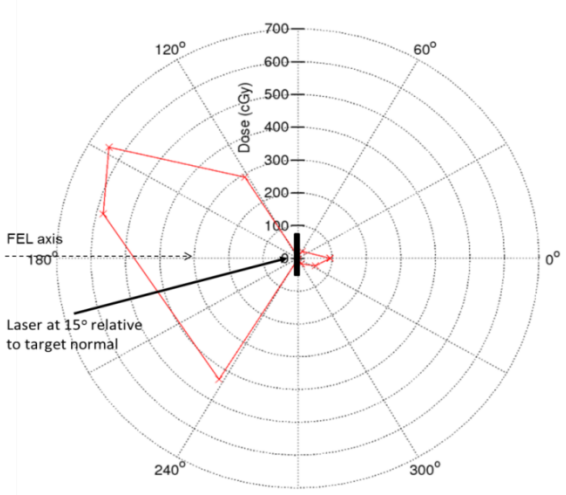

thick steel shields were deployed inside the MEC chamber in the forward and backward direction of the laser beam to evaluate their effectiveness in shielding the generated ionising radiation. Their efficacy is discussed later in the measurement results.

Figure 3. Layout inside MEC chamber for February 2014 experiment

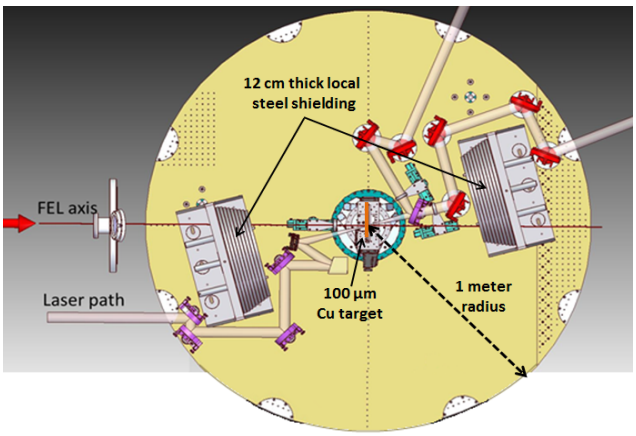

Table 1 lists key laser and optic parameters for the experiment and their associated uncertainties (one standard deviation). A total of 540 laser shots on target were taken during the course of the experiment. Due to the damage to the Al-coated OAP focusing mirror from the high-energy laser beam, only a limited number of shots could be taken. Future experiments using the MEC laser system will utilise other metal mirror coatings with higher reflectivity.

Table 1. Parameters from February 2014 MEC experiment (uncertainties in parentheses)

Parameters	MEC 2014
Target material	Copper
Target thickness (µm)	100
Energy before compressor (mJ)	1400 (5%)
Transmission fraction of compressor	0.68 (2%)
Transmission fraction of Al-coated OAP	0.87 (5%)
Fraction of energy in main peak	0.23 (20%)
Energy on target in main peak (mJ)	192 (21%)
FWHM pulse duration (fs)	70 (5%)
Horizontal $1/e^2$ radius spot size of main peak (µm)	13 (10%)
Vertical $1/e^2$ radius spot size of main peak (µm)	8 (10%)
Calculated peak intensity (W/cm^2)	1.8×10^{18} (27%)

Detectors and instruments

A combination of passive dosimeters and active detectors were deployed inside and outside the Al MEC target chamber and around Hutch 6 for radiation measurements. The passive dosimeters included electrostatic pocket ion chambers (PIC) with a full scale of 0.02 or 2 mSv and Landauer personnel dosimeters (nanoDot, Luxel+ Ja, and InLight). Only nanoDots were approved for use in the MEC under vacuum conditions, and these were expected to record high-dose values from the mixed electron and photon field inside the target chamber. All other dosimeters (0.02 and 2 mSv PICs, Luxel+ Ja, and Inlight) were

and 50% for I > 10^{19} W/cm^2 [1] [24]. Because Hayashi equations only account for the 0° photon dose yield at very high-intensity lasers with no shielding, the SLAC RP model may overestimate the photon dose outside 0° and when accounting for the shielding effects of the target chamber itself.

Experimental set-up and beam parameters

The February 2014 experiment was performed at the LCLS Hutch 6 (MEC hutch) using the 0.8 µm Ti:Sapphire short pulse laser on a 100 µm thick copper target. Figure 2 shows the layout of MEC Hutch 6 with its short and long pulse laser systems and the aluminium target chamber.

Figure 2. Layout of SLAC LCLS Hutch 6

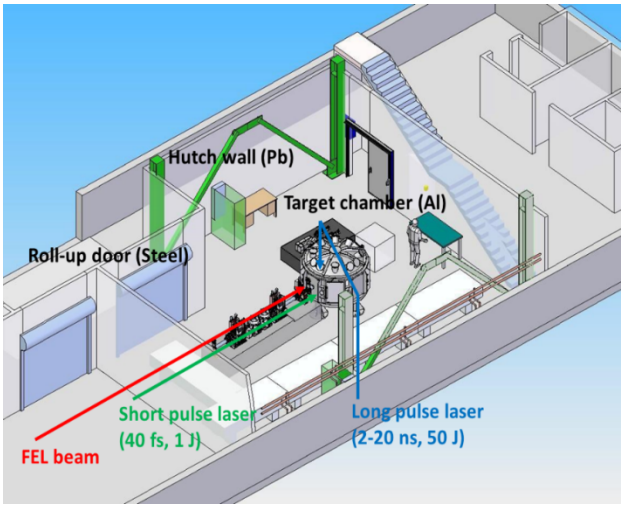

MEC target chamber layout

Figure 3 shows a horizontal cross-section of the MEC target chamber. The target chamber has a radius of about 1 meter, and its aluminium walls vary in thickness, but are typically 2.54 cm thick (5.08 cm for chamber doors). For the 2014 MEC experiment described here, the unfocused short pulse laser entered the target chamber from the left and was directed with a series of mirrors to an Al-coated off-axis parabolic (OAP) mirror. The OAP mirror focused the laser beam to a horizontal and vertical 1/e2 radius spot size of 13 µm × 8 µm with a peak intensity of 1.8x1018 W/cm2 at 192 mJ. The focused laser beam was incident on the target material at an angle of 15o relative to target normal. Copper foils of thickness 100 µm served as the laser targets and were positioned at the chamber centre and perpendicular to the FEL axis.

The lenses and mirrors located downstream of the laser-matter interaction point were used before the start of the experiment for characterising laser beam parameters. Pulse energy measurements were taken with a Coherent J50 50M-IR sensor and a Coherent LabMax-TOP meter. The pulse duration was measured twice with two separate instruments, a Coherent single-shot autocorrelator (SSA) and an APE LX Spider autocorrelator, before and after the experiment, and both instruments reported the same result. An Adimec OPAL-1000 CCD camera, calibrated before the experiment, determined the spot size by imaging the beam. The measured profile of the focused beam on target was a complicated distribution with multiple peaks, and this contributes to the uncertainty associated with laser intensity calculations.

With the laser system operating at 1 Hz, a target rastering system ensured each laser shot interacted with fresh copper material. Furthermore, as seen in Figure 3, two 12 cm

Figure 1. SLAC RP model for T_h (keV) as a function of I (W/cm²) with λ=0.8 µm

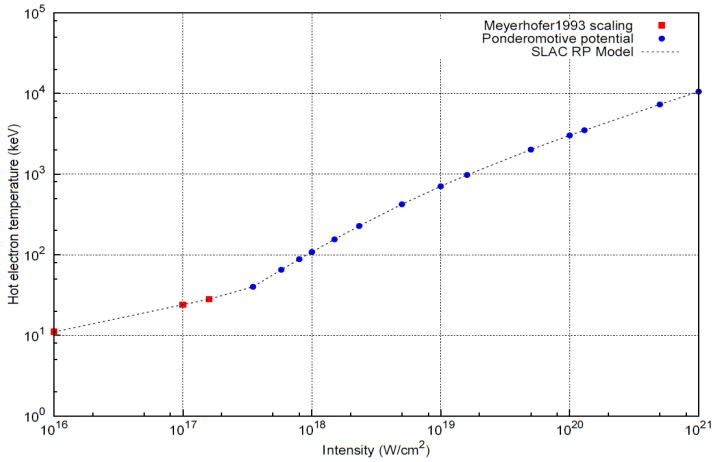

The energy distribution of electrons is also characterised by T_h. Equations (3) and (4) give two distributions used by RP to characterise the energy of the hot electrons for I below and above 10^{18} W/cm², respectively [20-22]. The Relativistic Maxwellian case with an average electron energy of $3T_h$ is a harder electron spectrum than the Maxwellian case with an average energy of $1.5T_h$.

$$N_e \propto E_e^{1/2} \exp\left(-\frac{E_e}{T_h}\right) \text{ for } I \le 10^{18} \text{ W/cm}^2 \text{ (Maxwellian)} \quad (3)$$

$$N_e \propto E_e^{2} \exp\left(-\frac{E_e}{T_h}\right) \text{ for } I > 10^{18} \text{ W/cm}^2 \text{ (Relativistic Maxwellian)} \quad (4)$$

Photon dose calculation

Monte Carlo codes such as FLUKA can predict the photon dose from a hot electron spectrum described by Equation (3) or (4), the hot electron temperature T_h, the laser energy to electron energy conversion efficiency α, and the angular and spatial distribution of the electrons. However, it is desired to have a simple empirical formula based on the above parameters that can provide a quick estimate of the photon dose yield due to laser-matter interaction.

The SLAC RP model for photon dose utilises Equations (5) and (6) from Y. Hayashi [23] that are derived for the maximum bremsstrahlung photon dose (occurring at 0° along laser axis) generated through interaction between a short pulse high-power laser and a solid target. The equations are based on a laser-generated electron spectrum with a Relativistic Maxwellian distribution as described earlier in Equation (4).

$$H_x \approx 1.8 \times \left(1.10 \times \frac{\alpha}{R^2}\right) \times T_h^2 \text{ for } T_h < 3 \text{ MeV} \quad (5)$$

$$H_x \approx 1.8 \times \left(3.32 \times \frac{\alpha}{R^2}\right) \times T_h \text{ for } T_h \ge 3 \text{ MeV} \quad (6)$$

The 0° photon dose yield H_x is in units of Sv/J, and R is the distance between the laser-target interaction point and the dose point in cm. Equations (5) and (6) from Hayashi were derived based only on the ponderomotive force theory for I between 10^{19} to 10^{21} W/cm². To adapt for lower laser intensities, the RP model uses the T_h from Equations (1) and (2) to calculate H_x. The SLAC RP model for the laser conversion efficiency α is 30% for I ≤ 10^{19} W/cm²

methods and tools to estimate the required shielding at various intensities for different targets.

Experiments performed to-date include radiation measurements at the Lawrence Livermore National Laboratory's Titan laser Facility in 2011 and measurements at SLAC's MEC Facility in 2012 and 2014. In the Titan measurements, the laser beam intensity and pulse energy were ~10^{20} W/cm^2 and 400 J, respectively. Targets included 3-5 mm thick hydrocarbon foam and 1 mm gold foil. The 2012 experiment at SLAC's MEC laser facility was performed with laser intensities between 3x10^{16} and 6x10^{17} W/cm^2 (40 fs and up to 0.15 J per pulse). Targets for the MEC 2012 experiment included gold foils (0.01 and 0.1 mm) and copper (1 mm). The results of these two measurements have been reported elsewhere [14] [16]. Preliminary results of the latest MEC experiment in February 2014 are compared with results from analytical models and Monte Carlo simulations.

SLAC RP dose model

The bremsstrahlung photon yield due to hot electrons generated from laser-matter interaction is characterised by the temperature (or energy) of hot electrons, T_h, and the laser energy to electron energy conversion efficiency, α. The hot electron temperature T_h is a function of laser parameters and increases with the normalised laser intensity, $I\lambda^2$, where I (W/cm^2) is the laser intensity, λ the laser wavelength (μm) [17] [18].

Electron temperature and energy distribution

At lower laser intensities, inverse bremsstrahlung and resonance absorption are the dominant mechanisms for producing hot electrons, and SLAC RP uses Meyerhofer's empirical scaling of Equation (1) to calculate T_h in units of keV for normalised laser intensity $I\lambda^2 < 1.6\text{x}10^{17}$ W-μm^2/cm^2 [17].

$$T_h = 6\times10^{-5}\left(I\lambda^2\right)^{\frac{1}{3}} \quad (1)$$

At higher laser intensities, when $I\lambda^2 \geq 1.6\text{x}10^{17}$ W-μm^2/cm^2, the ponderomotive force is the primary electron heating mechanism, and it is defined as the force that a dipole experiences in an oscillating electromagnetic field. In the case of a laser-plasma interaction, the free electrons in the plasma experience the oscillating electric field of the incident laser. Equation (2) is used to calculate T_h-based on the ponderomotive force where M_e is the electron rest mass (511 keV) [18] [19].

$$T_h = M_e \times \left(\sqrt{1.0 + I\lambda^2/1.37\times10^{18}} - 1.0\right) \quad (2)$$

Figure 1 shows the distinct inflection point at $I\lambda^2$ = 1.6x10^{17} W-μm^2/cm^2 from the combination of Equations (1) and (2) for calculating T_h. The value of T_h is directly proportional to the photon dose generated through bremsstrahlung of hot electrons with the laser's target and target chamber's walls. The SLAC RP model for T_h provides a conservative approach at estimating the photon dose yield from laser-matter interaction.

Measurements of high-intensity laser induced ionising radiation at SLAC

Taiee Liang[1,2], Johannes Bauer[1], Maranda Cimeno[1], Anna Ferrari[3], Eric Galtier[1], Eduardo Granados[1], James Liu[1], Bob Nagler[1], Alyssa Prinz[1], Sayed Rokni[1], Henry Tran[1], Mike Woods[1]
[1]SLAC National Accelerator Laboratory, Menlo Park, CA US
[2]Georgia Institute of Technology, Atlanta, GA US
[3]Institute of Radiation Physics, Dresden, Germany

Abstract

A systematic study of measurements of photon and neutron radiation doses generated in high-intensity laser-target interactions is underway at SLAC National Accelerator Laboratory using a femtosecond pulsed Ti:sapphire laser (800 nm, 40 fs, up to 1 J and 25 TW) at the Linac Coherent Light Source's (LCLS) Matter in Extreme Conditions (MEC) facility. Preliminary results from recent measurements with the laser-optic-target system (peak intensity $1.8x10^{18}$ W/cm^2) are presented and compared with results from calculations based on analytical models and FLUKA Monte Carlo simulations.

Introduction

The number and use of high-intensity (multi-terawatt and petawatt) lasers in research facilities has seen a rapid rise in recent years. These lasers can now be used in conjunction with research programmes in III- and IV-generation light sources to study matter under extreme conditions [1], or as sources of particle acceleration [2].

High-intensity laser-matter interaction in vacuum can create a plasma, and further laser interactions with the plasma can accelerate electrons in the plasma up to 10's to 1000's of keV [3-9]. These "hot" electrons will interact with the laser target and the target chamber and generate bremsstrahlung X-rays [10-11]. This mixed field of electrons and photons can be a source of ionising radiation hazard for personnel working on or near such systems if sufficient radiological controls are not implemented. Currently, there is limited information on the ionising radiation hazards associated with such laser-matter interactions, and on controls for such hazards. Characterisation of the radiation source term, understanding the radiological hazards, and development of appropriate measures to ensure personnel safety in this rapidly rising field are needed.

SLAC Radiation Protection (RP) Department, in conjunction with the Linac Coherent Light Source (LCLS) Laser Division, has embarked on a systematic study to measure ionising radiation under controlled experiments using the high-intensity, short-pulse laser of the LCLS's Matter in Extreme Conditions (MEC) instrument [12].

As part of this on-going effort, SLAC RP has also been developing analytical models to estimate radiation yield (Sv/J) and performing Monte Carlo simulations to characterise the measured data more accurately [13-16]. Another goal from the measurements is to evaluate the performance of various types of active and passive detectors in the laser-induced radiation fields. The purpose of these studies is to evaluate the efficacy of shielding for protection of personnel from the ionising radiation and to develop accurate

loss scenario considered here, it will be prudent to exclude personnel access to the AP30 service building during mu2e beam operations.

Acknowledgements

Consultation with a rather large group of people was required to produce this work. First and foremost, the author acknowledges the contributions by Don Cossairt and Nikolai Mokhov for insights into the skyshine problem and for application of the MARS code to solve it.

Vladimir Nagaslaev provided the incident beam parameters for the resonant extraction system as well as the layout of the ESS septa placement and angles. Jim Morgan provided the design layout of the extraction system along with beam line coordinates and magnet currents. Carol Johnstone provided starting alignment data for the extraction line components. Corey Crowley designed the modular in-tunnel shielding system. Brian Hartsell provided the preliminary electrostatic septa mechanical design adapted for the model. Mike Vincent provided the C-magnet geometry. Rob Kutschke and Andrei Gaponenko made advances in MARS grid job submission procedures and taught the author to use them. Steve Werkema provided general help and consul in the development and execution of this model and the many previous versions. He also reviewed this paper and is partly responsible for whatever clarity of thought it may provide. Finally, the calculations used to produce results presented here required many years of process time. This work would not have been possible without the support of the Fermilab grid computing system.

References

[1] Mu2e Collaboration (2012), Mu2e Conceptual Design Report, arXiv:1211.7019 [physics.ins-det].

[2] Fermilab Radiological Controls Manual, http://esh.fnal.gov/xms/FRCM.

[3] N.V. Mokhov (1995), "The Mars Code System User's Guide", Fermilab-FN-628, N.V. Mokhov, S.I. Striganov, "MARS15 Overview", Fermilab-Conf-07/008-AD (2007); *Proc. of Hadronic Shower Simulation Workshop*, Fermilab, September 2006, *AIP Conf. Proc.* 896, pp. 50-60 (2007); http://www-ap.fnal.gov/MARS/.

[4] http://www.grc.nasa.gov/WWW/k-12/airplane/atmosmet.html.

Finally, the result of the direct calculation, which includes direct and skyshine sources as a function of floor in Wilson Hall, corresponding to an angle of 23 degrees in azimuth relative to the forward incident beam direction, is shown in Figure 17. The first floor does not receive a direct contribution from the AP30 service building since the areas share a common elevation. The direct effective dose rate contribution at a given floor can be approximated by subtracting the first floor rate from the combined rate. Wilson Hall is a massive concrete structure. No credit is taken for the shielding provided by the building. Consequently, the calculations are conservative except perhaps where offices are located in the glass-walled cross-overs at the south face of Wilson Hall.

Figure 17. The combined skyshine/direct effective dose rate as a function of floor elevation in Wilson Hall is shown at the arrow in the plot

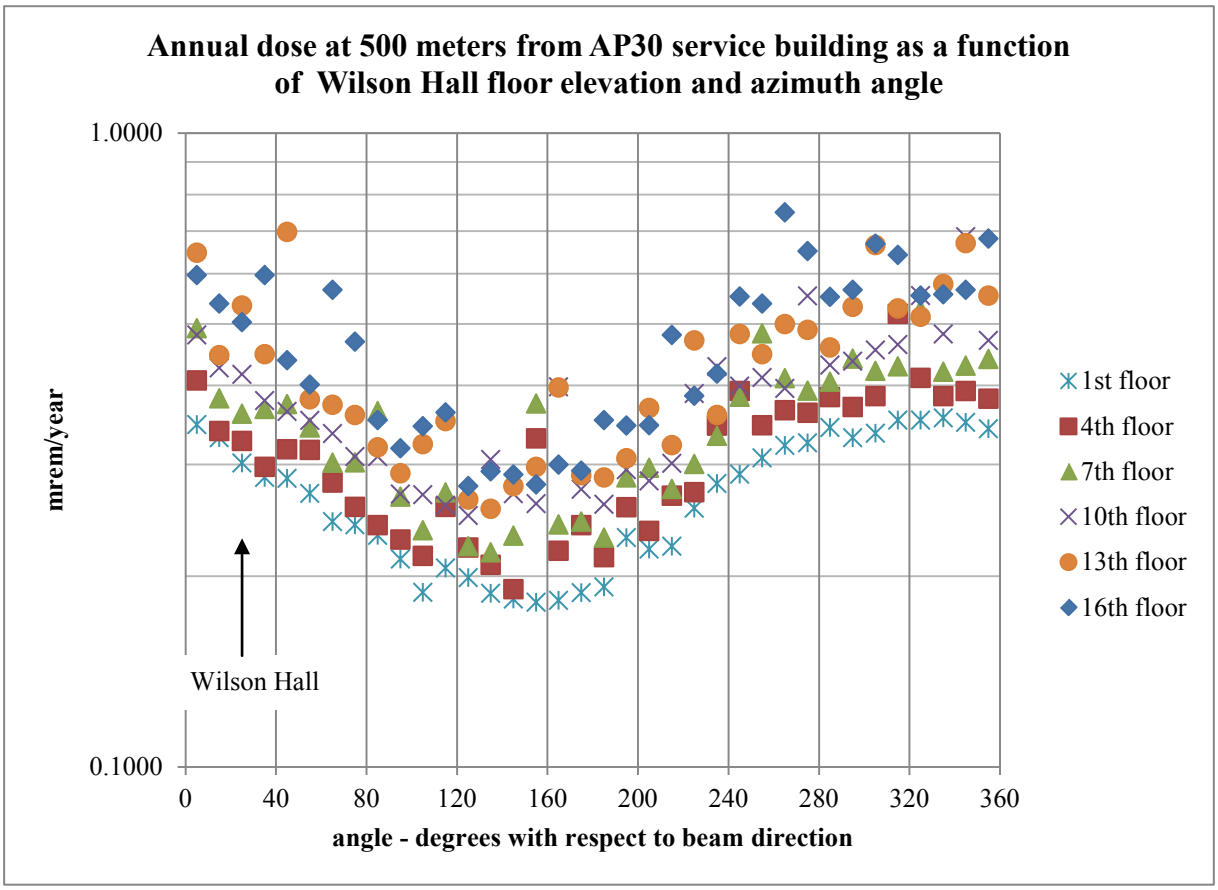

The difference between the 1st floor and other floor effective dose rates is due to the direct effective dose rate.

Conclusions

A model of the resonant extraction system has been created in which 1.25% beam losses are realistically distributed. A supplemental shield system design has been produced. The resulting calculated skyshine and direct effective dose rates fall within all limitations of the Fermilab Radiological Controls Manual. However, an active protection system will be required to limit radiation effective dose rates significantly higher than those calculated in the work reported here. Additional sources of beam loss at the antiproton source facilities could lead to additional sources of skyshine. Those additional sources must be included with the results reported here when/if they are observed. Based upon the beam

Figure 15. The annual radiation effective dose rate for continuous Mu2e operation in the 5 km TE detector is shown in blue while statistical errors are shown in red as a function of distance from the centre of the model

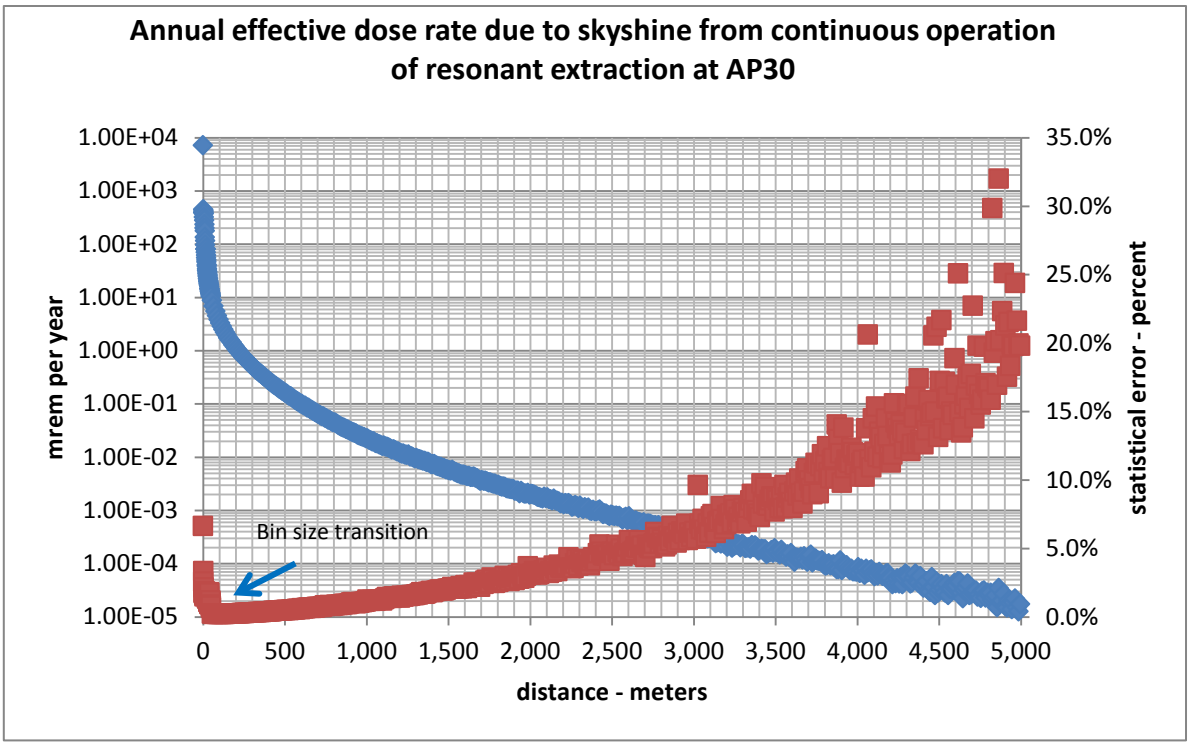

Figure 16. Histogram of prompt effective dose rate in mrem/hr for slow resonant extraction of 8 GeV, 8 kW beam loss with 1.25% beam loss

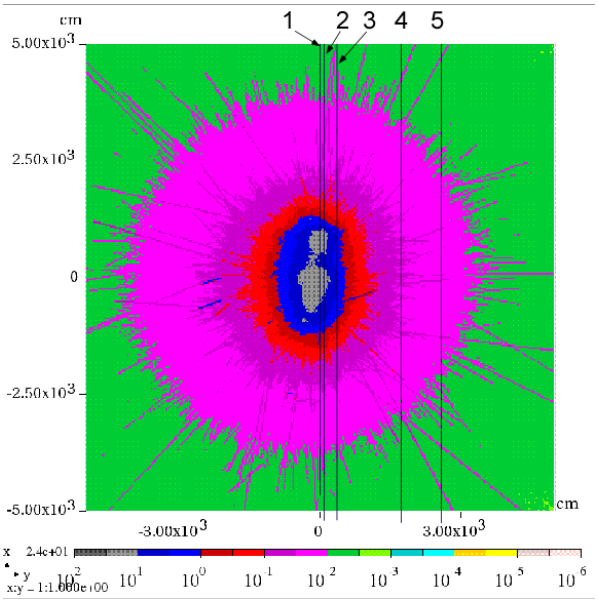

Enumerated lines legend is: 1. Delivery Ring centreline, 2. Tunnel outer concrete edge, 3. Edge of service building; 3/4. Parking Lot; 5. Edge of Indian Road.

Figure 14. Plan view of average total effective dose rate in mrem/hr for ten 1 km layers of atmosphere above the AP30 service building (continued)

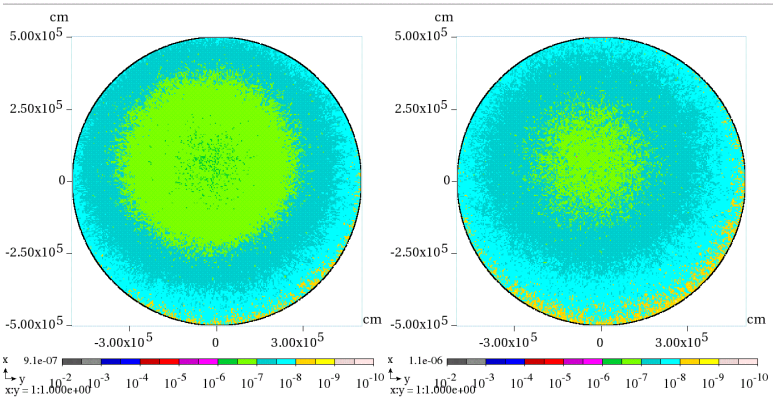

Layer 7 and 8

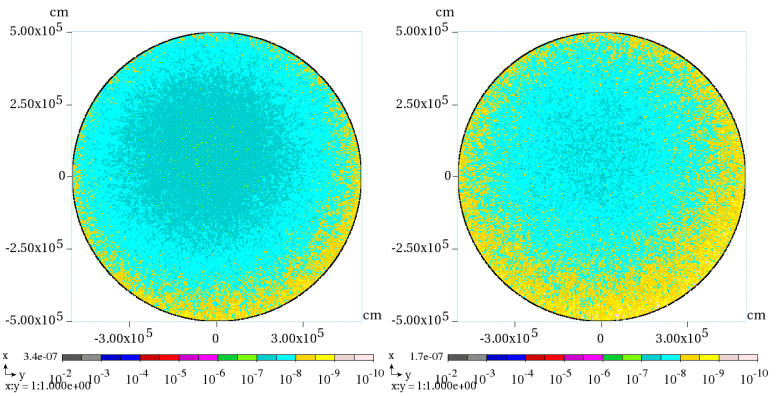

Layer 9 and 10

Figure 14. Plan view of average total effective dose rate in mrem/hr for ten 1 km layers of atmosphere above the AP30 service building

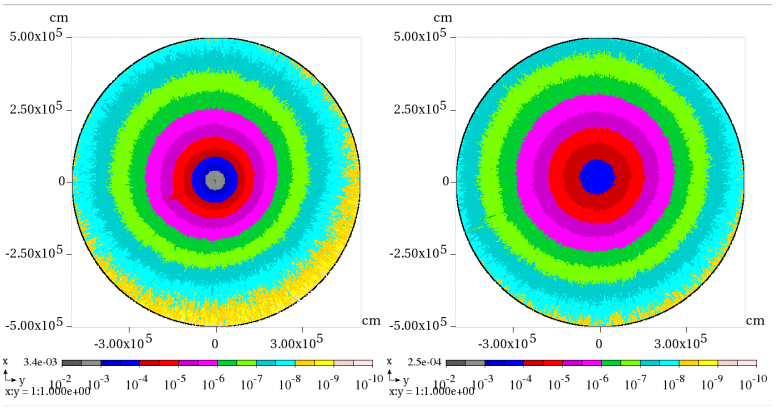

Layer 1 and 2

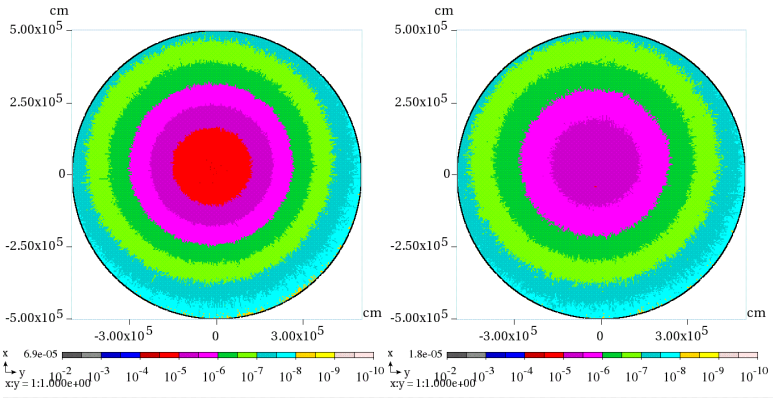

Layer 3 and 4

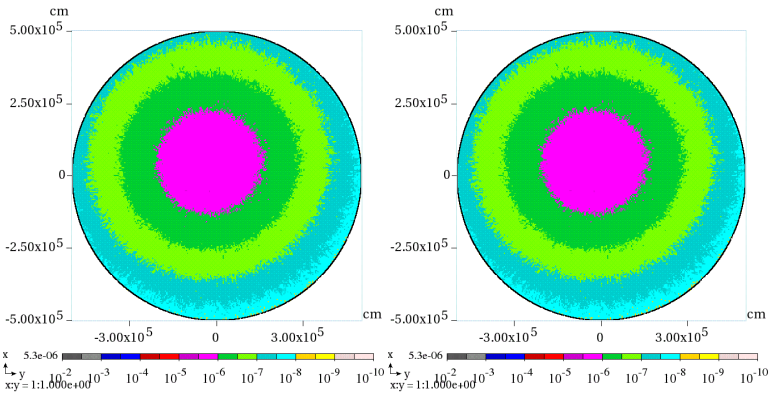

Layer 5 and 6

MARS skyshine and direct results

Histograms in elevation view of total effective dose rate for the 8 kW proton beam extraction with a 1.25% beam loss are shown in Figure 13. The plume in the xz plane is tipped due to the forward momentum tendency of the emerging particle shower. The plume in the yz plane is tipped to beam left due to the proximity of the beam transport system adjacent to the tunnel wall at beam right; i.e. the tunnel wall suppresses the plume at beam right.

Figure 13. The prompt total effective dose rate in mrem/hr is shown for the xz plane on the left and the yz plane on the right

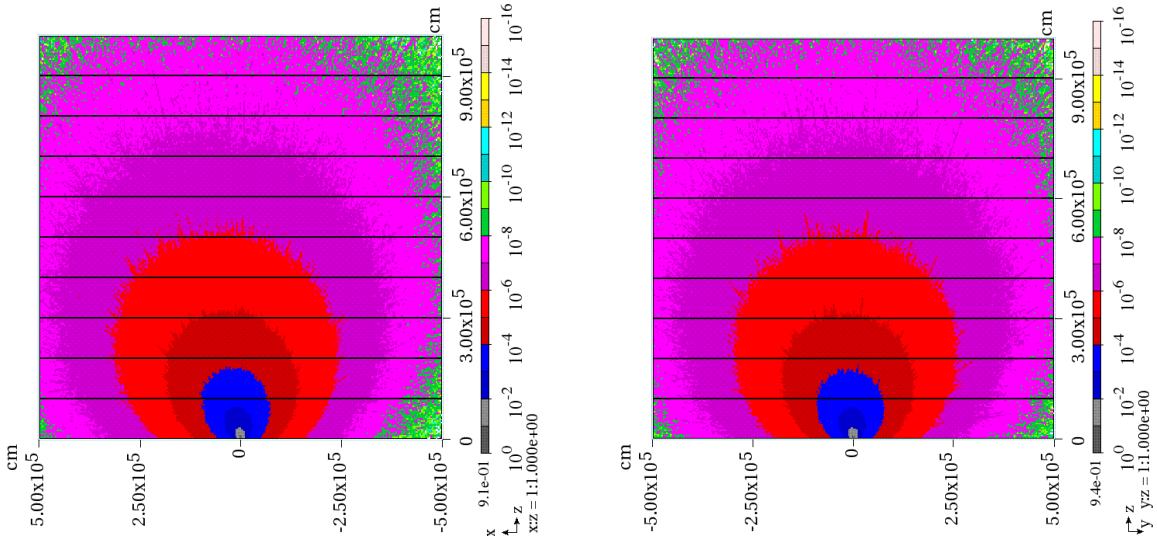

Histograms in a plan view of total effective dose rate for the 8 kW proton beam extraction with a 1.25% beam loss are shown in Figure 14. The non-symetric nature of the plume is further amplified in these images.

The result of total effective dose rate in the 5 km radius TE detector is shown in Figure 15. The dose rate at Wilson Hall (500 m) is 0.17 mrem per year

The result for prompt effective dose rate in the volume histogram in the vicinity of the AP30 service building is shown in Figure 16.

The stage 2 run particle files were used as source terms for the third (skyshine) and fourth (direct) calculations. Figure 11 shows the location in elevation at which the particle source files were written. Histograms indicating the total flux during the stage 1 and stage 2 runs are shown in Figure 12.

Figure 11. Elevation view of AP 30 service building showing elevations at which stage 1 and stage 2 particle showers were collected

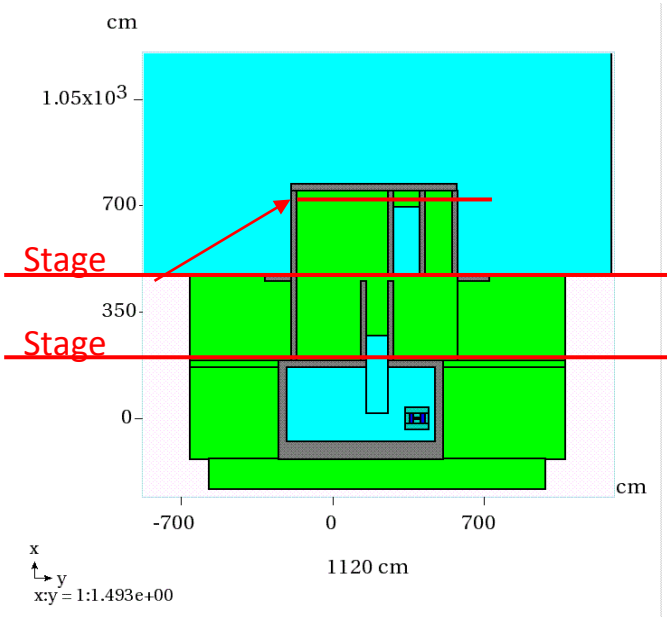

Figure 12. Longitudinal elevation views in the plane of the proton beam

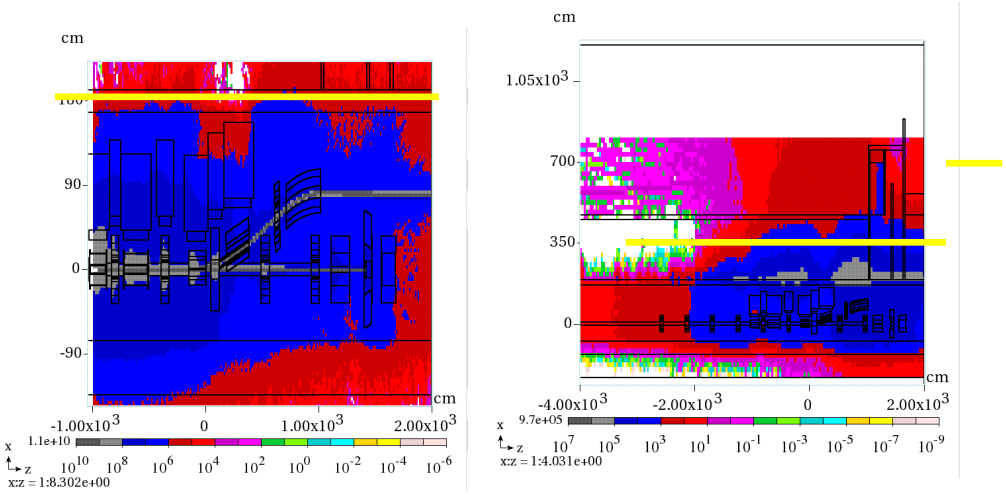

Histograms of total flux created during the stage 1 (left) and stage 2 (right) runs are indicated. The yellow lines indicate particle collection surfaces for the two runs.

assumed to be constant throughout each layer. The atmosphere was modelled with weight fractions of the following elements: nitrogen (0.746), oxygen (0.24), argon (0.013), and hydrogen (0.001). The density of the atmosphere was found to have a profound effect on the shape of the plume.

Wilson Hall, the 16 story central laboratory building, is sited approximately 500 m from the AP30 service building. This building would be exposed to radiation directly emitted from the surface of the AP30 service building floor. A second MARS skyshine model, referred to as the DIRECT model, was also employed to determine radiation effective dose rate as a function of floor at Wilson Hall, due to direct and skyshine radiation sources. The model, created in root geometry, consists of at TE cylindrical shell centred on the AP30 service building with a radius of 500 m and a height of 70 m corresponding to the height of Wilson Hall. The TE cylinder was subdivided into 16 layers representing the approximate division of floors within Wilson Hall. Each of the layers was subdivided into 10 degree bins in azimuth. The details of the model are illustrated in Figure 10.

Figure 10. The blue arrow points to the approximate location of the slow resonant extraction system in the AP30 service building

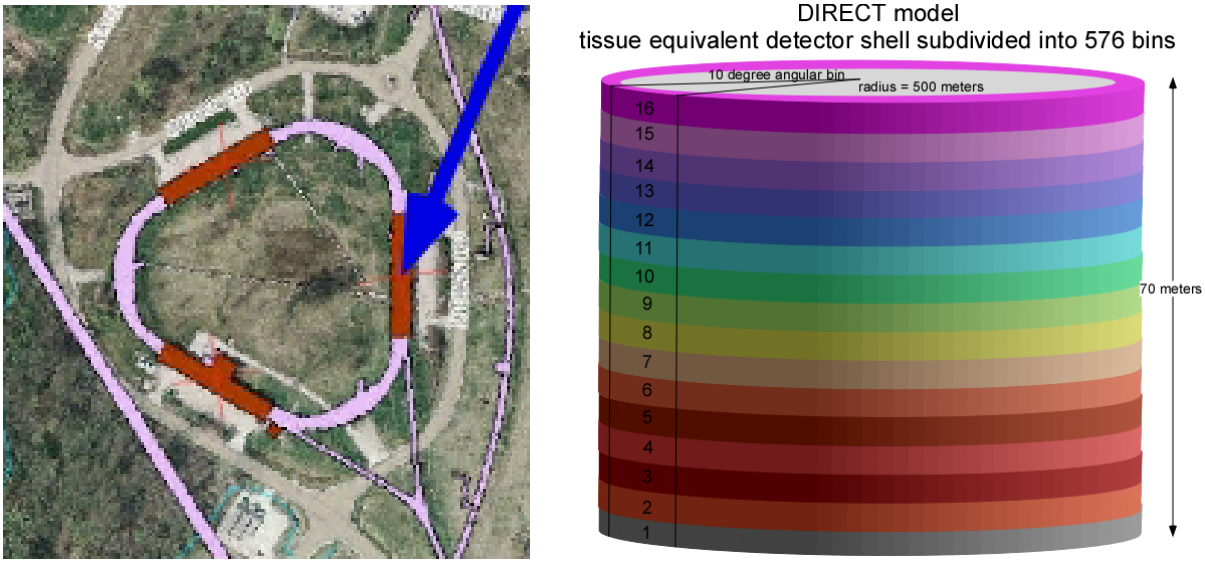

The tail of the arrow is directed towards Wilson Hall, an angle of 23 degrees relative to the direction of the incident beam. The figure at right shows a representation of the DIRECT model. The layers represent approximate floor locations at Wilson Hall and are further subdivided into 36 angular bins of 10 degrees azimuth. The cylindrical shell is centred at the AP30 service building.

MARS simulations

A series of four MARS simulations was required for this work. In the first run (called stage 1), the 8 GeV proton beam is introduced to the slow resonant extraction system. The resulting shower is propagated through the slow resonant extraction system, the in-tunnel shielding system, and to a surface just outside the tunnel. The goal of the first run is to write a file of shower particles at a surface defined outside the tunnel containing the slow resonant extraction system. The particle file consisting of 2×10^5 to 1×10^6 particles contains the particle type, the weight, energy, positions in x, y, and z and the direction cosines. In the second run (called stage 2), the stage 1 particle file is used as a source term to continue propagation of the shower through the remaining shield above the tunnel. A second set of surfaces, the service building floor and the top surface of the stairway structure, were established to collect a new set of shower particles for the stage 2 run.

The placement of the particle source between the TE detector and histogram volumes was intentional. The source propagates upward through the histogram volume, which gives a measure of the direct component. Reflected sky shine passes downward through the histogram volume and provides a pure skyshine component in the TE detector.

Figure 8. Skyshine model feature for radius = 500 m and height = 10 m

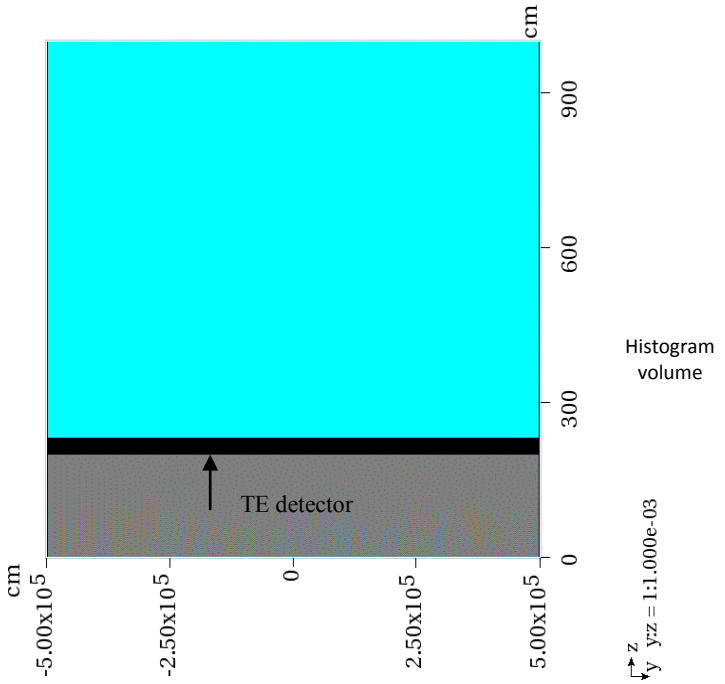

Figure 9. Cross-section of the full model (left), plan view of the model through the TE detector for the first 50 m in radius (right)

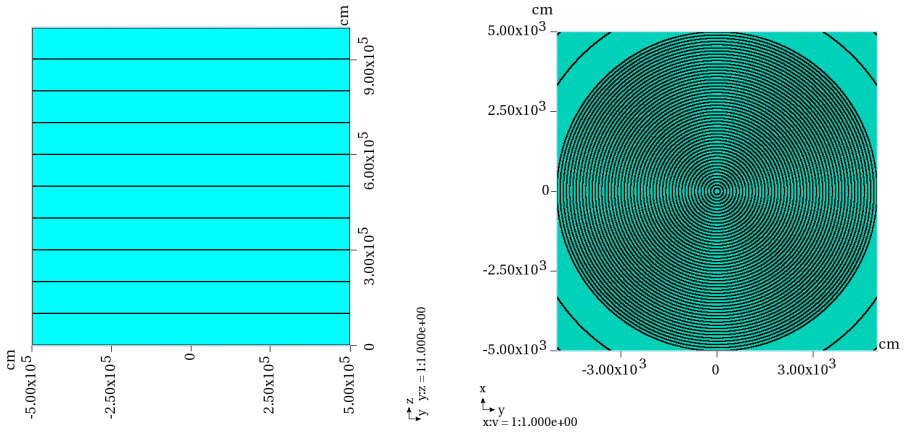

The density of the atmosphere as a function of height was calculated using the NASA earth atmosphere model for the troposphere for altitudes less than 11,000 m [4]. The temperature corrected density was calculated at the elevation for the centre of each of ten 1 km layers (local ground elevation at the AP30 service building is 744 feet) and

Figure 6. Supplemental in-tunnel shielding is shown above the Lambertson magnet

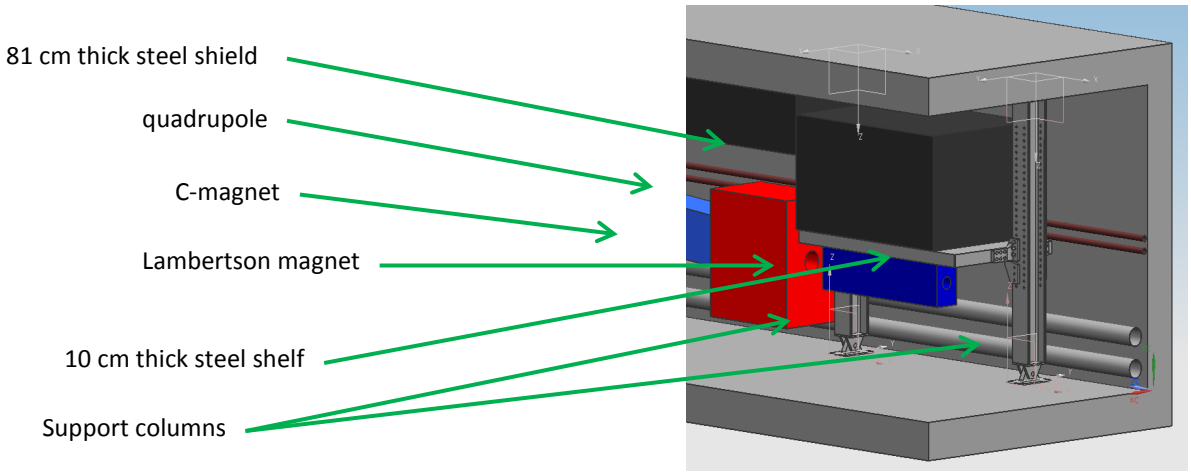

Figure 7. A concrete/marble shield is to be placed in the tunnel adjacent to extraction system components to limit worker radiation exposure during maintenance periods

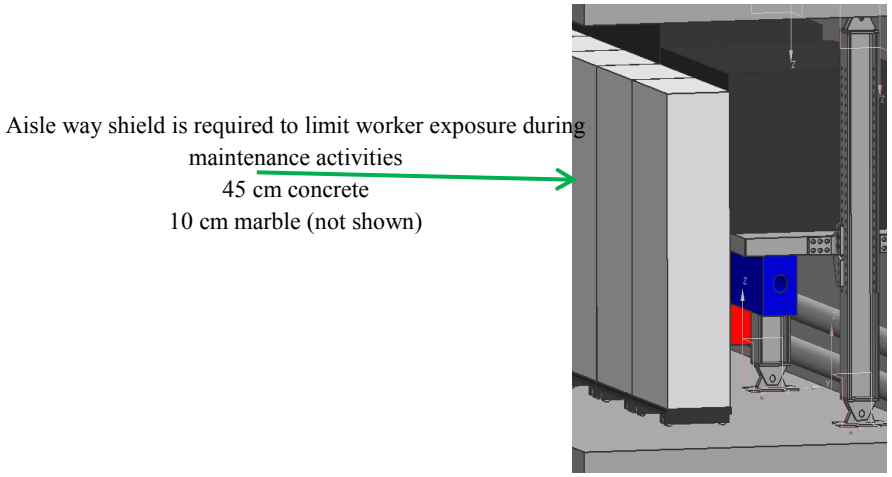

The shields are mounted on movable platforms to facilitate access to extraction system components.

Radiation skyshine model

The radiation skyshine model eventually developed for this work is a cylindrical volume with a radius of 5 km and a height of 10 km. Initially, the goal in making the model was to understand radiation effective dose at a radial distance of 500 metres and a height of up to 500 metres. As work on the calculation proceeded, and because grid computing resources were being employed, it became apparent that a significantly larger atmospheric model could be used without the need for extraordinary calendar time to complete the calculation. Therefore, the dimensions of the model were increased.

The base of the model is a concrete disk 2 m thick and 5 km radius. A tissue equivalent (TE) layer of detector, 0.3 m in height, covers the concrete disk. For the first 50 m, the TE layer is subdivided into 1 metre radial bins. From 50 m to 5,000 m, the TE disk is divided into 10 m radial bins. A MARS histogram volume (air), 100 m long by 100 m wide by 1.7 m high was placed in the atmosphere just above the TE detector at the model centre. The purpose of this histogram is to determine radiation effective dose rate due to direct and skyshine sources in the service building, the adjacent parking lot, and the nearby service road. Details of the model are shown in Figures 8 and 9.

Figure 5. Extraction system component alignment

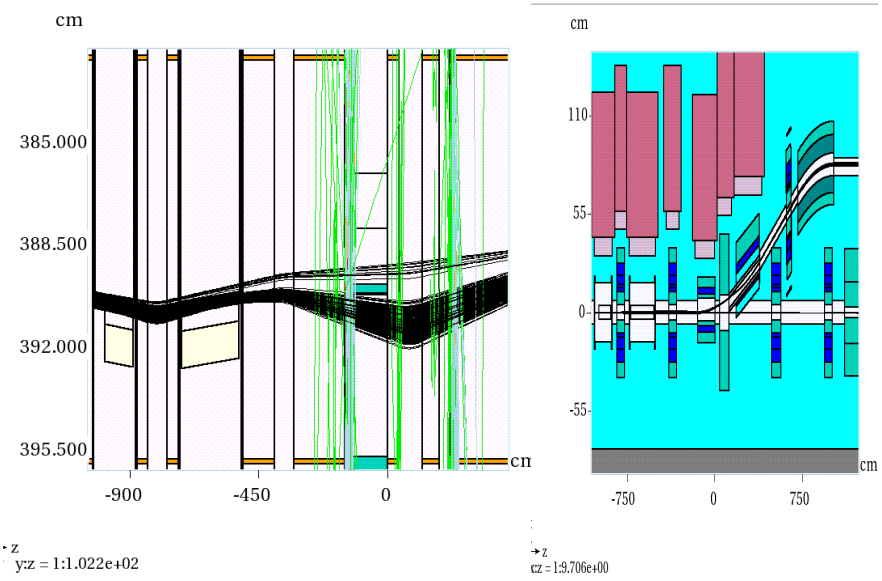

At the left of the figure, the electrostatic septa foil planes are treated as black holes. The separated beams scrape on the misplaced Lambertson magnet resulting in a particle shower indicated by the green neutron traces. The Lambertson magnet is then repositioned so that the separated beams pass cleanly through the circulating and extraction orbits as shown on the right.

Supplemental shielding system

The AP30 service building shielding is limited to 10 feet (3.048 m). Various schemes have been examined to supplement the shielding externally but all options explored were found to be either impracticable or cost prohibitive. An in-tunnel, supplemental shielding system was devised as an alternative. The modular shield design can be adopted on a location by location basis as required. The design features of such a system are illustrated in Figure 6. Seven of the supplemental systems were incorporated in the MARS model to shield extraction beam losses resulting from the electrostatic septa, Lambertson magnet, C-magnet, and three quadrupoles in Figures 3 and 5.

In addition to the steel shield shown in Figure 6, a composite concrete/marble shield is to be located in the aisle of the tunnel adjacent to the extraction devices. Residual radiation dose rates due to the unavoidable 100 watt extraction beam loss will be shielded to limit worker exposure during delivery ring maintenance periods. Figure 7 shows an illustration of the aisle shield.

The 2 m long Lambertson magnet (ELAM in Figure 3) is the limiting aperture in the extraction system. Cross-section views of the circulating and extraction apertures are illustrated in Figure 4. The circulating beam in the delivery ring passes through the non-field region of the Lambertson magnet while the extracted beam passes through the field region where it is deflected vertically upward. A part of the beam which intersects the foil plane scatters and is lost in the Lambertson magnet at the septum, a 3 mm wide steel divides the circulating and extraction channels. The septum acts as a magnetic field flux return; consequently, its design thickness is a constraint, which results in unavoidable beam loss.

Figure 4. Beam position at the upstream and downstream ends of the Lambertson magnet apertures (left)

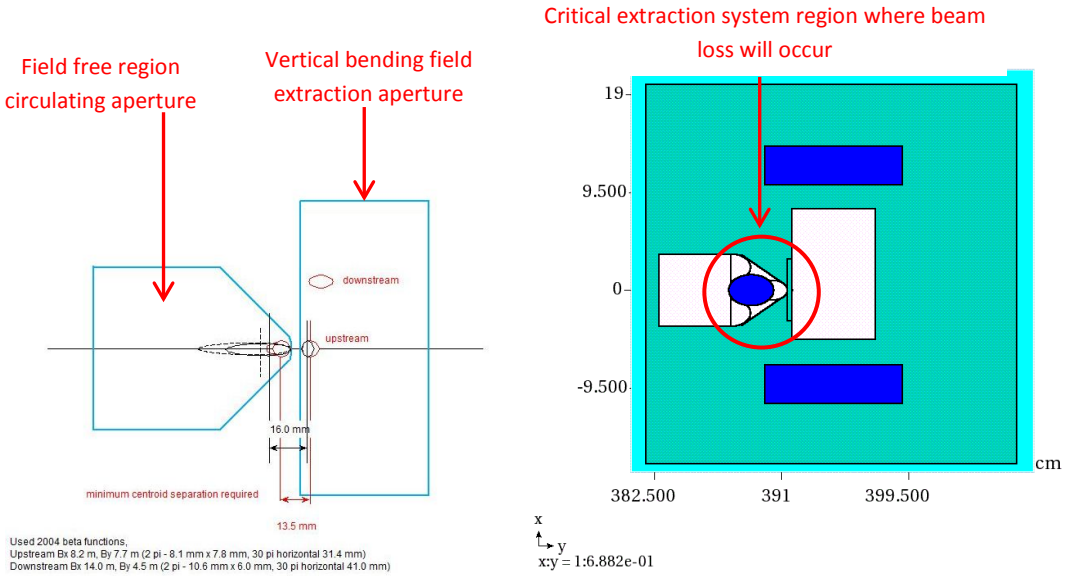

Beam scattered by the electrostatic septa foils is stopped in the steel in the region depicted by the circle in the right image.

In the MARS model, alignment of the extraction system components is necessary to optimise beam transmission and minimise beam loss. Scattering of the proton beam incident on the electrostatic septa foil planes is unavoidable. Losses from scattering in the foils are indistinguishable from losses due to misalignment of extraction system magnets. Therefore, to aid in the alignment process, the wire plane foils are temporarily treated as black holes. This permits the positioning of the extraction Lambertson, C-magnet, and other extraction line components to minimise beam loss. Once loss-free extraction positions are determined, the foil planes are returned to their normal material properties to establish conditions for normal beam loss. Surface detectors were also included in the model to determine the fraction of the beam lost in the tracking studies shown in Figure 5. The total beam loss for the region is estimated to be 1.25% or about 100 watts.

Figure 1. Longitudinal elevation view of the MARS model

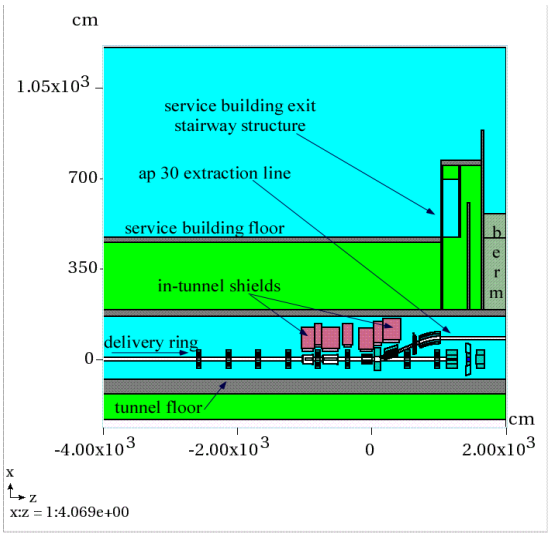

The shielding berm increases to 13 feet (3.96 m) just downstream of the indicated stairway. The AP 30 Service Building walls and roof are not shown in the figure.

Figure 2. Shielding details of the exit stairway

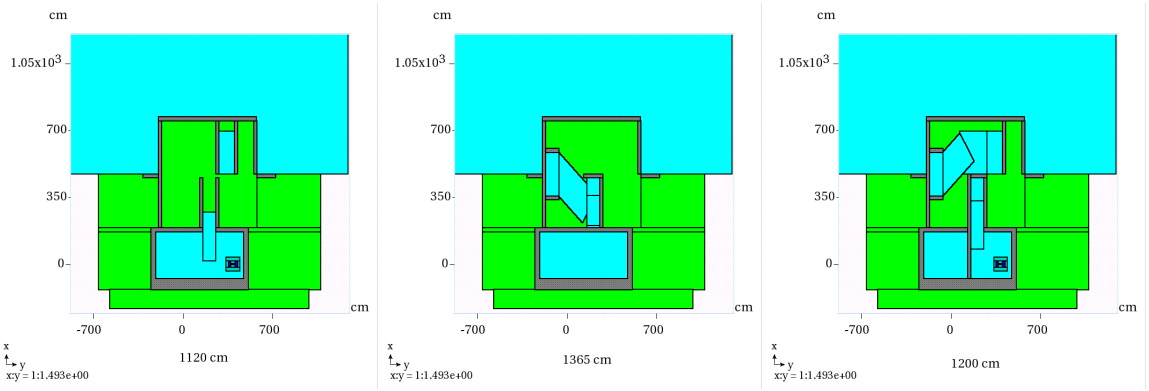

Figure 3. Delivery ring and extraction system details in a series of expanded views

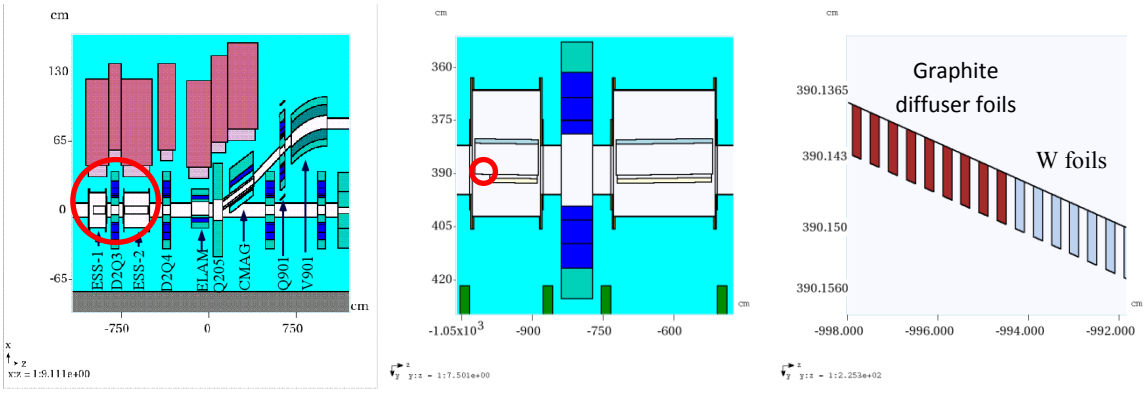

Horizontal scales for the images are left, 20 m; middle, 6 m, and right, 0.06 m.

Radiation skyshine calculation with MARS15 for the Mu2e Experiment at Fermilab

A.F. Leveling
Fermi National Accelerator Laboratory, US

Abstract

The Fermilab Antiproton source is to be repurposed to provide an 8 kW proton beam to the Mu2e experiment by 1/3 integer, slow resonant extraction. Shielding provided by the existing facility must be supplemented with in-tunnel shielding to limit the radiation effective dose rate above the shield in the AP30 service building. In addition to the nominal radiation shield calculations, radiation skyshine calculations were required to ensure compliance with Fermilab Radiological Controls Manual. A complete model of the slow resonant extraction system including magnets, electrostatic septa, magnetic fields, tunnel enclosure with shield, and a nearby exit stairway are included in the model. The skyshine model extends above the beam enclosure surface to 10 km vertically and 5 km radially.

Facility overview

The dominant source of radiation dose during Mu2e operation is the delivery ring extraction system, located in the beam enclosure below the AP30 service building. The AP30 anti-proton source service building was originally designed in conjunction with the accumulator/debuncher rings for a mW power, secondary anti-proton beam and could be operated nominally at up to 13 watts of 8 GeV primary proton beam. The shield between the beam tunnel and service building is 10 feet thick (3.048 m). The anti-proton source debuncher ring (now, the delivery ring) is being reconfigured to condition and extract an 8 kW, 8 GeV proton beam by 1/3 integer, slow resonant extraction, a relatively lossy process. If this facility was to be built in a “green field”, a shielding thickness of 18 to 22 feet might be chosen. To compensate for the shielding deficit, an in-tunnel steel shielding system has been designed. A MARS model of the existing facility was created which includes a portion of the delivery ring, the slow resonant extraction system, extration beam line, and a nearby exit stairway. A longitudinal elevation view of the facility model is shown in Figure 1 while transverse elevations views which illustrate details of the exit stairway are shown in Figure 2.

Extraction system configuration and alignment

Details of the MARS model for the extraction system including a portion of the delivery ring, the electrostatic septa, various quadrupoles, extraction Lambertson magnet, C magnet, and vertical bending magnet are shown in Figure 3. The model includes magnetic fields in the quadrupole and bending magnets. The electric fields of the electrostatic septa are approximated by a magnetic field vector at 90 degrees to the nominal electric field. A total of 850 graphite and tungsten foils are included in the model.

[4] M. Brugger et al. (2011), "FLUKA Capabilities and CERN Applications for the Study of Radiation Damage to Electronics at High-Energy Hadron Accelerators", presented at the SNA+MC, 17-21 October 2010, Tokyo, Japan, published by Atomic Energy Society of Japan in *Progress in NUCLEAR SCIENCE and TECHNOLOGY*; 948-954.

[5] A. Ferrari, P.R. Sala, A. Fassò, J. Ranft (2005), "FLUKA: a multi-particle transport code", CERN 2005-10 (2005), INFN/TC_05/11, SLAC-R-773.

[6] G. Battistoni, S. Muraro, P.R. Sala, F. Cerutti, A. Ferrari, S. Roesler, A. Fassò, J. Ranft (2007), "The FLUKA code: Description and benchmarking", *Proceedings of the Hadronic Shower Simulation Workshop 2006*, Fermilab 6-8 September 2006, M. Albrow, R. Raja eds., *AIP Conference Proceeding* 896, 31-49.

[7] R. Froeschl (2013), "The DORIAN code for the prediction and analysis of residual dose rates due to accelerator radiation induced activation", *Proceedings of the AccApp13 Conference 2013*, Brugge, 5-8 August 2013.

[8] M. Huhtinen (1997), "Determination of cross-sections for assessments of air activation at LHC", CERN Internal Report CERN/TIS-RP/TM/97-29.

[9] M. Brugger, D. Forkel-Wirth. S. Roesler, P. Vojtyla (2004), "Effective Dose to the Public from Air Releases at LHC Point 7", CERN-SC-2004-064-RP-TN.

[10] Swiss Federal Council (1994), "Swiss Radiological Protection Ordinance (RPO)", Status as of 1 January 2014, Reference 814.501.

[11] P. Vojtyla (2006), "Calculation of the external effective dose from a radioactive plume by using Monte Carlo dose kernel integration", *Applied Modeling and Computations in Nuclear Science*. Semkow, T. M., Pomme´, S., Jerome, S. M. and Strom, D. J. Eds. *A.C.S. Symposium Series* 945 (Washington, DC: American Chemical Society) pp. 104-114.

Figure 12. Side and top view of the first stack of the CERN Shielding Benchmark Facility (CSBF)

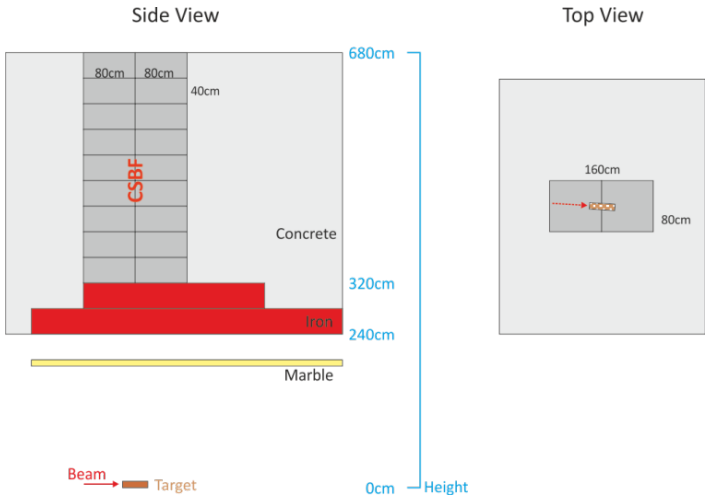

Conclusions

The CERN High Energy Accelerator Mixed Field (CHARM) Facility is currently constructed in the CERN PS East Experimental Area and will provide test locations for electronic equipment with well understood, mixed radiation fields to the CERN Radiation2 Electronics (R2E) project to study radiation effects on electronic components.

The radiation protection assessment of the facility has been presented. It has been split into the shielding design for the prompt radiation, the optimisation of the residual radiation and the activation of air and its subsequent release to the environment. It has been demonstrated that the CHARM will fulfill the CERN radiation protection requirements.

The CERN Shielding Benchmark Facility (CSBF) will be incorporated into the roof shielding structure of the CHARM Facility and will make parasitic use of the beam on the CHARM target for characterisation studies of the shielding properties of various materials for radiation fields laterally from a target after deep shielding penetration.

According to the current schedule, the CHARM Facility was expected to receive beam from the PS in July 2014.

Acknowledgements

We would like to thank the team members of the PS East Experimental Upgrade project for their support.

References

[1] www.cern.ch/charm.

[2] www.cern.ch/r2e.

[3] M. Brugger (2012), “Radiation Damage to Electronics at the LHC”, May 2012, *Conf.Proc.* C1205201, 3734-3736, Presented at Conference, C12-05-20.1, *Proceedings IPAC-2012-THPPP006.*

Figure 11. Annual effective dose to members of the public as a function of the air tightness

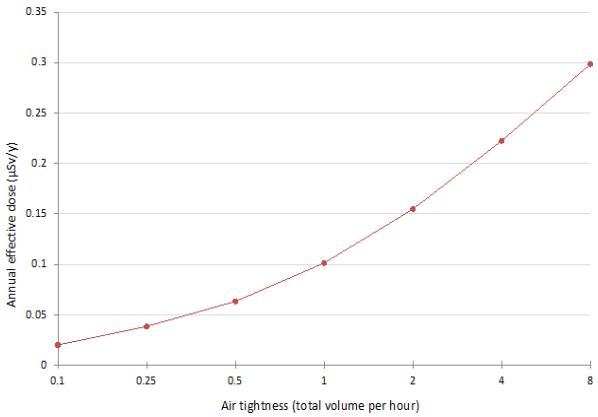

CERN Shielding Benchmark Facility (CSBF)

The CERN Shielding Benchmark Facility (CSBF) will be incorporated into the roof shielding structure of the CHARM Facility. The main purpose of the CSBF is the characterisation of the shielding properties of various materials for radiation fields laterally from a target after deep shielding penetration. In addition, these radiation fields can be used for detector calibration and detector inter-comparison studies.

The CSBF will make parasitic use of the radiation field generated by the impact of the beam on the CHARM target. The detailed design is still on-going and aims to minimise the impact on the operation of the CHARM Facility.

Figure 12 shows a side view and a top view of the first part of the CSBF. Situated vertically above the CHARM target and embedded into the roof shielding structure, the first part of the CSBF consists of a stack of 9 layers. Each layer is 40 cm high and consists of 2 concrete slabs of 80 cm x 80 cm area. Below the CSBF are cast iron of 80 cm thickness and marble of 10 cm thickness. The first part of the CSBF starts at a distance of 320 cm from the centre of the CHARM target. A second stack with identical layout will be placed further downstream.

Some concrete slabs can be replaced by slabs of the shielding material to be characterised. It will also be possible to place detectors inside the CSBF into hollow spaces created by dedicated support structures. These support structures will also provide cable feed-throughs. The characterisation studies of the inserted shielding materials will be performed with neutron detectors and activation samples.

The following methodology has been used to obtain the radionuclide concentrations, the annual release to the environment and the resulting annual effective dose to members of the public:

- The track-length spectra for protons, neutron and charged pions have been scored in the air volumes inside the CHARM Facility (and the upstream proton facility) in the FLUKA Monte Carlo simulation.
- These track-length spectra have been folded with a dedicated set of air activation cross-sections [8] [9] to obtain the radionuclide production yields.
- The radionuclide concentrations in the facility and the release term to the environment have been calculated from the radionuclide production yields taking the time evolution and the characteristics of the ventilation circuit into account.
- The radionuclide concentrations in the facility after beam stop have been converted to the committed effective dose due to inhalation without flush for a 1-hour access by application of exposure-to-dose conversion coefficients for inhalation [10]. The decrease of the radionuclide concentrations due to decay during the 1 hour period has been taken into account.
- The release term has been converted to the effective dose to members of the public by application of release to effective dose conversion coefficients, computed with a dedicated Monte Carlo integration program EDARA [11].

The obtained committed effective dose due to inhalation and the effective dose to members of the public are given in Table 3 for static confinement with one flush every week and dynamic confinement with an extraction rate of 1 air volume per hour. To meet design goal 1, dynamic confinement with a flush before access has been chosen. As shown in Figure 11, to meet design goal 2, the effective dose to members of the public has been calculated as a function of the air tightness, which corresponds to the extraction rate to ensure dynamic confinement of the facility. A design goal for the air tightness of 2 air volumes per hour has been set to preserve enough margin for the overall design goal of 1 µSv per year for the effective dose to members of the public (reference group).

Table 3. Radiological impact of air activation for different confinement types

Confinement type	Committed effective dose due to inhalation without flush* for 1 hour access µSv	Release to the environment TBq/y	Effective dose to members of the public µSv/y
Static (1 flush/week)	14	0.026	0.0072
Dynamic (1 volume/h)	1.9	2.4	0.10

*These are hypothetical values used only in the assessment. A flush will always be performed before access.

(lower by a factor of 3) when the movable shielding walls have been retracted from the facility during irradiation.

Figure 9. Residual radiation levels after 200 days of operation with maximum beam intensity followed by 1 hour (left) and 1 day (right) of cool-down

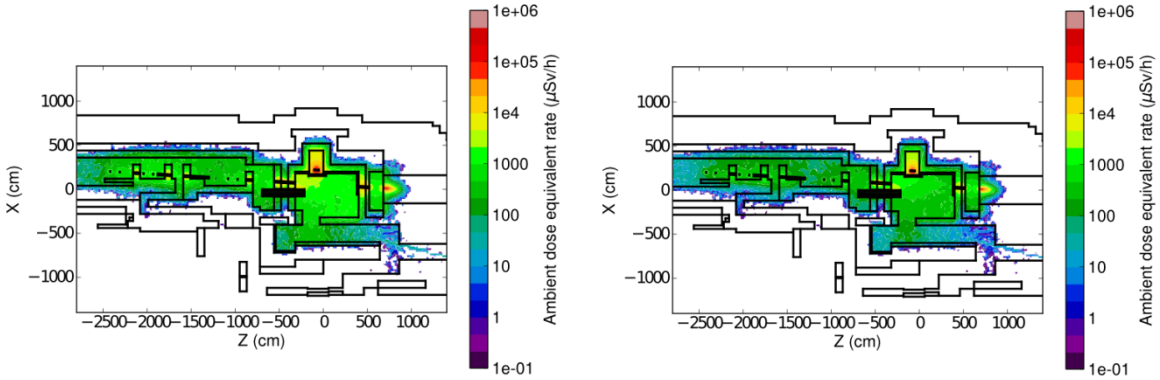

Figure 10. Time evolution of the residual radiation in the Patch Panel area after 200 days of operation with maximum beam intensity

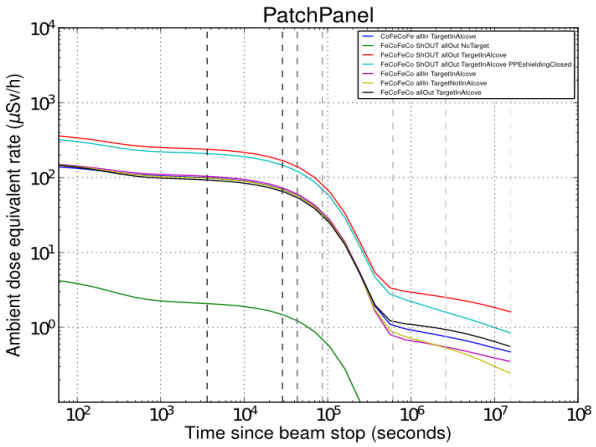

Air activation and subsequent release to the environment

The operation of the CHARM Facility will result in the activation of the air inside the facility. The design goals for the ventilation system of the CHARM Facility are:

- The committed effective dose due to inhalation has to be less than 1 μSv for a 1-hour access. The reason for this requirement is that the inhalation component of the effective dose is not directly monitored. The external exposure due to the activated air is monitored, is not larger for the given geometries than the internal exposure and is normally much smaller than the external exposure from the activated components of the facility.
- Effective dose to members of the public (reference group) has to be less than 1 μSv per year, combined from prompt radiation (sky-shine) and from releases to the environment.

Figure 8. Annual effective dose to members of the public due to sky-shine with nominal beam parameters

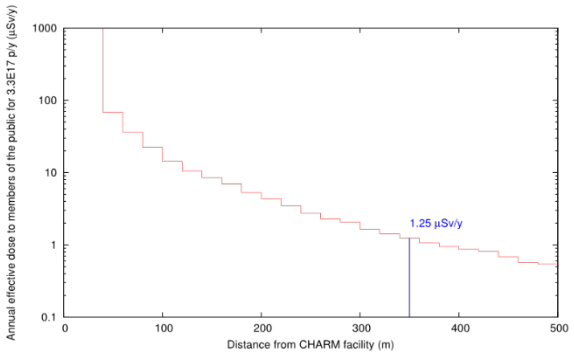

Residual radiation

The reduction of the residual ambient radiation levels is an important optimisation following the ALARA principle. In addition, reducing the residual ambient radiation levels to lower, the effective dose to personnel during interventions will also decrease the administrative requirements for the interventions and, as a consequence, result in a more efficient exploitation of the facility.

The main optimisation measures have been:

- Starting from the beginning, the radiation protection assessment was integrated in the design process of the facility.
- Parts of the concrete walls and the iron ceiling structure in the vicinity of the target have been covered with marble. This will reduce the production of ^{24}Na and ^{22}Na in this area and the marble will act as a shielding material reducing the radiation from the iron ceiling structure.
- The target will be moved to a dedicated alcove during access to the CHARM Facility. This alcove will be closed by a 20 cm thick movable marble shielding reducing the radiation exposure due to the target.
- Extensive studies for different shielding configurations during access have been performed to optimise the access procedures.
- An ambient dose equivalent rate objective of 100 µSv/h for the Patch Panel area (see Figure 4) has been defined. This area will be the most frequently accessed part of the facility.

To predict the ambient dose equivalent rate levels for various operational scenarios and cool-down times, Monte Carlo simulations have been performed with FLUKA and the DORIAN code [7]. The ambient dose equivalent rate levels for 200 days of operation with maximum beam intensity followed by cool-down periods of 1 hour and 1 day are shown in Figure 9. The evolution of the ambient dose equivalent rate for the Patch Panel area for various shielding configurations is presented in Figure 10 as a function of the cool-down time. The ambient dose equivalent rates for the Patch Panel area at cooling time less than 1 day are approximately 3 times higher for the configuration where the movable shielding walls have been retracted from the facility during irradiation than for the configuration where the movable shielding walls have been inside the facility during irradiation. The objective of 100 µSv/h for the Patch Panel area can be achieved for a cooling time of 1 hour for the maximum beam intensity when the movable shielding walls have been inside the facility during irradiation and for the nominal beam intensity

In addition, the shielding had to be designed so that the annual effective dose to members of the public, combined of prompt radiation (sky-shine) and releases to the environment, would be less than 1 μSv for the nominal annual protons on target.

The design of the shielding tried to make use of as many existing concrete and iron shielding blocks as possible as well as magnet yokes that had been part of the former LEP accelerator. In total, approximately 2000 tonnes of iron and 4000 tonnes of concrete have been used. The design had also to accommodate the fact that design choices were limited due to the presence of existing facilities in the East Experimental Area.

Monte Carlo simulations with the FLUKA code [5] [6] have been performed to estimate the prompt ambient equivalent dose rate levels for the CHARM Facility. The prompt ambient equivalent dose rate is shown at the beam-line level in Figure 6 and at 40 cm above the top of the shielding roof in Figure 7, demonstrating the compliance of the shielding design with the design goals with respect to the CERN area classification. The annual effective dose to members of the public due to sky-shine is shown in Figure 8 to be 1.25 μSv for the current design. Since this value is above the design goal of 1 μSv/y, the design of the shielding roof will be modified to respect this design goal. The predicted ambient dose equivalent rate level on the shielding roof will be verified by dedicated measurements during the commissioning of the CHARM Facility because of the large sensitivity of the ambient dose equivalent rate behind thick shielding to the uncertainties of the attenuation properties of the shielding material. This will also be part of the measurement programme for the CERN Shielding Benchmark Facility that is described below.

Figure 6. Prompt radiation at beam-line level with colour-coded area classification (blue covering the acceptable control room levels and green the acceptable low occupancy area levels)

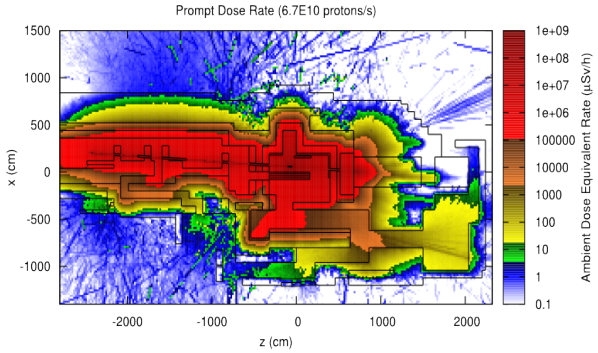

Figure 7. Prompt radiation at 40 cm above the shielding roof with colour-coded area classification (blue covering the acceptable control room levels and green the acceptable low occupancy area levels)

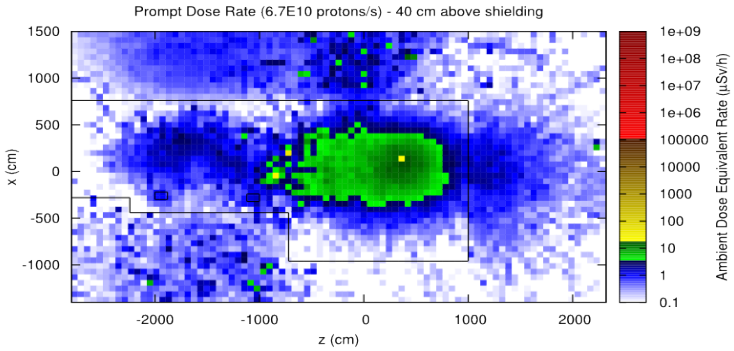

Figure 4. Layout of the CHARM Facility

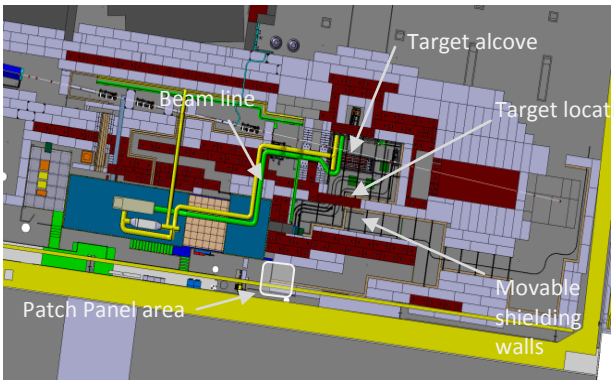

Figure 5. Reverse integral (defined as the integral starting from a given energy up to infinite energy) of the high-energy hadron fluence normalised to the total high-energy hadron fluence above 20 MeV (left) for the LHC tunnel and location 13 in the CHARM Facility

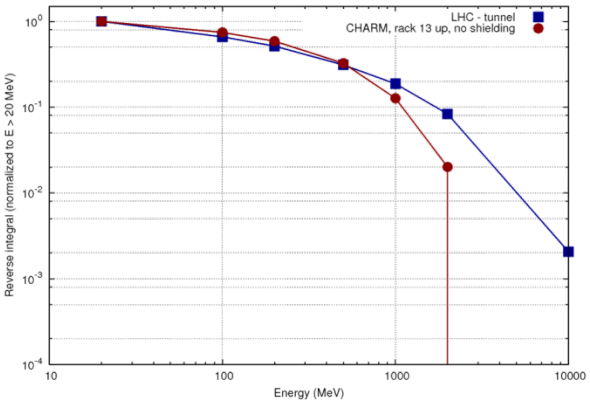

Radiation protection assessment approach

The radiation protection assessment of the facility has been divided into 3 categories that are discussed in the following sections, namely the shielding design for the prompt radiation, the optimisation of the residual radiation and the activation of air and its subsequent release to the environment. The characterisation of the facility with respect to the categorisation of its various parts in terms of radioactive waste classes and their corresponding elimination pathways will be performed in the future.

Prompt radiation

The shielding of the CHARM Facility was designed to respect the CERN area classification. This means that the ambient dose equivalent rates should be below 3 µSv/h for the control rooms inside the East Hall and less than 15 µSv/h (low occupancy area) at 40 cm outside the shielding walls for maximum average beam intensity of 6.7E10 protons per second. In addition, the ambient dose equivalent rates should be below 2.5 µSv/h outside the hall for maximum average beam intensity. These requirements meant that all shielding passages (access chicanes, ventilation ducts, cable ducts) had to be designed in an optimised way. The locations of the area monitors were chosen to verify compliance with these area classification limits.

Within the facility, a 24 GeV/c proton beam extracted from the Proton Synchrotron (PS) accelerator impacts on a cylindrical copper or aluminum target and the created secondary radiation field is used to test electronic equipment installed at predefined test positions. Copper and aluminum as material choices for the primary beam target are good compromises not only because of their mechanical and thermal properties, but together with the mobile shielding configuration they also allow the creation of a secondary particle spectra representative for the source term of those present in the atmospheric, space and accelerators environments.

To model and choose between the various representative spectra, different shielding configurations are thus available in the facility. Four movable layers of an individual thickness of 20 cm made of concrete and iron can be placed between the target and the test locations in different combinations, thus allowing to modulate the test spectra and adopt them as closely as possible to the radiation field (energy and intensity) aimed for during the tests. The shielding plates are motorised with remote control. The intensity of the radiation field can be modulated by varying the primary beam intensity, the choice of target head, e.g. two massive ones (Al or Cu – the yield of the massive Al target is about 2.5 times smaller than for the massive Cu target) or one with reduced effective density (Al target with holes – it gives an additional reduction by a factor 4), allowing for an overall reduction factor (including beam intensity reduction) of the primary radiation field of 10-100, in total.

In summary, the CHARM Facility will receive a pulsed proton beam from the CERN PS with a beam momentum of 24 GeV/c. There will be 5e11 protons per pulse with a pulse length of 350ms. Under nominal conditions, 2 spills per 45.6 seconds, i.e. per PS super-cycle, will be sent to the CHARM Facility. This is the foreseen operation mode of the facility for the next years. Theoretically, up to 6 spills per 45.6 seconds will be possible in case the East Experimental Area is the only user of the test beam cycles of the PS. Table 2 shows the operational parameters accounting for the number of days of operation per year and machine availability.

Table 2. Operational parameters of the CHARM Facility

Scenarios	Average proton beam intensity on target	Annual number of protons on target
Nominal (2spills/45.6s)	2.2E10 p/s	3.3E17 p/y
Maximum (6spills/45.6s)	6.7E10 p/s	1e18 p/y

A sketch of the CHARM Facility is presented in Figure 4. Figure 5 shows the comparison of a representative radiation spectrum in the LHC tunnel and the selected location in the CHARM Facility.

This facility is not only useful for testing devices within accelerator representative environments, but its available radiation fields will also be characteristic of ground and atmospheric environments (neutron energy spectra) as well as the space environment (representative for the inner proton radiation belt). In addition, the size of the available test area is such that also larger objects, and ultimately even objects requiring special services (power, cooling, etc.) to be connected for operation, can be irradiated.

Table 1. Annual High Energy Hadron (HEH) fluences for different radiation environments

Spectrum	HEH fluxes (>20MeV/cm2/year)
Ground level	$1\text{-}2\times10^{5}$
Avionic	2×10^{7}
ISS orbit	1×10^{9}
LHC machine	1×10^{6} - 1×10^{11}
LHC detectors	$> 10^{11}$

The irradiation chamber is large enough to host a complete accelerator control system (e. g. power converters) but can also host full satellites, and part of cars or planes. For SEEs caused by High Energy Hadrons (HEH) present in the various radiation environments, Table 1 provides a generalised overview of annual fluences, later to be put in the context of what can be achieved in terms of test-time acceleration factor at CHARM. In this respect, so far only few mixed field test areas exist, which often do not provide sufficient beam-intensity or flexible test conditions (e.g two CERN test areas, CNRAD and H4IRRAD, but have significant limitations in beam availability, intensity and flexibility).

Layout and operational parameters

As indicated in Figure 1, the CHARM Facility will be located in one of the experimental halls at CERN. Its surrounding layout is composed of iron and concrete blocks in order to reduce maximum radiation outside the shielding structure. A three-dimensional view of the facility and a horizontal cut of the inner target chamber are shown in Figure 3 (a) and (b), respectively. As shown in Figure 3 (a), the target chamber is large enough to host bulky and complete systems (e.g. satellites) as around 70 m^3 of space will be available for radiation tests.

Figure 3: (a) Three-dimensional view of the facility and (b) FLUKA geometry for the target area

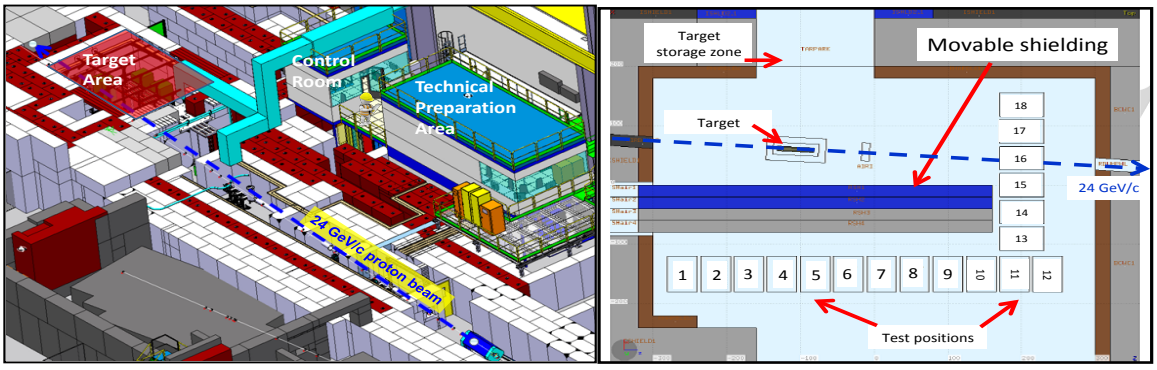

Racks 1 to 18 are the regions representing the test locations. The blue, grey and brown plates are iron, concrete and marbles blocks.

Introduction

The CERN High Energy Accelerator Mixed Field (CHARM) Facility [1] is currently being constructed in the CERN Proton Synchrotron (PS) East Experimental Area. The purpose of the CHARM Facility is to provide test locations for electronic equipment with well understood, mixed radiation fields that are typical of the CERN accelerators and other applications of interest. This facility will complement the existing irradiation facilities at CERN such as CERF and IRRAD.

The location of the CHARM Facility on the CERN site and its connection to the CERN PS are shown in Figure 1.

Figure 1. Location of the CHARM Facility connected to the CERN PS

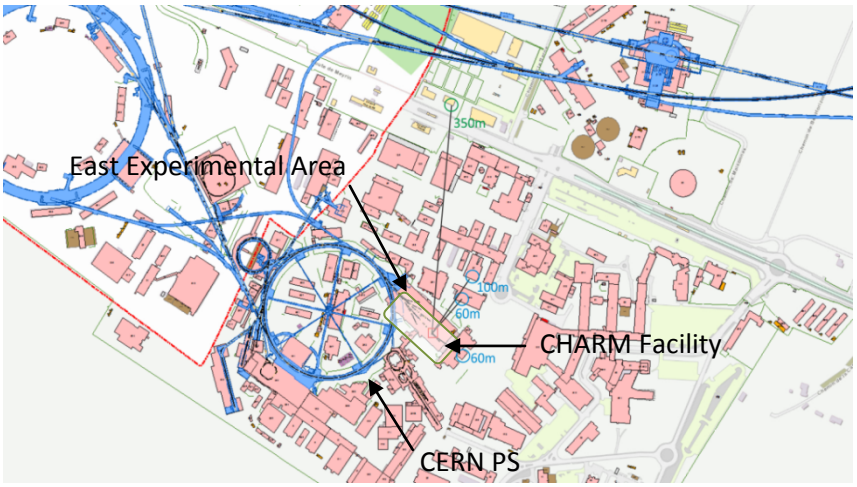

The CHARM Facility will provide test locations for electronic equipment with well understood, mixed radiation fields to the CERN Radiation2 Electronics (R2E) project [2][3][4]. The R2E project was initiated by the observation of significant downtime of the CERN Large Hadron Collider (LHC) due to Single Event Effects (SEE) in electronic devices in the LHC tunnel that triggered the dumping of the LHC beams. This fact is illustrated in Figure 2.

To be able to reach the goal of the R2E project of 0.5 SEE induced beam dumps/fb-1 after the start-up ending the Long Shut-down 1 (LS1) in 2015, extensive testing of electronic equipment that is installed in the LHC tunnel is necessary. The CHARM Facility will provide this testing capability even for tests of entire electronic systems up to dimensions of 1m x 1m x 2m.

Figure 2. LHC beam dumps induced by Single Event Effects (SEE) in electronic devices

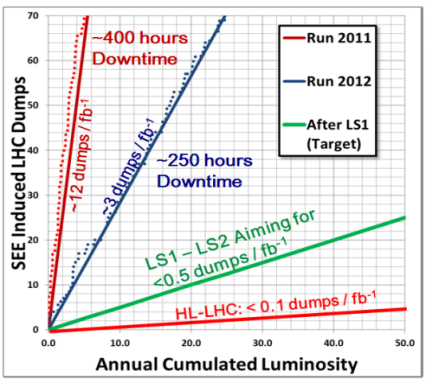

The CERN High Energy Accelerator Mixed Field (CHARM) Facility in the CERN PS East Experimental Area

Robert Froeschl, Markus Brugger, Stefan Roesler
CERN European Organisation for Nuclear Research, Switzerland

Abstract

The CERN High Energy Accelerator Mixed Field (CHARM) Facility is currently being constructed in the CERN PS (Proton Synchrotron) East Experimental Area to study radiation effects on electronic components. The chosen location has become available due to the decommissioning and subsequent dismantling of the DIRAC experiment and the CHARM Facility will share it with a proton irradiation facility that is situated further upstream.

The CHARM Facility will receive a primary proton beam from the CERN PS at a beam momentum of 24 GeV/c and a maximum average beam intensity of 6.7E10 protons/second with a maximum pulse intensity of 5E11 protons/pulse and a respective pulse length of 350 ms. The beam will impinge on one out of a set of dedicated targets to produce the desired radiation fields at several experimental positions. These radiation fields can be adjusted by insertion of up to four moveable shielding walls, two made out of concrete and two made out iron. The main purpose of the CHARM Facility will be the investigation of the effects of these radiation fields on electronic components in the framework of the Radiation to Electronics (R2E) project.

First, the radiation field requirements on the CHARM facility by the R2E project are discussed. Then, the radiological assessment of the facility is presented, including the shielding design for the prompt radiation and the optimisation of the residual radiation. Furthermore, the air activation calculations, the resulting radiological impact from the release of radionuclides to the environment and the derived requirements for the dynamic confinement of the air inside the CHARM facility are illustrated.

The shielding of the CHARM facility will also include the CERN Shielding Benchmark Facility (CSBF) situated laterally above the target. This facility will allow deep-penetration benchmark studies of various shielding materials. The current plans for the construction and the commissioning of the CSBF are outlined.

Session I: Source Term and Related Topics

Chair: Hee-Seock Lee

S. Ban (KEK), M. Brugger (CERN), R. Grove (ORNL), J. Gulliford (NEA), H. Hirayama (KEK), G. Hughes (LANL), B. Kirk (honorary), H.S. Lee (PAL), S. Mashnik (LANL), N. Mokhov (the general chairman of SATIF-12, FNAL), G. Muhrer (ESS), T. Nakamura (honorary), H. Nakashima (JAEA), S. Roesler (CERN), S. Rokni (SLAC), E. Sartori (honorary), M. Silari (CERN), T. Valentine (ORNL), P. Vaz (IST), and A. Yamaji (NEA).

The members of the Local Organising Committee (from FNAL) were:

M. Bruce, D. Cossairt, N. Mokhov, V. Pronskikh, I. Rakhno, C. Sazama, K. Vaziri, and S. Weber.

simulation codes, which were not presented this time (e.g. PHITS, MCNP) and of discussions on safety factors applied in design and licensing of facilities.

The sixth session was chaired by R. Grove (ORNL) and focused on code benchmarking and inter-comparison exercises. The session contained four presentations. Extensive benchmarking and inter-comparisons were presented for the codes FLUKA, GEANT4, MARS15 and PHITS and phenomena. The results on the inter-comparison proposed at the last workshop (SATIF-11) revealed some unexpected discrepancies among results from different codes (in the energy range of 10-100GeV and with increasing angle) and indicated that further comparisons and analyses were needed for the next workshop (possibly, comparison with experimental measurements).

For the first time in the history of SATIF, a poster session was held, due to the high number of submitted contributions that could not be accommodated in the oral session. The session attracted 11 contributions from ESS (2), HZDR (2), Fermilab (4), FRIB (1), JLab (1), and KEK (1) in the topics of radiation protection (7), design of instrumentation (3), and code development (1).

The last session was dedicated to summarising the workshop, identifying areas of co-operation for the next two years, identifying actions required in order to achieve desired progress in the different research areas and monitoring the progress achieved in actions decided in past workshops. Several comments and suggestions were made by the participants and by N. Mokhov and P. Vaz in particular. Some participants showed interest and were encouraged to participate in NEA EGRTS activities and in particular, to participate in the compilation of new experimental data and review of SINBAD.

There were on-going investigations on possible causes of the systematic underestimation or overestimation of code-computed results compared with experimental results (by factors ranging up to a factor of 10 in some cases). The participants agreed on the need to perform further analyses to better understand the reasons for the underestimations and inform the community on their findings. This need was also supported by the outcome results of the computational benchmark proposed by H. Hirayama at SATIF-11. The results from the benchmark indicated a further need to compare total cross-sections used by each code as well as compare total neutron fluence, and total energy fluence emitted from the target. Furthermore, comparison with experimental measurements seemed essential.

Discussions were undertaken on the available computational methods to perform radiation damage assessment and to compute displacement per atom (dpa), helium production, etc. The need to validate models currently used for dpa calculation, using measurements already identified at the SATIF-11 meeting, was re-stated. Suggestions for topics to be addressed in the future SATIF workshops included discussions on state-of-the-art of radiation transport in molecular dynamics and multi-scale modelling.

It was suggested that the next SATIF workshop (SATIF-13) be held in 2016 in Europe following the tradition of rotating the venue between America, Europe and Asia. Anna Ferrari (HZDR) presented that Helmholtz-Zentrum Dresden-Rossendorf is ready to organise SATIF-13 with the support of the Technische Universität Dresden in Dresden, Germany. A technical tour to ELBE (Electron Linac for beams with high Brilliance and low Emittance) may be arranged. A. Ferrari agreed to explore details of the potential arrangements. An interest in hosting SATIF-13 was also expressed by P. Ortego (SEA) at the fourth EGRTS meeting of WPRS held in February 2014 at the NEA. Final confirmation will be provided well in advance of the next meeting. Participants thanked the General Chairman N. Mokhov and FNAL for hosting SATIF-12, for the outstanding scientific programme, for the friendly atmosphere that contributed to foster intense scientific discussion and for their kind hospitality. The Chairman adjourned the meeting.

The members of the Scientific Committee of SATIF-12 were: